IJOER
RESEARCH JOURNAL

ISSN
2395-6992

International Journal of Engineering Research & Science

www.ijoer.com
www.adpublications.org

Volume-3! Issue-10 ! October, 2017 www.ijoer.com ! info@ijoer.com

Preface

We would like to present, with great pleasure, the inaugural volume-3, Issue-10, October 2017, of a scholarly journal, *International Journal of Engineering Research & Science*. This journal is part of the AD Publications series *in the field of Engineering, Mathematics, Physics, Chemistry and science Research Development*, and is devoted to the gamut of Engineering and Science issues, from theoretical aspects to application-dependent studies and the validation of emerging technologies.

This journal was envisioned and founded to represent the growing needs of Engineering and Science as an emerging and increasingly vital field, now widely recognized as an integral part of scientific and technical investigations. Its mission is to become a voice of the Engineering and Science community, addressing researchers and practitioners in below areas

Chemical Engineering	
Biomolecular Engineering	Materials Engineering
Molecular Engineering	Process Engineering
Corrosion Engineering	
Civil Engineering	
Environmental Engineering	Geotechnical Engineering
Structural Engineering	Mining Engineering
Transport Engineering	Water resources Engineering
Electrical Engineering	
Power System Engineering	Optical Engineering
Mechanical Engineering	
Acoustical Engineering	Manufacturing Engineering
Optomechanical Engineering	Thermal Engineering
Power plant Engineering	Energy Engineering
Sports Engineering	Vehicle Engineering
Software Engineering	
Computer-aided Engineering	Cryptographic Engineering
Teletraffic Engineering	Web Engineering
System Engineering	
Mathematics	
Arithmetic	Algebra
Number theory	Field theory and polynomials
Analysis	Combinatorics
Geometry and topology	Topology
Probability and Statistics	Computational Science
Physical Science	Operational Research
Physics	
Nuclear and particle physics	Atomic, molecular, and optical physics
Condensed matter physics	Astrophysics
Applied Physics	Modern physics
Philosophy	Core theories

Chemistry	
Analytical chemistry	Biochemistry
Inorganic chemistry	Materials chemistry
Neurochemistry	Nuclear chemistry
Organic chemistry	Physical chemistry
Other Engineering Areas	
Aerospace Engineering	Agricultural Engineering
Applied Engineering	Biomedical Engineering
Biological Engineering	Building services Engineering
Energy Engineering	Railway Engineering
Industrial Engineering	Mechatronics Engineering
Management Engineering	Military Engineering
Petroleum Engineering	Nuclear Engineering
Textile Engineering	Nano Engineering
Algorithm and Computational Complexity	Artificial Intelligence
Electronics & Communication Engineering	Image Processing
Information Retrieval	Low Power VLSI Design
Neural Networks	Plastic Engineering

Each article in this issue provides an example of a concrete industrial application or a case study of the presented methodology to amplify the impact of the contribution. We are very thankful to everybody within that community who supported the idea of creating a new Research with IJOER. We are certain that this issue will be followed by many others, reporting new developments in the Engineering and Science field. This issue would not have been possible without the great support of the Reviewer, Editorial Board members and also with our Advisory Board Members, and we would like to express our sincere thanks to all of them. We would also like to express our gratitude to the editorial staff of AD Publications, who supported us at every stage of the project. It is our hope that this fine collection of articles will be a valuable resource for *IJOER* readers and will stimulate further research into the vibrant area of Engineering and Science Research.

Mukesh Arora

(Chief Editor)

Board Members

Dr. S.R.Boselin Prabhu

Ph.D, Wireless Sensor Networks, M.E. Network Engineering, Excellent Professional Achievement Award Winner from Society of Professional Engineers Biography Included in Marquis Who's Who in the World (Academic Year 2015 and 2016). Currently Serving as Assistant Professor in the department of ECE in SVS College of Engineering, Coimbatore.

Dr. Maheshwar Shrestha

Postdoctoral Research Fellow in DEPT. OF ELE ENGG & COMP SCI, SDSU, Brookings, SD Ph.D, M.Sc. in Electrical Engineering from SOUTH DAKOTA STATE UNIVERSITY, Brookings, SD.

Zairi Ismael Rizman

Senior Lecturer, Faculty of Electrical Engineering, Universiti Teknologi MARA (UiTM) (Terengganu) Malaysia Master (Science) in Microelectronics (2005), Universiti Kebangsaan Malaysia (UKM), Malaysia. Bachelor (Hons.) and Diploma in Electrical Engineering (Communication) (2002), UiTM Shah Alam, Malaysia

Dr. D. Amaranatha Reddy

Ph.D.(Postdocteral Fellow,Pusan National University, South Korea), M.Sc., B.Sc. : Physics.

Dr. Dibya Prakash Rai

Post Doctoral Fellow (PDF), M.Sc.,B.Sc., Working as Assistant Professor in Department of Physics in Pachhuncga University College, Mizoram, India.

Dr. Pankaj Kumar Pal

Ph.D R/S, ECE Deptt., IIT-Roorkee.

Dr. P. Thangam

BE(Computer Hardware & Software), ME(CSE), PhD in Information & Communication Engineering, currently serving as Associate Professor in the Department of Computer Science and Engineering of Coimbatore Institute of Engineering and Technology.

Dr. Pradeep K. Sharma

PhD., M.Phil, M.Sc, B.Sc, in Physics, MBA in System Management, Presently working as Provost and Associate Professor & Head of Department for Physics in University of Engineering & Management, Jaipur.

Dr. R. Devi Priya

Ph.D (CSE),Anna University Chennai in 2013, M.E, B.E (CSE) from Kongu Engineering College, currently working in the Department of Computer Science and Engineering in Kongu Engineering College, Tamil Nadu, India.

Dr. Sandeep

Post-doctoral fellow, Principal Investigator, Young Scientist Scheme Project (DST-SERB), Department of Physics, Mizoram University, Aizawl Mizoram, India- 796001.

Mr. Abilash

MTech in VLSI, BTech in Electronics & Telecommunication engineering through A.M.I.E.T.E from Central Electronics Engineering Research Institute (C.E.E.R.I) Pilani, Industrial Electronics from ATI-EPI Hyderabad, IEEE course in Mechatronics, CSHAM from Birla Institute Of Professional Studies.

Mr. Varun Shukla

M.Tech in ECE from RGPV (Awarded with silver Medal By President of India), Assistant Professor, Dept. of ECE, PSIT, Kanpur.

Mr. Shrikant Harle

Presently working as a Assistant Professor in Civil Engineering field of Prof. Ram Meghe College of Engineering and Management, Amravati. He was Senior Design Engineer (Larsen & Toubro Limited, India).

Table of Contents

TOC'S Five-Step Cycle: An Approach to Instant Results and Cultural Change

Paula Vargas[1], Liane Mahlmann Kipper[2], André Luiz Emmel Silva[3], Flávia Luana da Silva[4], Gabriela Zucchetti Kessler[5]

[1]Graduation in Industrial Engineering – Universityof Santa Cruz do Sul, Rio Grande do Sul, Brazil
[2]Corresponding Author, PhD in Industrial Engineering, Professor at the Post-graduation Program in Industrial Systems and Process, University of Santa Cruz do Sul, Rio Grande do Sul, Brazil.Av. Independência , 2293 – Bairro Universitário, Brazil, 96800-000, Santa Cruz do Sul, RS; Tel.: +550-51 3717-7390
[3]Master in Environmental Technology, Professor at the Department of Architecture, Engineering and Agricultural Sciences – University of Santa Cruz do Sul, Rio Grande do Sul, Brazil
[4,5]Graduation Student in Industrial Engineering– University of Santa Cruz do Sul, Rio Grande do Sul, Brazil

Abstract— *The Theory of Constraints (TOC) offers an interesting alternative to the use of management tools, in especial yours TOC cycle. Although it is an interesting alternative, only a small number of publications focus on the TOC cycle. This article aims to describe the TOC cycle and to present its application in the furniture industry, aiming to show a simplified method of your application. The approach is exploratory and descriptive, with a bibliometric analysis and case study. After finding a restricted number of publications, some of the articles were analyzed and it was possible to propose and demonstrate a simplified method for the application of the TOC. From the application of the five steps of TOC cycle, it was possible to identify and eliminate the bottlenecks. The results obtained were positive, because in less than a year the productive process presented productivity gains and a change in the organizational culture.*

Keywords— Theory of Constraints, Five Steps, Gain, Productivity.

I. INTRODUCTION

Every company is a complex system that needs to apply management tools to provide productivity gains, and thereafter to provide increases in profit, in order to be in balance with production process bottlenecks. Identifying and dealing with the bottlenecks and at the same time promoting a new organizational culture is not a simple equation to be solved. When talking about the management tools used nowadays by organizations, the Theory of Constraints (TOC) offers interesting alternatives to equations, seeing the company not as isolated parts but as an integrated system or a group of elements where any type of connection can be found [1]. It is an integrated management philosophy that changes managers' ways of thinking and represents an important tool to solve problems. Şimşita, Günayb and Vayvay [2] the TOC prescribes methods and tools to control and overcome restrictions (known as strangulation points in bottlenecks) which limit a system's ability to achieve goals [3].

After analysing these tools, the "five steps" methodology was found, which can implement TOC in a process by structured and simplified means. After that, a bibliometric study was realized on the Scopus database, aiming to analyse the occurrence of researches based on TOC's five-step methodology. Searching for the key terms 'theory of constraints' and 'five steps' in the last ten years, 11 scientific works were found, with eight articles being published in periodicals (Figure 1).

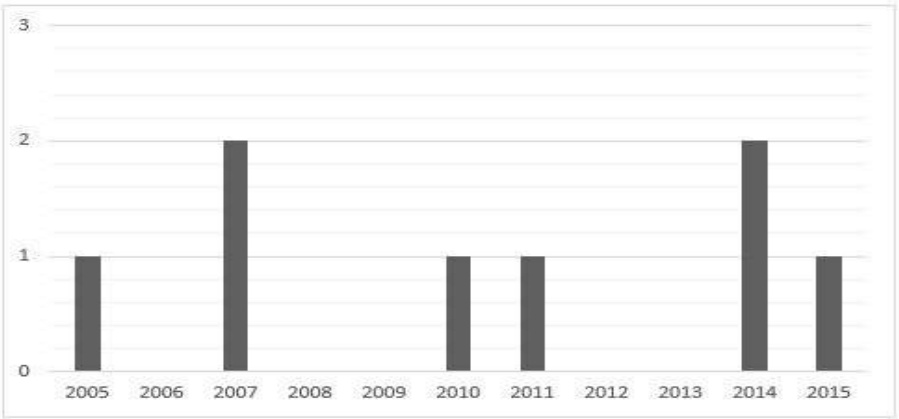

FIGURE 1 – GRAPHIC OF PUBLICATIONS FROM 2005 TO 2015[4]

Considering the small number of publications focused on TOC's five steps – a maximum of two articles per year, with the trend remaining this low – this theme was considered a good one to explore in a theoretical and practical way. According to Silberman et al. [5] despite the advantages provided by TOC, many Brazilian companies still do not use this methodology as a global philosophy of business management. It is believed that this may occur because managers are not compromised to apply the tool or are totally unfamiliar with the theme. In this way, the goal of this article is to describe the five-step methodology and to realize its practical application in a medium-sized company in the furniture industry, aiming to demonstrate a simplified method of applying TOC to identify and eliminate bottlenecks, focused on enhancing productivity.

II. MATERIALS AND METHODS

The research was exploratory and descriptive. Vergara [6] comments that the exploratory research can be realized in areas where only a little accumulated scientific knowledge exists. This work is a research that aims to discover theoretical concepts regarding the five steps of the TOC and the resulting gains and productivity, a subject matter that has not yet been fully explored. Combined with the theoretical research, a bibliometric analysis of the Scopus database was carried out using the keywords 'theory of constraints' and 'five steps'. The research period was from 2005 until August 2015 and the research considered the Scopus database using these keywords. It aimed to learn the distribution of scientific articles published during the period as well as to qualitatively analyse the concepts related to this research. It was also descriptive, because it was realized to try to describe the characteristics that made the TOC five steps a real concept in a familiar company. For this case study, the steps described in the next chapter were followed.

According to Reid [7] the five steps of focalization were carried out to ensure that management would direct its attention to what was really important for the system's good performance, that is, what made the system's constraint performance better. When talking about the cycle, the five steps are represented in Figure 2, showing that after each developed step, another one is unlocked, until the fifth step is reached, when the process can be repeated for the same constraint or starting from a new one, beginning a new cycle, as represented by the doted arrow.

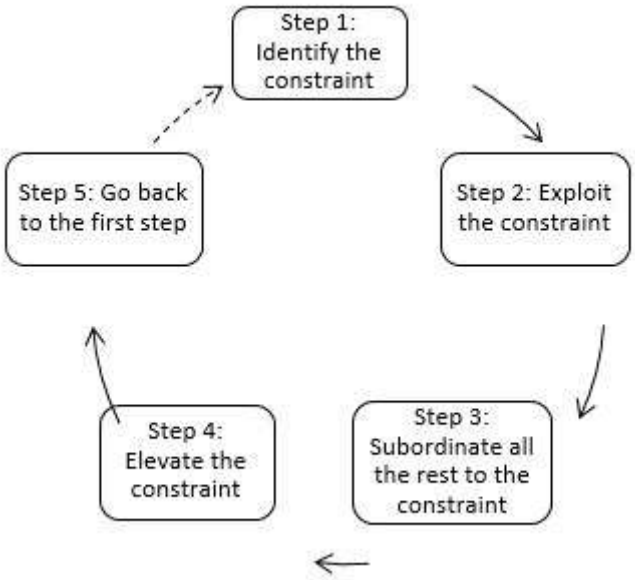

FIGURE 2 – TOC FIVE-STEP CYCLE

The five steps of TOC flow representations are joined by arrows indicating the next step of the cycle. The last arrow can represent the two possible next steps of the process: one is when the bottleneck has not been eliminated in only one round, and the other is when the bottleneck has been eliminated and Step 1 considers a new constraint.

Step 1: Identify the constraint. The identification of the constraint phase of the system must start from process information, focusing on lateness or where most working hours are usually needed, which means that the constraint identification begins from previous knowledge of the process. According to Souza [8], in order to verify whether there is a real bottleneck, the total load must be calculated, generated by the requests that should have been dealt with during the programmed horizon imposed for each type of resource. According to Goldratt [9] in the calculation of machine load, all the requests that should be dealt with inside the horizon must be taken into account. Other complementary variables of the calculation are the existing stock and the set-up times or the machine preparation time. After the calculation, a comparison of the results of the machine

load for each resource must be done, with all the available time determined for the same period. In the case that the machine load presents a higher value than the availability of the resource, this will be treated as a bottleneck.

Step 2: Exploit the constraint. The exploration is likely to reveal the 'hidden capacity' that will allow the transfer rate to increase without additional costs [10]. As Reid [7] mentioned, this step aims to maximize the existing operational set-up efficiency from the constraint resource inside the system. In other words, the management must focus on eliminating all the waste or unproductive time in activities where the constraint occurs, increasing the capacity of the production system.

Step 3: Subordinate all the rest to the constraint. The subordinate step consists in the process of making a non-constraint to produce only what the system constraint allows. According to Pretorius [11], the third step deals only with the management rules for non-constraints, which are often related tothe 'Road Runner ethic' or behaviour. This means that the non-constraint's level of application is determined by constraints on the capacity and usage.

Step 4: Increase the constraint. Pretorius [11] affirms that when improvement of the system through exploration and subordination is not possible, the next step is to increase the constraint capacity. This step aims to find alternative ways to increase the constraint capacity. Once the capacity of the constraint is increased, constraint new constraint may happen in another activity of the production system or the constraint could continue in the same place, but with its capacity increased [11].

Step 5: Go back to the first step. From the TOC's cycle, depending on the decisions made during the process, a new constraint is created. In this way, the fifth and last step aims to go back to the first one if the constraint has been solved or to go to the identification of a new constraint caused by the elimination of the bottleneck. Reid [7] states that when a decision is made to keep the constraint in its current location, management actions taken in later steps will lead to a new location of constraint in the system. Therefore, it is necessary to return to the first step and identify a new system constraint.

III. THEORETICAL FRAMEWORK

3.1 Theory of Constraints (TOC)

According to Naor et al. [12], the origin of TOC dates from 1970, when Goldratt [9] was motivated to assist his neighbour, who worked in a cage factory, by developing an effective programme to increase the industry output. The programme, later called Optimized Production Technology (OPT), was quickly adopted by big US corporations. Despite the huge adoption a few years after its creation, many failures were identified. To improve the OPT,Goldratt [13] created the TOC, which spread worldwide after publication in 1984 of the book *The Goal*. The book sold more than 5 million copies, was translated into 21 languages, and became a mandatory read on many management courses around the world [12]. From the book*The Goal*, which claims that the only purpose of a company is to make a profit now and in the future, the authors define six variables as organizational measures to reach that goal. Three of them are operational: income, inventory, and organizational expenses. The other three are financial: liquid profit, return on investment (ROI), and cash flow. All these metrics are combined through relationships [14]. According to Ifandoudas and Chapman [15], the benefits achievable with the adoption of TOC are reported as a reduction in delivery time, cycle time, reduced inventory, and improved productivity and quality of production.

The tools that compose the TOC thinking process allow diagnosis of the problem, the development of new solutions, and the building of action plans Kim et al. [16] allowing the manager to pay attention to more serious questions [17]. TOC is a theory that clearly identifies a gain orientation, together with three dimensions: mind maps, metrics, and methodology [18]. It can also be defined as a management philosophy that provides a focus on continuous improvement, resulting in advances in organizational performance [19, 20]. This philosophy starts from the principle that each organization has constraints that stop it from achieving its goals; in this way, a company is as strong as its biggest constraint. Therefore, there is always an aspect in every system which determines its result. A constraint can be a physical resource, management politics, or behaviour factors [21].

There are good cases of TOC application in many different sectors, such as production, logistics, supply chain, distribution, project management, accounting, research and development, sales and marketing, and others [22, 2]. Its first application was in production planning and programming to maximize profits and effectiveness related to market demand by identifying and exploring the constraint resources [23], using the Drum–Puffer–Rope (DPR)methodology [24, 25] and defining five steps for the TOC process.

The DPR methodology is a basic TOC principle, where all the bottleneck's resources impose the production rhythm, because they are the chain's weakest link [5]. The method focuses on seeking a production flow balance, directed by the restrictions

and resource capacity. According to Naor et al. [12], the 'drum' represents the production rate. It gives the synchronization rhythm to the system's activities flow. The 'rope' is a communication mechanism that transfers information to the system based on 'puffer' consumption, which is the information flow or materials. In this way, the whole mechanism must work in harmony.

3.2 Five steps

The TOC principle emphasizes the importance of identifying and eliminating bottlenecks (constraints) in the manufacturing process, not only to increase productivity, but also as a tool to measure and control the materials flow [26]. The five steps comprise a methodology that aims to break up the system constraints and to achieve a high level of performance management [27]. According to the TOC, every system oriented towardsa defined goal needs to have at least one limitation on achieving this goal; otherwise the system's profitability would be endless. In this direction, TOC proposes that every organization should follow the five steps [13, 28, and 9] as a way to identify constraint factors that stop the company achieving its goals, with the aim of breaking them, and repeating these steps as part of a continuous process improvement [29].

1. Identify the system constraints;
2. To exploit the system constraints to their maximum;
3. To subordinate everything else to the system constraints;
4. To raise the system constraints;
5. To go back to the first step.

In the next part, the results found from the exploration and descriptions of the realized research are presented.

IV. RESULTS AND DISCUSSION

From the exploration of research using bibliometric analysis, the results listed in Table I were obtained.

TABLE 1
LIST OF ARTICLES, AUTHORS, AND PUBLICATION DATE (2005 – AUGUST 2015).

Article title	Authors	Publication Year
Theory of constraints – application in land transportation systems [3]	AleksandarZivaljevic	2015
Introducing in-between decision points to TOC's five focusing steps [11]	Pieter Pretorius	2014
Applying the Theory of Constraints in the South African coal supply chain [30]	Ken Mathu	2014
Theory of constraints – lessons for academicians and practicing managers from "the goal – II" [31]	Ajay Kumar Gupta; Arvind Bhardwaj; Arun Kanda	2011
The TOC-based algorithm for solving multiple constraint resources [32]	KumarAmitava Ray; Bijan R. Sarkar; Subir KumarSanyal	2010
Applying the TOC five-step focusing process in the service sector: A banking subsystem [7]	Richard A. Reid	2007
Applying Theory of Constraints on ongoing improvement in manufacturing system dealing with animal feed [33]	Sumitra K Mukhopadhyay; Joy Prakash Panda	2007
From Management by Constraints (MBC) to Management by Criticalities (MBC II) [34]	Dan Trietsch	2005

Table 1 presents the articles found from the bibliometric analysis realized using the Scopus database covering the period from 2005 until August 2015. From these titles, an exploratory research was made in the completed texts, where it was possible to access five of them. Table 2 synthesizes the main aspects of these five works, highlighting the major results of the five steps described and using tools.

TABLE 2
SYNTHESIS OF THE MAIN INFORMATION FROM THE FIVE ARTICLES IN THE REALIZED BIBLIOMETRIC ANALYSIS.

Author (year)	Objective	Method	Main Results
AleksandarZivaljevic (2015) [3]	To exploit the usage of TOC in the approach to traffic jams as a main restriction to improve the usage of a land transport system.	Exploratory research to develop a provisional theory through the generation of new ideas and assumptions, making an image database for the advancement of investigations.	The research concludes that the biggest restriction is broken at the third step of TOC's five steps and that improvement in certain segments of land transport could be reached using the theory.
Pieter Pretorius (2014) [11]	To ensure a large application of the five steps to also include non-physical constraints, which cannot be approached when using linear programming.	Conceptual research through a search for concepts to define a diagram that helps the execution of the TOC's five steps when a non-physical constraint occurs.	A focus diagram of the TOC's five steps, detailing the decision point, especially for non-physical constraint cases.
Ken Mathu (2014) [30]	To establish processes to minimize or relieve the constraint found at a coal mining supply chain in South Africa with the aim of improving its operational effectiveness, efficiency, and profitability.	Qualitative research.	The main process restrictions were found and the steps required to minimize the constraints were indicated.
KumarAmitava Ray; Bijan R. Sarkar; Subir KumarSanyal (2010)[32]	To analyse the heuristic model integration, comprising the Analytic Hierarchy Process (AHP) and TOC in a decision model.	The methodology incorporates an analysis to provide the decision maker with additional information about the model strength, so he or she can make the best decision.	Elaboration and revision of an algorithm. Many advantages are indicated: 1) It is suitable to deal with production analysis. This includes quantitative factors. 2) It eliminates strict mathematical expressions. 3) It is simple and direct. 4) It generates the ideal solution in any case.
Richard A. Reid (2007) [7]	To present a detailed descriptive analysis of sequential TOC application with a focus on the process improvement of five steps for service process, that was limited all the service system.	The five-step approach is presented with each step being described and evaluated in relation to its role in effective constraint management. An example of a bank sub-system provides additional insights.	An illustrative tutorial that details the TOC application in the effective management of a service process.

From Table 2, it was possible to identify the satisfactory results that the research focusing on the TOC's five steps showed, making the idea of a practical and effective application strong for this methodology. Also for to realize that theoretical researches are still broadly discussed, aiming to improve the TOC cycle usage in diverse industrial sectors

In relation to the case study realized, it was observed that the main productive process flow involves the following sectors of: cutting, edge banding, drilling, painting, and packaging.

Knowing the process, the TOC application started with the previous analysis of each sector to identify the first constraint. In this way, for each constraint found, the five-step methodology with an execution chronogram of the bottleneck elimination work were followed, always in search of the goal, according to Reid [7] After the fifth step ,return to step 1 and eliminating the next bottleneck by repeating the steps until the current bottleneck was elminated. After the identification of the first bottleneck and execution of TOC, three other bottlenecks were identified in different sectors (Figure 3).

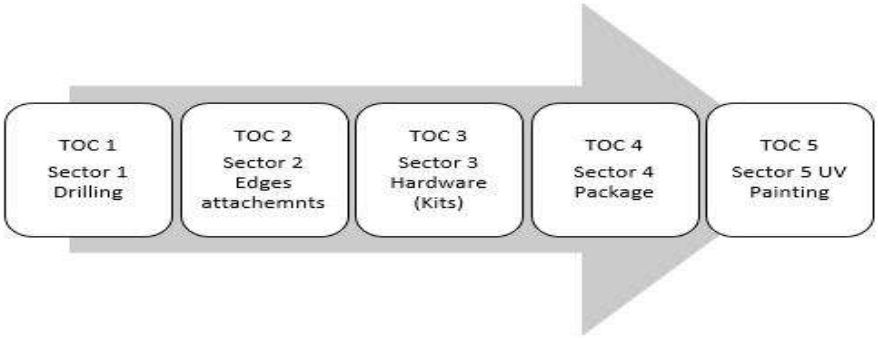

FIGURE 3 – CONSTRAINTS FLOW

In TOC 1, the application of the first tool was realized from the initial identification of the bottleneck. This bottleneck was a problem known by all personnel working in the factory, and in this way, the analysis started from this manufacturing limitation. According to Vergara [6] analysis of the first step is based on information about the process that is already known, usually concerning failures. In Figure 4 shows a flowchart of the five steps of TOC 1, with the first step being at the top of the flow.

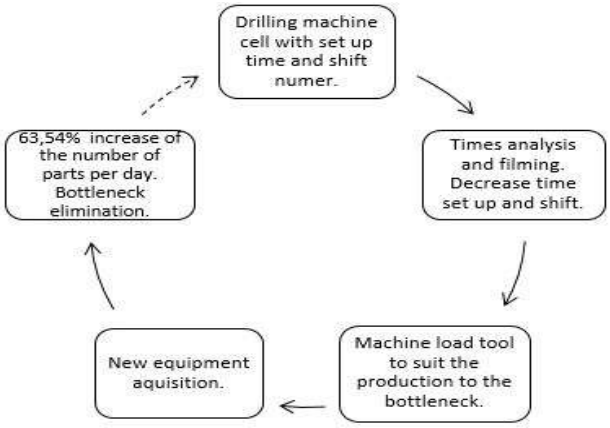

FIGURE 4 – FIVE STEPS OF TOC 1

The elimination of the bottleneck in the tool sector, led to a significant increase in the daily production, which ultimately initiated a new constraint in the cell that predates the drilling machine in the process. As a solution, the production was maximized through the lifting of the restriction, transforming the machine into two equal parts. This premise confirms the finding of Goldratt [9] that when perfection of the system is reached, the alternative is to raise the restrictive factor. Thus, Figure 5 shows the five-step flowchart of TOC 2, with the first step being at the top of the flow.

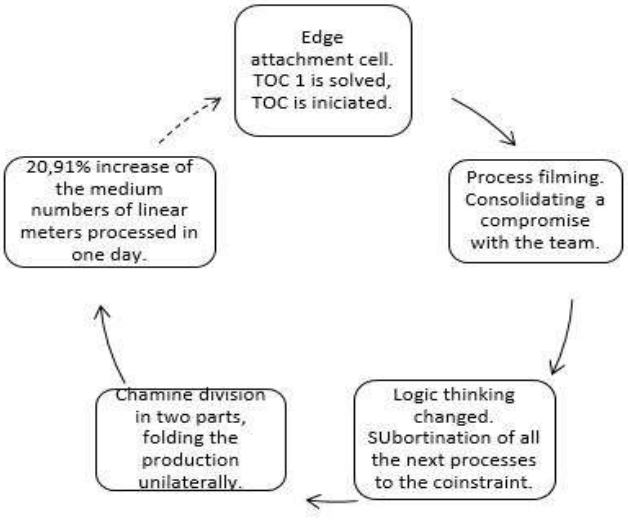

FIGURE 5 – FIVE STEPS OF TOC 2

With the increase of daily production in these two manufacturing sectors, the fittings sector becomes incapable of supplying the production demand with a reduced shift and becomes a new process bottleneck. According to Silberman et al. [5], depending on the decisions regarding the process, a new constraint is generated. From this bottleneck, TOC 3 is initiated and its five steps are represented in the flowchart shown in Figure 6.

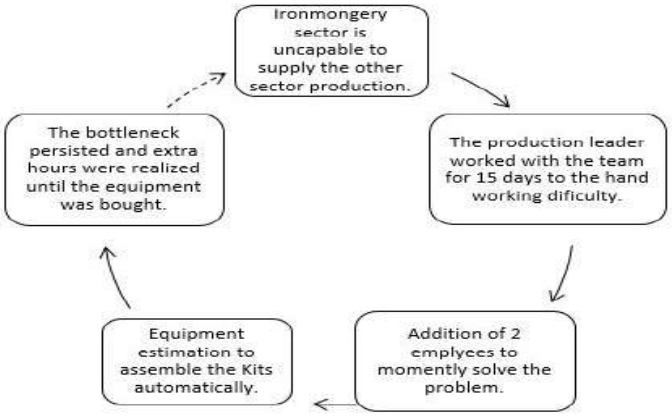

FIGURE 6 – FIVE STEPS OF TOC 3

In the last productive flow step, the fourth constraint was found, initiated by the increase in production in most of the other sectors. This constraint was about the inability to supply the final processing of the product. TOC 4 arises from that event, and its five steps are represented in the flowchart in Figure 7.

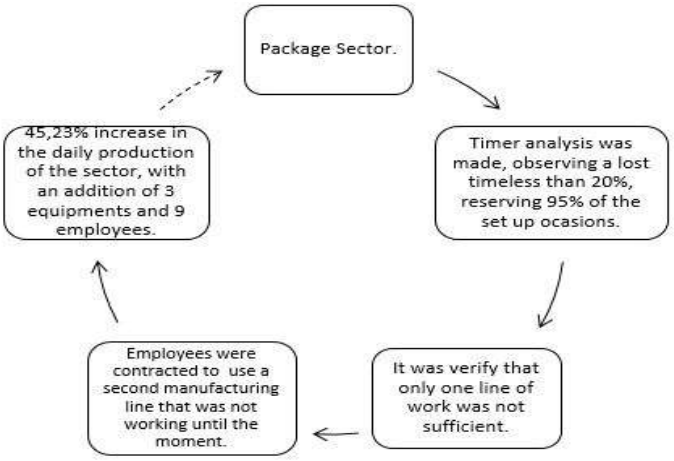

FIGURE 7 – FIVE STEPS OF TOC 4

With the elimination of the bottleneck by TOC 4, the daily appearance of new bottlenecks is inevitable, because the natural cycle of the TOC is to find and eliminate them through the five steps. Tyan et al. [36] suggest that the principles of TOC are effective tools for continuous improvement of a process. From the satisfactory results, the continued use of this tool is already shaping a new culture at the factory, allowing gains in productivity and profit, as can be seen in Figure 8.

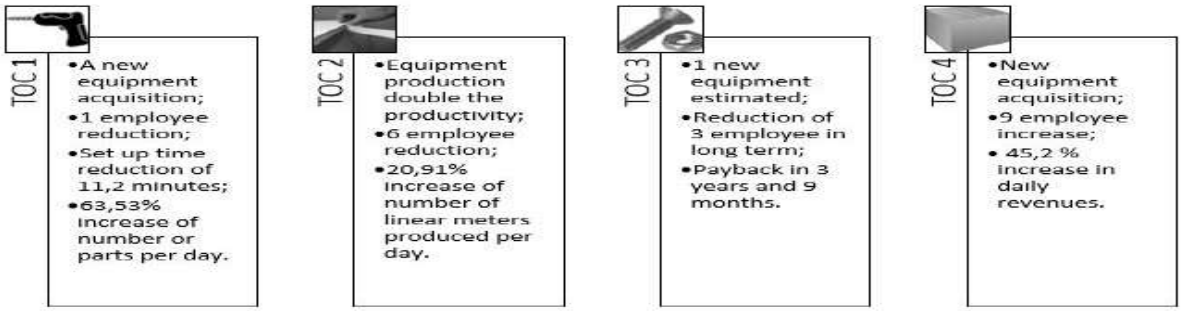

FIGURE 8 – RESULTS FOUND WITH THE USE OF THE TOC CYCLE

Figure 8 represents the gains acquired in each realized TOC cycle in the process. From these numbers it is possible to perceive the improvement achieved in each step either by reducing the number of employees or by increasing productivity, strengthening the affirmation of Naor et al. [12] that the TOC is an example of an operations management approach used successfully in practice.

Sharma [35] considers that of the production operations of a company will always be relevant, as it facilitates a clear understanding and problem analysis. Visualizing the results in terms of operational aspects, income increases and decreases in inventory and operational expenses, which improves the company's financial variables, increasing its liquid profit, ROI, and cash flow. These six variables are the so-called organizational measures described in the book *The Goal*, and they have a direct connection with the organizational goal of making money. These relations between operational and financial aspects shows that the main gain that every company seeks – profit – becomes more achievable after the application of the TOC's five steps to the process, turning the operational gains into financial ones.

Another important aspect is the change in cultural organization or the alteration of the mind maps developed in the employees involved during the execution of each cycle. It was observed that the execution of the TOC cycle promoted better employee performance and a greater contribution of the employees to the improvement of the process as a whole. The change of this mental model adopted by the employees came from the TOC's measures and methodology, naturally adopted during its application, proving the results of Gupta and Boyd [18], shows the TOC's relationship with mental models, measures, and methodologies. With the use of the TOC cycle, there are changes in the way each employee behaves and sees his or her work, leading to changes in his or her way of acting in relation to work and the organization.

This change in mental models caused by the measures and changes in methodology adopted in the TOC cycles can be considered the most important, because this aspect ensures the continuity of the TOC process and in consequence the company's evolution and increase in benefits achieved, as stated by Goldratt [13] who reported operating earnings by using the TOC.

V. CONCLUSION

From the point of view of theoretical studies, the TOC showed to be more effective when the five-step methodology is applied, because of its understandable simplicity and practical application in numerous industrial sectors.

From the theoretical researches realized, it was possible to verify the existence of just a few articles that used the TOC five steps as the main strategy for theapplication of tools. In this way, it was possible to propose and demonstrate a simplified method for the application of the TOC. In this application of this method, the results achieved by the application of the five steps were very positive, because it was observed that in less than one year the production already showed results very close to the expected results, besides ensuring a culture change in the factory that changed the employees' way of thinking and acting regarding their jobs.

The mind maps underwent significant alterations following the measures and changes of the methodologies of the daily work of every employee. The relations between these three dimensions demonstrate the strong connection when things change. After the operational results, work measures, and methodologies, modification of the mind maps through which the organization and its productive methods were visualized could be observed, bringing gains in all aspects.

Finally, through the case study it could be observed that TOC is a trustable and flexible theory that brings gains and objectivity to solving problems such as bottleneck elimination with profit gains, besides significantly changing the industry's daily work, bringing a more effective dynamic to achieve the goal of the company.

REFERENCES

[1] Quelhas, O., A. B. Barcaui. "A teoria das restrições aplicada a gerência de projetos: uma introdução à corrente crítica." [2008]. Accessed: 25 Sept. 2015.<www.pmtech.com.br/newsletter/Marco_2005/TOC_e_CCPM_em_GP.pdf>.

[2] Şimşita, Z. T., N. S. Günayb, O. Vayvay. 2014. "Theory of Constraints: A Literature Review." *Procedia – Social and Behavioral Sciences*. v. 150, p. 930–936, (2014).

[3] Zivaljevic, A. "Theory of constraints – application in land transportation systems." *Management of Environmental Quality: An International Journal*. v. 26, n. 4, p. 505–517, (2015).

[4] SCOPUS. 2015. Accessed: 30 Sept. 2015. http:<//www-scopus-com.ez127.periodicos.capes.gov.br/home.uri?zone=header&origin=searchbasic>.

[5] Silberman, I. M., P. R. Silva, R. M. Ayres, S. Cogan. "Teoria das restrições (TOC): uma análise de estudos de caso disponíveis em anais de congressos." *Revista de Contabilidade do Mestrado em Ciências Contábeis da UERJ* (online), Rio de Janeiro, v. 17, n.2, p. 28–44, (2012).

[6] Vergara, S. C. *Projetos e relatórios de pesquisa em administração***.** 14. ed. São Paulo: Atlas. 94 p., (2013).
[7] Reid, R. A. "Applying the TOC five-step focusing process in the service sector: A banking subsystem." *Managing Service Quality: AnInternationalJournal*. v. 17, n. 2, p. 209–234, (2007).
[8] Souza, F. B. "Do OPT à Teoria das Restrições: avanços e mitos." *Revista Produção*. v. 15, n. 2, p. 184–197, (2005).
[9] Goldratt, E. M. *Haystack Syndrome: Sifting information out of the data ocean*. North River Press (1990).
[10] Schragenheim, E., H. Dettmer. *Manufacturing at Warp Speed*.StLucie Press, Boca Raton, FL (2001).
[11] Pretorius, P. "Introducing in-between decision points to TOC's five focusing steps." *International Journal of Production Research*.v. 52, n. 2, p. 496–506 (2014).
[12] Naor, M., E. S. Bernardes, A. Coman. "Theory of constraints: is it a theory and a good one?" *International Journal of Production Research*. v. 51, n. 2, p. 542–554 (2013).
[13] Goldratt, E. M., and J. Cox. *The goal: A process of ongoing improvement*. Great Barrington. MA: North River Press (1984).
[14] Costas, J., B. Ponte, D. De la fuente,, R. Pino,, J. Puche. "Applying Goldratt's Theory of Constraints to reduce the Bullwhip Effect through agent-based modeling.Original Research Article."*Expert Systems with Applications*, v. 42, n. 4, p. 2049–2060, (2015).
[15] Ifandoudas, P., and R. Chapman. "A practical approach to achieving agility–a theory of constraints perspective." *Production planning and control*, *20*(8), 691-702 (2009).
[16] Kim, S., V. J. Mabin, J. Davies. "The theory of constraints thinking processes: retrospect and prospect." *International Journal of Operations & Production Management*. v. 28, n. 2, pp.155–184 (2008).
[17] Wu, H. H., A. H. I. Lee, T. P. Tsai. "A two-level replenishment frequency model for TOC supply chain replenishment systems under capacity constraint." *Computers & Industrial Engineering*. v. 72, p. 152–159 (2014).
[18] Gupta, M. C., L. H. Boyd. "Theory of constraints: a theory for operations management." *International Journal of Operations & Production Management*. v. 28 n. 10, pp. 991–1012 (2008).
[19] Inman, R. A., L. M. Sale, K. W. Green JR. "Analysis of the relationships among TOC use, TOC outcomes, and organizational performance." *International Journal of Operations & Production Management*. v. 29, n. 4, pp. 341–356 (2009).
[20] Zheng, B., Y. C. Gao, Y. Wang. "The Product-Mix Optimization with Outside Processing Based on Theory of Constraints Oriented Cloud Manufacturing." *Applied Mechanics and Materials*.v. 121–126, p. 1306–1310 (2011).
[21] Blackstone, J. H. "Theory of constraints – a status report." ***International Journal of Production Research,*** v. 39, n. 6, p.1053–1080 (2001).
[22] Wu, H. H., C. P. Chen, C. H. Tsai, T. P. Tsai. "A study of an enhanced simulation model for TOC supply chain replenishment system under capacity constraint." *Expert Systems with Applications*. v. 37, n. 9, p. 6435–6440 (2010).
[23] Golmohammadi, D. "A study of scheduling under the theory of constraints." *International Journal of Production Economics***.**v. 165, p. 38–50 (2015).
[24] Simons, J. V., P. W. Wendell. "An exposition of multiple constraint scheduling as implemented in the goal system." *Production and Operations Management*.6 (1), 3–22 (1997).
[25] Ronen, B., S. Pass. *Focused operations management: Achieving more with existing resources*. Hoboken, New Jersey: John Wiley & Sons (2008).
[26] Izmailov, A. "If Your Company is Considering the Theory of Constraints." *Procedia – Social and Behavioral Sciences*. v. 150, p. 925–929 (2014).
[27] Tsou, C. "On the strategy of supply chain collaboration based on dynamic inventory target level management: A theory of constraint perspective." *Applied Mathematical Modelling*. v. 37, n. 7, p. 5204–5214 (2013).
[28] Goldratt, E. M., and E. R. Fox. 1989. *A corrida*. São Paulo: IMAM (1989).
[29] Kahmann, A., A. P. Kloeckner, L. Zocche, R. A. Cassel. "Theory of Restrictions and Project Management – Critical Chain: A Systematic Review of the Literature." *Espacios***.** v. 35, n. 13 (2014).
[30] Mathu, K. "Applying the Theory of Constraints in the South African Coal Supply Chain." *Mediterranean Journal of Social Sciences*.MCSER Publishing, Rome, Italy.Vol. 5, No. 9, (2014).
[31] Gupta, A., A. Bhardwaj, A. Kanda. "Theory of Constraints – Lessons for Academicians and Practicing Managers from "The Goal - II"." *World Academy of Science, Engineering & Technology*. v. 54, p. 134, (2011).
[32] Ray, A., B. Sarkar, S. Sanyal. "The TOC-Based Algorithm for Solving Multiple Constraint Resources. IEEE Transactions on Engineering Management, Vol. 57, No. 2, Mai (2010).
[33] Mukhopadhyay, S. K., J. P. Panda. "Applying theory of constraints on ongoing improvement in manufacturing system dealing with animal feed." *International Journal of Manufacturing Technology and Management*. v. 10, n. 2/3, p. 261–275, (2006).
[34] Trietsch, D. "From management by constraints (MBC) to management by criticalities (MBC II)." *Human Systems Management*. v. 24, n. 1, p. 105–115, (2005).
[35] Sharma, S. "Development of supplier relationship including cost of defectives in the cyclic production." *Production Planning & Control*. v. 24, n. 8/9, p. 759–768, (2013).
[36] Tyan, J. C., Chen, J. C., & Wang, F. K. Development of a state-dependent dispatch rule using theory of constraints in near-real-world wafer fabrication. *Production Planning & Control*, 13(3), 253-261, (2002).

Path Planning with Smooth Curve Using Electromagnetism-like Mechanism Algorithm

Ming-Wei Hsu[1], Shih-Hua Huang[2], Yih-Guang Leu[3*]

Department of Electrical Engineering, National Taiwan Normal University, Taipei, Taiwan
Email: leuyk@ntnu.edu.tw (*corresponding author)

Abstract— *In this paper, we propose a new path planning method by using an electromagnetism-like mechanism algorithm. We use the different encoding method to solve trade-off problem that is encountered in the traditional path planning method. By combining different encoding method with electromagnetism-like mechanism algorithm, path point can be generated without the trade-off problem. In order to connect these points into smooth curve, we compare two path smoothing method, Bezier curve and cubic splines interpolation. Finally, cubic splines interpolation is used because it can generate smoother path.*

Keywords— Path Planning, Electromagnetism-like Mechanism Algorithm, Path Smoothing.

I. INTRODUCTION

For all of the mainstream robots which have the movement capability, path planning will be a necessary and worthwhile problem to solve. The traditional path planning method is proposed by computer scientist Dijkstra [1], then A* algorithm [2] solves the problem of direction. The A* algorithm makes it work more efficiently, but these algorithms will encounter the map trade-off problem in the practical application. In a known environment, the map needs to be cut into many grids, and these grids are used to plan the path.

The process of grids is a trade-off problem. If the map is cut into large grids, the relative generated path will be very rough. However, if the map is cut into small girds, it will cost a lot of computing costs. In real case, the obstacles on the map is irregular shape, such that path planning result is not the shortest path. As a result, many algorithms were proposed to compute shorter or more effective path for the trade-off problem.

To solve the problem mentioned above, we need to change the processing method for path planning by using a different map encoding method [3] and connect with the heuristic algorithm to solve the path planning problem. The electromagnetism-like (EM) algorithm [4] is innovative in the heuristic algorithm which is based on the characteristics of electromagnetic attraction and repulsion.

In this paper, instead of applying EM algorithm for optimization, we combine EM algorithm with different encoding method for path planning. It can avoid traditional trade-off problem by spreading points and connecting these points. The algorithm computes the path with path smoothing method. In this paper, cubic spline interpolation is chosen because it can smooth the path without increasing the algorithm's parameters. To demonstrate the proposed method, we simulate the possible map configuration, and use map simulation to verify the feasibility of the algorithm.

II. ELECTROMAGNETISM-LIKE MECHANISM ALGORITHM

Electromagnetism-like Mechanism algorithm [4] is a heuristic algorithm proposed in 2003, and the convergence is presented in [5]. EM algorithm applies the concept of Coulomb's law in the electromagnetic, the better electronic attract bad electrons, and bad electronics will repel other good electronics. The attraction and repulsion forces between electrons accumulate into total force in order to make the path result to better direction. Because EM algorithm has good computing ability, there are many kinds of applications, such as optimization question for communication system [6] [7], optimization the neural networks [8], optimization the learning rule for fuzzy neural networks [9], path-tracking problem [10], optimized tool path planning [11], parameter optimization [12], the routing problem [13], optimization the knapsack problem [14] and other applications [15] [16].

Besides considering the better solution, EM algorithm also consider the worst solution as a contrarian indicator, these multiple reference can let the solution converge faster. On the other hand, the EM algorithm has fewer parameters; it is more intuitive and convenient in parameter adjustment. And it can add more electronics in the map, such that user can adjust parameter based on road condition. It is feasible to choose the EM algorithm for path planning.

The EM algorithm includes four parts [17]: initialize the algorithm (Initiation), search the neighborhood to avoid falling into the optimal solution (Local), calculate the total force (CalcF) for each electronics, and move the electronics along the force direction (Move).

General framework is shown below.

```
1: Initiation()
2: ite←1
3: while ite <MAXITE do
4:   Local(LITE,α)
5:   F ←CalcF()
6:   Move(F)
7:   ite ←ite + 1
8: end while
```

In this paper we use the modified EM algorithm which adds the rearrange function in original EM algorithm. Rearrange function can adjust the position of electrons without altering the path, and it makes the EM algorithm can generate global optimal solution quickly. The flow chart of the EM in this paper is shown in Fig. 1.

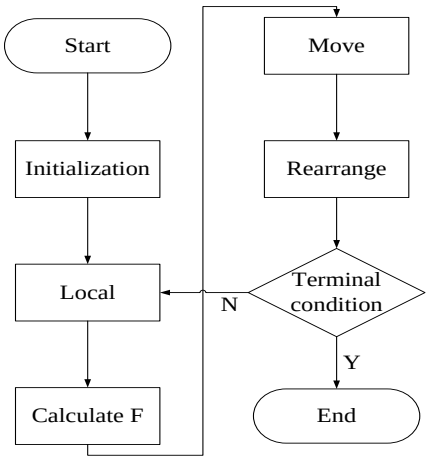

FIG. 1. FLOW CHART IN THIS PAPER

Step1: *Initiation*

Initiation spreads point randomly in the map. Each one of the point is regard as one electrical point, and all of the electronics are connected from start point to the end point, as shown in Fig. 2(a). Then the point is spread, and each electronic evaluates the other electronics' magnetic which has same dimensions, as shown in Fig. 2(b).

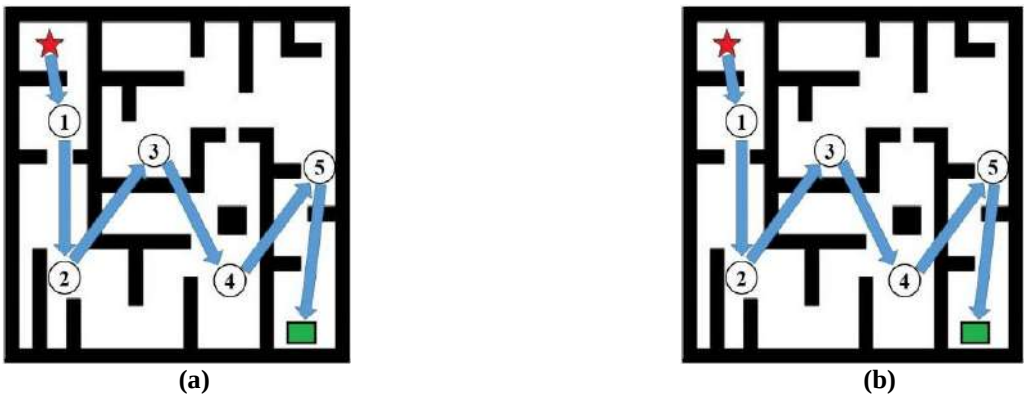

(a) **(b)**

FIG. 2. (a) LINK THE ELECTRICAL POINT. (b) TWO ELECTRICAL IN THE SAME FIELD

Step2: *Local*

Local makes a provisional electronics for each dimension. The electronic is a replica of the original one, then move randomly. If *Local* finds the better result, it will replace the original one, and finally find out whether there is a better global optimal solution.

Step3: *CalcF*

It is necessary to calculate charge amount for each electrons Q_i before calculating the total force. The attraction and repulsion forces are determined by charge amount. The charge amount of the i th electron is shown in (1).

$$Q^i = \exp(-n\frac{f(e^i)-f(e^{best})}{\sum_{i=1}^{m}(f(e^k)-f(e^{best}))}) \tag{1}$$

where m means the number of particles, e^i means the current electronic, and e^{best} means global optimal solution. The global optimal solution has a greater attraction. Then, calculate the total force F^i for each electron, as shown in (2).

$$F^i = \sum_{j\neq i}^{m}\begin{cases}(e^j-e^i)\dfrac{Q^iQ^j}{\left\|e^j-e^i\right\|^2}\\ (e^i-e^j)\dfrac{Q^iQ^j}{\left\|e^j-e^i\right\|^2}\end{cases} \tag{2}$$

Although equation (2) is more accord with physical meaning, it costs more time in algorithm. By [18], we use equation (3) to accelerate the implementation rate of algorithms.

$$F^i = \sum_{j\neq i}^{m}\begin{cases}(e^j-e^i)Q^iQ^j & if \quad f(e^j)<f(e^i)\\ (e^i-e^j)Q^iQ^j & if \quad f(e^j)\geq f(e^i)\end{cases} \tag{3}$$

Step4: *Move*

After calculating the total force F^i, electrons are designed to move a random distance based on the direction of the total force, and the movement method is shown on equation (4).

$$e_k^i = e_k^i + \gamma\frac{F^i}{\left\|F^i\right\|}(RNG) \tag{4}$$

where γ means a uniform distribution between 0 and 1. It also can use other types of distributions in calculating the step length. RNG means a random number for step length. It can determine a nonzero probability to move to unvisited search space.

Step5: *Rearrange*

If the electronics are overly concentrated, the EM algorithm will occur sharp point phenomenon when it applied to path planning, as shown in Fig.3. Therefore, we need the *Rearrange* function to redistribute the electrons. As a result, the global optimal solution is generated more quickly.

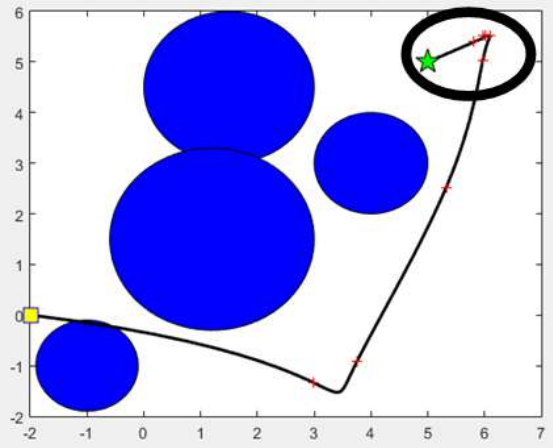

FIG. 3. SHARP POINT PHENOMENON

The general framework of the *Rearrange* function is described as follows.

```
1: γ ← RNG(0,1)
2: if γ < T*det then
3:   j ← 1
4:   for i = 1 to h do
5:     if length(i) = L*j/n
6:       e_k^i = position(i)
7:       if i = n+1
8:         break
9:       end if
10:      j ← j+1
11:    end if
12: end for
```

γ means a uniform distribution between 0 and 1. T means the threshold which makes the path rearrange. *det* is a parameter decrease when iteration number increases. We use *det* to control the probability which let algorithm execute the *Rearrange* function. L is the length of the path, n is the number of sections.

III. PATH SMOOTHING

The result of the path planning often has a non-smooth turning characteristic. It is caused by the rough segmentation of the map. This makes the path planning result possess sharp angle turning in the actual application. Therefore, the vehicle must need a lot of deceleration, or even stop the vehicle to make a turn.

After the path smoothing process, it makes the smooth path planning result. Therefore, the vehicle can make a turn without a lot of deceleration in actual application.

However, when we use high-order polynomial to approximate the path planning result, Runge's phenomenon will occurs. Runge's phenomenon occurs when using polynomial interpolation with polynomials of high degree over a set of equispaced interpolation points. It is a problem of oscillation at the edges of an interval. To avoid Runge's phenomenon, multi-sections are used rather than high-order interpolation method for path smoothing. This paper will introduce two methods of smoothing path in follow.

3.1 Bezier Curve [19]

Given point D_0 and D_1, the Bezier Curve L_0 is a straight line between those two points. The curve is given by equation (5):

$$\mathrm{L}_0 = (1-t)D_0 + tD_1 \tag{5}$$

If Bezier Curve starts from D_0 to D_2 and has a relay point D_1, the second order Bezier Curve $C_2(t)$ is shown as equation (6):

$$C_2(t) = (1-t)^2 D_0 + 2t(1-t)D_1 + t^2 D_2 \tag{6}$$

The general form of a n degree Bezier curve defined by the control points D_i (where $i = 0, \cdots, n$) is

$$C(t) = \sum_{i=0}^{n} B_{i,n}(t) D_i \tag{7}$$

where $B_{i,n}(t)$ is called Bernstein polynomials that are defined in (8).

$$B_{i,n}(t) = \binom{n}{i} t^i (1-t)^{n-i} \tag{8}$$

the cubic Bezier curve $C_3(t)$ is given in (9).

$$C_3(t) = (1-t)^3 D_0 + 3t(1-t)^2 D_1 + 3t^2(1-t)D_2 + t^3 D_3 \tag{9}$$

3.2 Cubic Splines Interpolation [20]

Spline interpolation uses segmented polynomial to interpolation, and it can achieve the smaller interpolation error by using low-order polynomial, and avoid Runge's phenomenon.

First, define $k_i = C^{"}(t_i)$ for $i = 1, 2, ..., n-1$, $C_i(t_i) = w_i$, $C_i(t_{i+1}) = w_{i+1}$ and $k_0 = 0, k_n = 0$. And it Lagrange form for $C^{"}(t_i)$ is

$$C_i^{"}(x) = \frac{k_{i+1}(x - t_i)}{(t_{i+1} - t_i)} + \frac{k_i(t_{i+1} - x)}{(t_{i+1} - t_i)} \tag{10}$$

Then the $C_i^{'}(x)$ and $C_i(x)$ are given as

$$C_i^{'}(x) = \frac{k_{i+1}(x - t_i)^2}{2(t_{i+1} - t_i)} + \frac{k_i(t_{i+1} - x)^2}{2(t_{i+1} - t_i)} + A_i + B_i \tag{11}$$

$$C_i(x) = \frac{k_{i+1}(x - t_i)^3}{6(t_{i+1} - t_i)} + \frac{k_i(t_{i+1} - x)^3}{6(t_{i+1} - t_i)} + A_i(x - t_i) + B_i(t_{i+1} - x) \tag{12}$$

where A_i and B_i are shown in equation (13) and (14).

$$B_i = \frac{w_i}{(t_{i+1} - t_i)} - \frac{(t_{i+1} - t_i)k_i}{6}, \tag{13}$$

$$A_i = \frac{w_{i+1}}{(t_{i+1} - t_i)} - \frac{(t_{i+1} - t_i)k_{i+1}}{6} \tag{14}$$

Therefore, C_i and $C_i^{'}$ are generated as following equation (15) and (16).

$$C_i(x) = \frac{k_{i+1}(x - t_i)^3}{6(t_{i+1} - t_i)} - \frac{k_i(x - t_{i+1})^3}{6(t_{i+1} - t_i)} + \left[\frac{w_{i+1}}{t_{i+1} - t_i} - \frac{(t_{i+1} - t_i)k_{i+1}}{6}\right](x - t_i) - \left[\frac{w_i}{(t_{i+1} - t_i)} - \frac{(t_{i+1} - t_i)k_i}{6}\right](x - t_{i+1}) \tag{15}$$

$$C_i^{'}(x) = \frac{k_{i+1}(x - t_i)^2}{2(t_{i+1} - t_i)} - \frac{k_i(x - t_{i+1})^2}{2(t_{i+1} - t_i)} + \frac{w_{i+1} - w_i}{t_{i+1} - t_i} - \frac{k_{i+1} - k_i}{6}(t_{i+1} - t_i) \tag{16}$$

Also, $C_i^{'}(t_i)$ requires the following condition.

$$C_{i-1}^{'}(t_i) = C_i^{'}(t_i) \quad i = 1, 2, \cdots, n-1$$

Then we can get equation (17).

$$C_i^{'}(t_i) = -\frac{1}{2}k_i(t_{i+1} - t_i) + \frac{w_{i+1} - w_i}{t_{i+1} - t_i} - -\frac{k_{i+1} - k_i}{6}(t_{i+1} - t_i) \tag{17}$$

By using $s_i = t_{i+1} - t_i$,and $d_i = \frac{w_{i+1} - w_i}{t_{i+1} - t_i}$, equation (17) has

$$C_i^{'}(t_i) = -\frac{1}{6}s_i k_{i+1} - \frac{1}{3}s_i k_i + d_i \tag{18}$$

$$C_{i-1}^{'}(t_i) = \frac{1}{6}k_{i-1}s_{i-1} + \frac{1}{3}k_i s_{i-1} + d_{i-1} \tag{19}$$

By $C_{i-1}^{'}(t_i) = C_i^{'}(t_i)$, then equation (20) is given.

$$\begin{cases} s_{i-1}k_{i-1} + 2(s_{i-1} + s_i)k_i + s_i k_{i+1} = 6(d_i - d_{i-1}) \\ k_0 = k_n = 0 \end{cases} \tag{20}$$

Bezier curve is widely used in computer graphics and other path smoothing method. It is a simple and practical way. However, distinguishing between control point and path point in path planning algorithm is more complicated.

In the EM algorithms, cubic splines interpolation is used in doing path smoothing algorithm so that the number of parameters does not increase. Regarding each point as one path point, the algorithm enhances the relevance and thus enhances the computing performance.

IV. SIMULATION RESULT

The simulation parameter is shown on Table.1, and the simulation result is shown in Fig. 4. As shown in Fig. 4, the square is the start point, the star is the end point, and the circle is the obstacle. After the path planning and smoothing, the curve is the algorithm result. We calculate the cost function by using the Pythagorean Theorem. When the path contacts the obstacle, its cost function will be multiplied 100 as a penalty. Thus we can always find the best cost without touching the obstacle.

TABLE 1
SIMULATION PARAMETERS

Parameters	Max Iteration(*MAXITE*)	Local Iteration(*LITE*)	Number of population	Number of Control Point(m)	Delta(*det*)	Rearrange threshold(T)	Penalty
Values	50	100	10	5	0.4	0.1	100

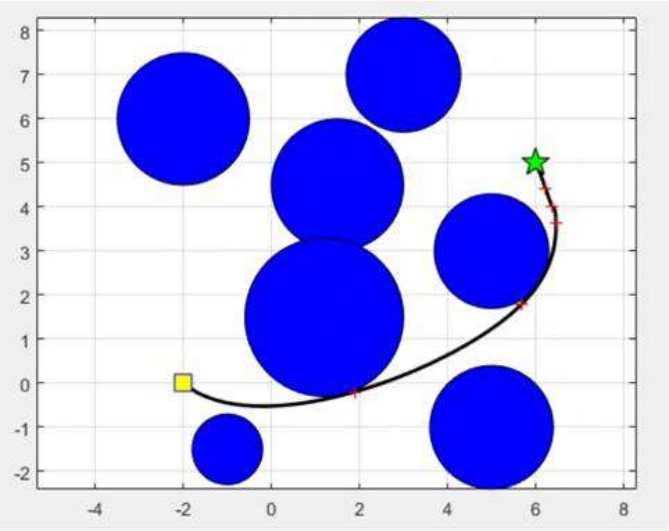

FIG.4. SIMULATIONAL RESULT

V. CONCLUSIONS

This paper has presented a path planning algorithm to solve the trade-off problem that is encountered in the traditional path planning method. Comparing two path smoothing method, Bezier curve and cubic splines interpolation, cubic splines interpolation is selected to smooth the path without increasing the number of parameters. By using the path smoothing method, the vehicle could go through the angle smoothly like reality.

ACKNOWLEDGEMENTS

This work was supported by the Taiwan Power Company, R.O.C. and the National Science Council of Taiwan, R.O.C., under Grants NSC 102-2221-E-003-011.

REFERENCES

[1] Dijkstra, E. W. (1959). "A note on two problems in connexion with graphs". *Numerische Mathematik* I: 269-271

[2] P. Hart, N. Nilsson, and B. Raphael, "A formal basis for the heuristic determination of minimum cost paths," *IEEE Trans. on Systems Science and Cybernetics, vol. 4, no. 2,* pp. 100-107, 1968.

[3] Yanrong Hu and Simon X. Yang, "A Knowledge Based Genetic Algorithm for Path Planning of a Mobile Robot," *Proceedings of the 2004 IEEE International Conference on Robotics and Automation,* New Orleans, USA, Pages 4350 – 4355, 2004.

[4] S.I. Birbil and S.-C. Fang, "An electromagnetism-like mechanism for global optimization," *J. Glob. Opt.*, vol. 25, no. 3, 263-282, 2003.

[5] S. I. Birbil, S.-C. Fang, and R.-L. Sheu, "On the convergence of a population -based global optimization algorithm," *J. Glob. Opt.*, vol. 30, no. 2, 301-318, 2004.

[6] Tsai, Chuen-Yih, Ho-Lung Hung, and Shu-Hong Lee. "Electromagnetism-like method based blind multiuser detection for MC-CDMA interference suppression over multipath fading channel." *Computer Communication Control and Automation (3CA), 2010 International Symposium on.* Vol. 2, pp. 470-475, 2010.

[7] J. C. Chen, "Partial transmit sequences for PAPR reduction of OFDM signals with stochastic optimization techniques," *IEEE Trans. Consumer Electron., vol. 56*, no. 3, pp. 1229-1234, Aug. 2010.

[8] Q. Wu, et al., "Training neural networks by electromagnetism-like mechanism algorithm for tourism arrivals forecasting," in *Bio-Inspired Computing: Theories and Applications (BIC-TA), 2010 IEEE Fifth International Conference on*, 2010, pp. 679-688.

[9] P. Wu, K. Yang, and Y. Hung, "The study of electromagnetism-like mechanism based fuzzy neural network for learning fuzzy if-then rules," *Knowledge-Based Intelligent Information and Engineering Systems*, pp. 907–907, 2005.

[10] Yaonan, Wang, Yang Yimin, Yuan Xiaofang, Yin Feng, and Wei Shuning. "A Model Predictive Control Strategy for Path-Tracking of Autonomous Mobile Robot Using Electromagnetism-Like Mechanism", *2010 International Conference on Electrical and Control Engineering*, 2010

[11] Kuo, C. L., Chu, C. H., Wu, Q., Li, X., Gao, L. and Li, Y., "Electromagnetism-like Algorithms for Optimized Tool Path Planning in 5-Axis Flank Machining," *Computers and Industrial Engineering*, Vol. 84, pp. 70-78, 2014.

[12] F.-K. Chang and C.-H. Lee, Design of Fractional PID Control via Hybrid of Electromagnetism-Like and Genetic Algorithms, *in Eighth International Conference on Intelligent Systems Design and Applications*, pp 525–530, 2008.

[13] P. Wu, K.-J. Yang, and B.-Y. Huang, "A Revised EM-like Mechanism for Solving the Vehicle Routing Problems," *in Proceedings of the Second International Conference on Innovative Computing, Information and Control*, pp. 181-184, 2007.

[14] C. C. Chang, C. Y. Chen, C. W. Fan, H. C. Chao and Y. H. Chou, "Quantum-Inspired Electromagnetism-Like Mechanism for Solving 0/1 Knapsack Problem." *in IEEE conference on ITCS*, pp.1-6, 2010.

[15] Yun, Shang. "Research of Big Data Analysis on Rough Set and Electromagnetism-Like Mechanism Algorithm." *in IEEE conference on CIT*, pp. 923-926 , 2014.

[16] C. Y. Chen, C. H. Chiu, and H. C. Chao, "Classical and Quantum-Inspired Electromagnetism-Like Mechanism and its Applications," *IET Control Theory & Applications*, vol. 6, no. 10, 2012, pp. 1424–33.

[17] Zhang, C., Li, X., Gao, L., and Wu, Q., "An improved electromagnetism-like mechanism algorithm for constrained optimization," *Expert Systems with Applications*, Vol. 40, No. 14, pp. 5621-5634, 2013.

[18] Kuo, C. L., Chu, C. H., Wu, Q., Li, X., Gao, L. and Li, Y., "Electromagnetism-like Algorithms for Optimized Tool Path Planning in 5-Axis Flank Machining," *Computers and Industrial Engineering*, Vol. 84, pp. 70-78, 2014.

[19] A. R. Forrest, "Interactive interpolation and approximation by Bezier polynomials" *Comput. J.*, vol. 15, no. 1, pp. 71–79, 1972.

[20] McKinley, Sky, and Megan Levine." Cubic spline interpolation." *College of the Redwoods*, 1998.

Antioxidant Activity of gossypitrin isolated from the petals of *Taliparititi elatum* (Sw.) Fryxell (Malvaceae) in Cuba

José González[1*], Armando Cuéllar[2], Pedro Abreu[3], Max Monan[4], Enmanuel Nossin[5], Frantz François-Haugrin[6]

[1]Department of Pharmacy, Faculty of Pharmacy and Foods, Cuba.
[2]REQUIMTE, Departamento de Química, Faculdade de Ciências e Tecnologia da Universidade Nova de Lisboa, 2829-516 Caparica, Portugal.
[3]ARVARNAM, Martinica.

Abstract— *Taliparititi elatum Sw. Fryxell (Malvaceae) is an endemic tree widely distributed in Cuba. The flowers are used in traditional medicine for the treatment of asthma. It was decided to search for any product responsible of this devoted activity. From the flower leaves (petals) it was isolated a flavonoid glycoside characterized as Gossypitrin and a sample was evaluated for its in vitro scavenging effects on reactive oxygen species (ROS) ($O^{\cdot-}$, $HO^{\cdot}$, HOCl, $ROO^{\cdot}$, and H_2O_2), reactive nitrogen species (RNS) ($ONOO^-$ and NO) and $ABTS^{\bullet+}$, $DPPH^{\cdot}$ radicals and Reducing Power assay. Additionally, two enzymatic assays (Inhibition of xanthine oxidase (XO) and Effect on XO activity) were also evaluated. In the scavenging assays the sample showed to be not effective against all assayed ROS and RNS, and displayed a weak activity in the DPPH and Reducing Power assays, but it displayed a good activity in the $ABTS^{\bullet+}$ assay (2, 14 mM). The enzymatic assays corroborated that Gossypitrin shows a weak activity on inhibition of XO. These results provide scientific support for the empirical use of the flowers of T. elatum as an antasthmatic medicine.*

Keywords— Taliparititi elatum, scavenging effect, reactive oxygen species, reactive nitrogen species, antioxidant activity.

I. INTRODUCTION

Flavonoids are among the most ubiquitous groups of plant secondary metabolites distributed in various foods and medicinal plants. They are largely planar molecules and their structural variation comes in part from the pattern of substitution: hydroxylation, methoxylation, prenylation, or glycosylation. Although they are sometimes found as their aglycones, flavonoid most commonly occur in plant materials as flavonoid *O*-glycosides, in which one or more hydroxyl groups of the aglycones are bound to a sugar, forming an acid-labile glycosidic O-C bond. There are certain hydroxyl groups in flavonoids that are usually glycosylated. These are the 7-hydroxyl group in flavones, flavanones, and isoflavones and the 3- and 7-hydroxyl groups in flavonols and flavanols. 5-*O*-Glycosides are rare for compounds with a carbonyl group at C-4, since the 5-hydroxyl group participates in hydrogen bonding with the adjacent carbonyl at C-4 (Larson, 1997). These polyphenols show biological properties through their free-radical-scavenging antioxidant activities and metal-ion chelating abilities. They are also known for their ability to inhibit enzymes such as protein kinase C, several protein-tyrosine kinases, or cyclic-dependent kinases (Akiyama et al., 1987; Wang et al., 2003; Frey et al., 2003) Flavonoids are converted to several other phenolic acids. Some of these metabolites have shown higher antioxidative and estrogenic activities (measured in vitro) than their parent compounds, for instance equal compared with daidzein (Rimbach et al., 2003).

Most interest has been focused on the antioxidant activity of flavonoids, which is due to their ability to reduce free radical formation and to scavenge free radicals. To establish the role of flavonoids as antioxidant in vivo, it is critical to understand the chemical nature of the absorbed forms in the circulation in vivo. The antioxidant efficacy of flavonoids in vivo is poorly documented, presumably because of the limited knowledge on their uptake and distribution in humans. Most ingested flavonoids are extensively degraded to various phenolic acids, some of which still possess a radical-scavenging ability (Rowland et al., 2003).

Gossypitrin is a flavonoid isolated and characterized from the flower leaves (petals) of *Taliparititi elatum* Sw. Fryxell (Malvaceae), a tree with a wide distribution in Cuba, that growth in any type of soil, particularly in swanpyones. It can get about 25 m of height. It shows peciolated leaves, to mentose-velvet like and heart-shaped at the basis. The flowers are big, yellow flower leaves that become reddish when old. The flowers are used as appetitive, emollient, sudorific and as excellent expectorant combined with the flowers of *Hibiscus rosa-sinensis*. The mixture is used in traditional medicine as expectorant and antasthmatic (Roig, 1974: Acosta y Rodríguez, 2006). The aim of the present study was to evaluate the

in vitro scavenging effects of a sample of gossypitrin on ROS ($O^{\cdot-}$, $HO^{\cdot}$, HOCl, ROO, and H2O2), RNS ($ONOO^{-}$ and NO) and DPPH radical

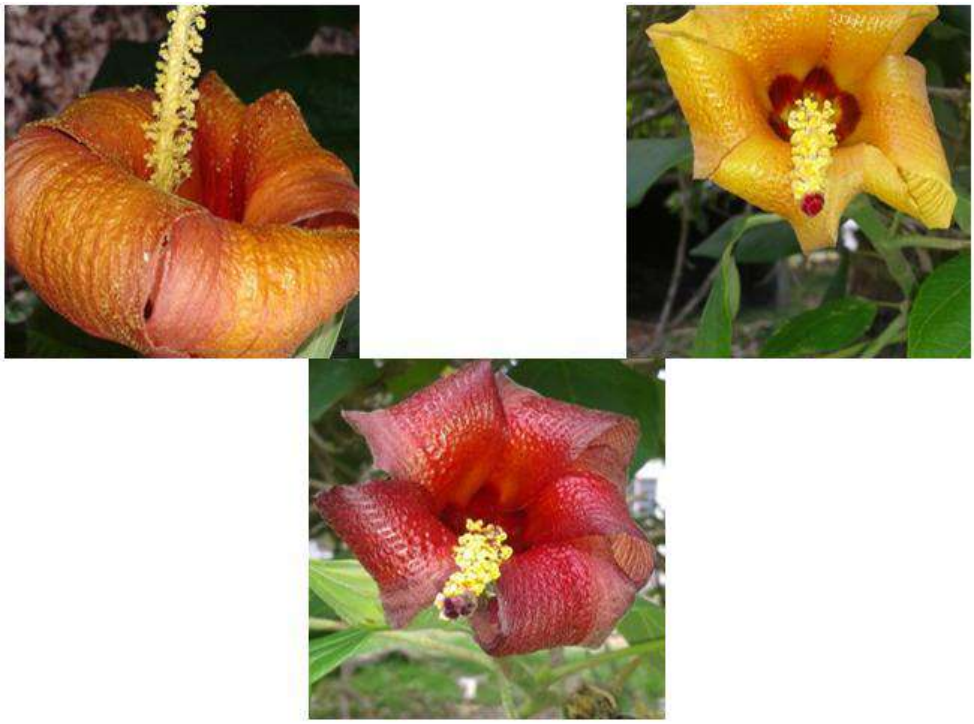

FIGURE 1. FLOWERS OF *T. ELATUM* SW

II. MATERIAL AND METHODS

2.1 DPPH assay

DPPH scavenging activity was measured according to the procedure described by Blois (Blois, 1958). Briefly, each test sample (100 mL) of various concentrations (0.015 – 0.500 mg/mL) was added to 900 mL of freshly prepared DPPH solution (0.004% in MeOH), and the mixture vortexed for 15 s. The decrease in absorbance at room temperature was determined at 515 nm after 30-45 min of incubation. All experiments were performed in triplicate. The inhibition percentage (%) of radical scavenging activity was calculated as $(1 – A_s/A_0) \times 100$, where A_0 and A_s are the absorbance of the control and sample, respectively, at 515 nm. α-tocopherol and quercetin were used as standards.

2.2 Radical Cation ABTS•+ scavenging activity

The radical cation $ABTS^{\bullet+}$ scavenging activity was evaluated according to the modified TEAC method of Re et al., 1999. $ABTS^{\bullet+}$ (7 mM) was dissolved in milli Q water and added topotassium persulfate to reach a 2.4 mM final concentration. The reaction mixture was left 16 h in dark at room temperature, and the radical cation solution was further diluted with water to give an absorbance value of 0.700 ± 0.03 at 734 nm. Samples were diluted with H_2O/EtOH so that after the addition of 15 mL to 1.485 mL of $ABTS^{\bullet+}$, a 20% - 80%decrease in the initial absorbance at 734 nm is observed. The decrease of absorbance was recorded at time intervals of 1, 2, 5, 10 and 15 min, for a range of 5-8 concentrations (0 to 20 mM final concentration after addition of $ABTS^{\bullet+}$) for each sample. Assays were performed in triplicate and solvent blanks were run in each assay. The percentage inhibition of absorbance at 734 nm was calculated and plotted as a function of sample concentration and that of the antioxidant standard Trolox (6-hydroxy-2,5,7,8-tetramethylchroman-2-carboxylic acid). The scavenging activity is estimated within the range of the dose–response curve of Trolox and expressed as the Trolox equivalent antioxidant capacity (TEAC), which is defined as the concentration (mM) of Trolox having the equivalent antioxidant capacity to a 1.0 mM or 1 mg/mL of the tested sample solution.

2.3 Reducing Power assay

Reducing power was determined according to the method of Oyaizu (Oyaizu, 1986). Samples (0.02–1.0 mg) were dissolved in 1.0 mL of milli Q water to which was added 2.5 mL of a 0.2 mM phosphate buffer (pH 6.6) and 2.5 mL of a 1% (w/v) solution of potassium ferricyanide. The mixture was incubated in a water bath for 20 min at 50 ^{o}C, followed by the

addition of 2.5 mL of a 10% (w/v) trichloroacetic acid solution. The mixture was then centrifuged at 5000 rpm for 10 min, and a 2.5 mL aliquot of the resulting upper layer was combined with 2.5 mL of Milli Q water and 0.5 mL of a 0.1% (w/v) $FeCl_3$ solution. The absorbance of the reaction mixture was read spectrophotometrically at 700 nm against a blank sample. The mean absorbances from three independent samples were plotted against concentration and a linear regression analysis was carried out to calculate the IC_{50} value, defined as the effective concentration at which the decrease in absorbance was 0.50 at 700 nm. α-tocopherol and quercetin were used as standards.

2.4 Assessment of scavenging activity against reactive oxygen species (ROS) and reactive nitrogen species (RNS)

For assessment of scavenging activity against ROS and RNS, the sample is dissolved in the buffer solution applied in each assay in order to achieve concentration values up to 10 mg of dried solid/mL. All determinations were performed in a microplate reader (Synergy HT, BIO-TEK), using spectrometric, fluorimetric or chemiluminiscence detection. Each study corresponds to four experiments performed in triplicate at 37 ºC.

2.4.1 Superoxide radical ($O^{\cdot-}$) scavenging assay

The $O_2^{\cdot-}$ scavenging activity was measured by monitoring the $O_2^{\cdot-}$ induced reduction of nitroblue tetrazolium chloride (NBT) to the blue chromogen diformazan (Fernandes et al., 2003). $O_2^{\cdot-}$were generated by the phenazine methosulphate (PMS)/NADH system. The reaction mixtures in the sample wells contained, in a final volume of 300 µL, the following reagents at the indicates final concentrations: NBT (43 µM), NADH (166 µM), extract at various concentrations (0-1.0 mg/mL) and PMS (2.7 µM). All reagents and extract were dissolved in 19 mM phosphate buffer, pH 7.4.

2.4.2 Hydroxyl radical ($HO^{\cdot}$) scavenging assay

The $HO^{\cdot}$ scavenging activity was measured by monitoring the $HO^{\cdot}$-inducing oxidation of luminol (Oosthuizen and Greyling, 2001) with modifications. $HO^{\cdot}$ was generated by a Fenton system ($FeCl_2$ /EDTA/H_2O_2). Reaction mixtures wells contained, in a final volume of 250 µL, the following reagents at the indicated final concentrations: 0.5 M Na_2CO_3 buffer, pH 10, luminol (20 µM), $FeCl_2$-EDTA (25 µM, 100 µM), extract at various concentrations (0-2.0 mg/mL) and H2O2 (3.5 mM). The iron salt was premixed with the chelator dissolved in water before addition to the reaction mixture.

2.4.3 Hypochlorous acid (HOCl) scavenging assay

The HOCl scavenging activity was measured by monitoring the HOCl-inducing oxidation of luminol, accordingly to a described procedure (Yildiz et al., 1998) with modifications. HOCl was prepared immediately before use by adjusting the pH of a 1% (v/v) solution of NaOCl to 6.2 with diluted sulphuric acid. The concentration of HOCl was further determined spectrophotometrically at 235 nm using the molar absorption coefficient of 100 $M^{-1} cm^{-1}$ (Aruoma, 1997). Reaction mixtures in the samples wells contained, in a final volume of 250 µL, the following reagents at the indicated final concentrations: 50 mM Na_2HPO_4 buffer, pH 12, luminol (250 µM), extract at various concentrations (0-400 µg/mL), and HOCl (25 µM).

2.4.4 Peroxyl radical ($ROO^{\cdot}$) scavenging assay

The $ROO^{\cdot}$ scavenging activity was measured by monitoring the decay in fluorescence due to the oxidation of fluorescein, accordingly to a described procedure known by oxygen radical absorbance capacity (ORAC) assay (Fernandes et al., 2004.). $ROO^{\cdot}$was generated by thermo decomposition of α-α'-azodiisobutyramidine dihydrochloride (AAPH). Reaction mixtures in the samples wells contained, in a final volume of 200 µL, the following reagents dissolved in 75 mM potassium phosphate buffer, pH 7.4, at the indicated final concentrations: fluorescein (61 nM), extract at various concentrations (00.01 mg/mL) and AAPH (19 mM). The scavenging effects are expressed as the relative trolox equivalent ORAC value, which is calculated by the following equation, where AUC represents the area under curve:

Relative ORAC value = [(AUC sample – AUC blank)/ (AUC trolox – AUC blank)] x (mass of trolox/mass of flavonoid)

2.4.5 H_2O_2 scavenging assay

The H_2O_2 scavenging activity was measured by monitoring the H_2O_2 -induced oxidation of lucigenin, accordingly to described procedure (Costa et al., 2005). Reaction mixtures in the samples wells contained, in a final volume of 250 µL, the following reagents at the indicated final concentrations: 50 mM Tris buffer, pH 7.4, lucigenin (3 mM), extract at various concentrations (0-10.0 mg/mL) and H2O2 (2%).

2.4.6 Nitric oxide ($^{\cdot}$NO) scavenging assay

The $^{\cdot}$NO scavenging activity was measured by monitoring the $^{\cdot}$NO- induced oxidation of non-fluorescent 4,5-diaminofluorescein (DAF-2) to the fluorescent triazolofluorescein, accordingly to described method (Nagata et al., 1999) with modifications. $^{\cdot}$NO was generated by the 3-(aminopropyl-1-hydroxy-3-isopropyl-2-oxo-1-triazene (NOC-5). A stock solution of 2.07 mM DAF-2 in DMSO was purged with nitrogen and stored at -20 ^{0}C. Working solutions of DAF-2 were diluted with the 50 mM phosphate buffer, pH 7.4, to 1/368 fold from the stock solution, and were placed on ice in the dark immediately before the determinations. The reaction mixtures in the samples wells contained, in a final volume of 300 µL, the following reagents at the indicated final concentrations: DAF-2 (5 µM), extract at various concentrations (0-200 µg/mL) and NOC-5 (10 µM).

2.4.7 Peroxynitrite ($ONOO^{-}$) scavenging assay

The $ONOO^{-}$scavenging activity was measured by monitoring the $ONOO^{-}$ - induced oxidation of dihydrorhodamine 123 (DHR 123) to rhodamine 123, accordingly to described procedure (Kooy et al., 1994) with modifications. $ONOO^{\cdot}$ was synthesized as described before (Beckman et al., 1994). Prior to each study, the concentration of the stock peroxynitrite solution was determined spectrophotometrically in 0.1 M NaOH ($\epsilon_{302\ nm}$ = 1670 $M^{-1}cm^{-1}$). A stock solution of 2.89 mM DHR 123 in dimethylformamide was purged with nitrogen and stored at -20 ^{0}C. Working solution of DHR 123 diluted from the stock solution were placed on ice in the dark immediately before the determinations. The buffer (90 mM sodium chloride, 50 mM sodium phosphate (pH = 7.4) and 5mM potassium chloride) was purged with nitrogen and placed on ice before use. At the beginning of the experiments, 100 µM DTPA was added to the buffer. Reaction mixtures in the samples wells contained, in a final volume of 300 µL, the following reagents at the indicated final concentrations: DHR 123 (5 µM), extract at various concentrations (0-200 µg/mL) and $ONOO^{-}$ (600 nM). In a parallel set of experiments the assays were performed in the presence of 25 mM $NaHCO_3$.

2.5 Enzymatic assays

2.5.1 Inhibition of xanthine oxidase (XO)

Superoxide radicals were generated by the X/XO system following a described procedure (Fernandes et al., 1999). The reaction mixtures in the sample wells consisted of xanthine (44 µM), XO (0.29 unit/mL), NBT (50 µM), and sample (5.2, 10.4, 20.8, 41.7, 83.3, and 166.7 µg/mL), in a final volume of 300 µL. Xanthine was dissolved in 1 µM NaOH, xanthine oxidase in 0.1 mM EDTA, and the other components in 50 mM phosphate buffer with 0.1 mM EDTA, pH 7.8. Allopurinol (Standard) was dissolved in DMSO. The reaction was conducted at room temperature for 2 min and initiated by the addition of XO.

2.5.2 Effect on XO activity

The effect of the sample on XO activity was evaluated by measuring the formation of uric acid from xanthine in a double-beam spectrophotometer (Shimadzu 2600), at room temperature. The reaction mixtures contained the same proportion of components as in the enzymatic assay for superoxide radical scavenging activity, except NBT, in a final volume of 600 µL. The absorbance was measured at 295 nm for 2 min. Additionally, this procedure was repeated with several concentrations of xanthine (11, 22, 44 and 88 µM and 73.2 µg/mL of sample, to get its inhibitory pattern.

III. RESULTS AND DISCUSSION

The present results showed for the first time that gossypitrin exhibit scavenging activity against some ROS and RNS and the inhibition of xanthine oxidase (Table 1). The flavonoid presented a diverse capacity for scavenging all ROS and RNS tested as indicated by the corresponding IC_{50} values, include in Table 1. All the reactive species were found at the µg/mL range. IC_{50} for $O_2^{\cdot-}$, HOCl and $^{\cdot}$NO were 28.9 ± 3.2, 1.17± 0.19 and 1.68 ± 0.12 µM of extract at various concentrations, respectively. No activity was detected in the H_2O_2 assay up to the sample concentration of 100 µM. The sample also showed a strong scavenging activity against $ONOO^{-}$ (IC_{50} = 1.09 ± 0.07 µM), which was reduced in the presence of $NaHCO_3$ (IC_{50} = 2.12 ± 0.15 µM).

The ORAC value obtained was 2.68 ± 0.22, indicating an ineffective capacity for scavenging ROO species when compared to the trolox value (1). The scavenging activity of the sample towards DPPH at various concentrations (0.015–0.500 mg/mL) was 18.376 µg/mL, which was indicative of a weak activity against the radical at least twice, compared with quercetin (8.052 µg/mL), but it is acceptable because the international guideline recommended that a value under 20 µg/mL

is considered to possess good antioxidant capacity. Reducing power assay of gossypitrin showed a value of 68.95 µg/mL, indicating a weak capacity for decrease in absorbance compared with quercetin (24.09 µg/mL) used as standard. The TEAC value of gossypitrin was 2.14 mM indicating two times lower activity against the radical cation $ABTS^{\bullet+}$, compared with quercetin (4.56 mM).

TABLE 1
IC_{50} VALUES CALCULATED FROM THE SCAVENGING ACTIVITY OF GOSSYPITRIN SAMPLE AGAINST DPPH, ABTS, REDUCING POWER, ROS, RNS AND ENZYMATIC ASSAYS

No.	Assay	Method	Standard		Gossypitrin
1	DPPH	Biois, 1958	Quercetin	8,05 µg/mL	18,376 µg/mL
2	TEAC	Re y col., 1999 (m)	Quercetin	4,56mM	2,14 mM
3	Reducing Power	Oyaizu, 1986	Quercetin	24,09 µg/mL	68,95 µg/mL
4	O_2	Fernandes y cl., 2003	Trolox	$1,83\pm0,09\times10^3$µM	28,9±3,2 µM
5	HOCL	Yildiz y col., 2004	Lipoic acid	2,37±0,13 µM	1,17±0,19 µM
6	$ROO^{\cdot}$	Fernandes y cl., 2004	Fluorescein (Trolox)	1	2,68±0,22 µM
7	$^{\cdot}NO$	Nagata y col., 1999	Rutin	0,52±0,02 µM	1,68±0,12 µM
8	$ONOO^{\cdot}$(1*)	Kooy y col., 1994	Ebselen	2,51±0,09 µM	1,09±0,07 µM
9	$ONOO^{\cdot}$(2*)	Kooy y col., 1994	Ebselen	16,0±1,9 µM	2,12±0,15 µM
10	H_2O_2	Costa y col., 2005	Lucigenin		(*)
11	$HO^{\cdot}$	Oosthuizen y Greyling, 2001	Luminol		(*)
12	Inhibic. XO	Fernandes y cl., 1999	Allopurinol	5,11±0,19 µM	52,8±2,2 µM

(*) No activity was detected in the H_2O_2 and $HO^{\cdot}$ assay up to the sample concentration of 100 mM. (1^* and 2^*) within and without the presence of $NaHCO_3$, respectively.

Enzymatic assay (Inhibition of xanthine oxidase) of various samples of gossypitrin (5.2, 10.4, 20.8, 41.7, 83.3, and 166.7 µg/mL) showed a value of IC_{50} (µM) = 52.8 ± 2.2, which was indicative of weak activity compared with Allopurinol (IC50 = 5.11 ± 0.19 µM) used as standard (Table 1).

In vitro antioxidant methods results for the evaluation of antioxidant activities of gossypitrin isolated from the ethanolic extracts of the petals of *T. elatum* were expressed in the IC_{50} values i.e., the quantity of flavonoid needed to scavenge 50 % of the radical produced in the reaction mixture. In addition, a chemical compound having low IC_{50} values is considered to possess strong antioxidant properties (Cuéllar & González, 2009; González & Cuéllar, 2010).

The role of ROS and RNS as the final common mediators of tissue damage in diseases of diverse etiologies emphasizes the wide range of therapeutic applications of antioxidants. The results demonstrated that this flavonoid exhibits an interesting antioxidant activity. It was able to quench DPPH radical, ABTS radicals and scavenge HOCl and $ONOO^{\cdot}$. The TEAC value of gossypitrin allow include this chemical compound into the eleven better secondary metabolites in the nature (flavonoids, phenylpropanoid and carotenoids), according with the results of Rice-Evans and Miller, 1996.

IV. CONCLUSION

On the basis of the results of the research, it is clear that gossypitrin have powerful antioxidant activity against various free radicals. The flavonoid showed antioxidant activity against all assayed radicals but with a different behavior in front of each tested radically specie. The results of the present investigation suggest, that the antasthmatic activity of the extracts of *T. elatum* used in Cuban traditional medicine, and recognized by the Ministry of Health (MINSAP), could be explained, at least in part, by their antioxidant and transition metal quelator properties. The bioguided isolation of the active constituents of *T. elatum* is being conducted, aiming the formulation of a safer and efficient drug. The ethanolic extracts from the petals of the flowers can be used as easily accessible source of natural antioxidants.

CONFLICT OF INTEREST

The authors declare no conflict of interest.

ACKNOWLEDGEMENTS

The authors acknowledge REQUIMTE, Departamento de Química, Faculdade de Ciências e Tecnologia da Universidade Nova de Lisboa (Portugal) for experimental support for this work. Sincere thanks also to Mathew S, González T, Costa D, Segundo M A, Fernandes E. for their valuable assistance.

REFERENCES

[1] Larson, R. A. Phenolic and enolic antioxidants. Naturally Occurring Antioxidants. Boca Raton: CRC press LLC; 100–109, 1997.
[2] Akiyama, T.; Ishida, J.; Nakagawa, S.; Ogawa, H.; Watanabe, S.; Itoh, N.; Shibuya, M.; Fukami, Y. Genistein, a specific inhibitor of tyrosine-specific protein kinases. J. Biol. Chem. 262: 5592–5595, 1987.
[3] Wang, S.; De Groff, V. L.;Clinton, S. K. Tomato and soy polyphenols reduce insulin-like growth factor-I-stimulated rat prostate cancer cell proliferation and apoptotic resistance in vitro via inhibition of intracellular signaling pathways involving tyrosine kinase. J. Nutr. 133:2367–2376, 2003.
[4] Frey, R. S.; Singletary, K. W. Genistein activates p38 mitogen activated protein kinase, inactivates ERK1/ERK2 and decreases Cdc25C expression in immortalized human mammary epithelial cells. J. Nutr. 133: 226–231, 2003.
[5] Rowland, I.; Faughnan, M.; Hoey, L.; Wahala, K.; Williamson, G.; Cassidy, A. Bioavailability of phyto-oestrogens.Br. J. Nutr. 1: S45 – S58, 2003.
[6] Roig, J. T. Plantas Medicinales Aromáticas y Venenosas de Cuba. Editorial Científico Técnica, La Habana, 618-619, 1974.
[7] Acosta de la Luz, L. L.; Rodríguez Ferradá, C. A. Plantas medicinales. Bases para una producción sostenible. Agrinfor, Impresiones MINAG, 124-125, 2006.
[8] Blois MS. Antioxidant determination by the use of a stable free radical. Nature 181: 1199, 1958.
[9] Re R, Pellegrini N, Proteggente A, Pannala A, Yang M, Rice-Evans C. Antioxidant activity applying and improved ABTS radical cation decolorization assay. Free Radic Biol Med, 26: 1231, 1999.
[10] Oyaizu M. Studies on products of browing reaction prepared from glucosamine. Jpn J Nutr. 44: 307-314, 1986.
[11] Fernandes, E.,Toste S. A., Lima, J. L. F. C., Reis S. The metabolism of Sulindac enhances its scavenging activity against reactive oxygen and nitrogen species. Free Radical Biology and Medicine. 35, 1008-1017, 2003.
[12] Oosthuizen, M.M. J., Greyling, D. 2001. Hydroxyl radical generation: The effect of bicarbonate, dioxygen and buffer concentration on pH-dependent chemiluminiscence. Redox Report. 6, 105-116, 2001.
[13] Yildiz, G., Demiryurek, A.T., Sahin-Erdemli, I., Kauzik, I. Comparison of antioxidant activities of aminoguanidine, methylguanidine by luminol-enhanced chemilumiscence. British Journal of Pharmacology. 124, 905-910, 1998.
[14] Aruoma, O.I. Scavenging of hypochlorous acid by carvedilol and ebselen in vitro. General Pharmacology. 28, 269-272, 1997.
[15] Fernandes, E., Costa D., Toste, S,A., Lima, J.F.C., Reis, S. In vitro scavenging activity for reactive oxygen and nitrogen species by nonsteroidal antiinflammatory indole, pyrrole, and oxazole derivative drugs. Free Radical Biology and Medicine, 37, 1895-1905, 2004.
[16] Costa, D., Gomes, A., Reis. S., Lima J. L. F. C, Fernandes, E. Hydrogen peroxide scavenging activity by non-steroidal anti-inflamatory drugs. Life Sciences 76, 2841- 2848, 2005.
[17] Nagata, N., Mornose, K., Ishida, Y. Inhibitory effects of catecholamines and antioxidants on fluorescence reaction of 4,5-diaminofluorescein, DAF-2, a novel indicator of nitric oxide. Journal of Biochemistry 125, 658-661, 1999.
[18] Kooy, N. W., Royall, J.A., Ischiropoulos, H., Beckman, J. Peroxynitrite-mediated oxidation of dihydrorhodamine 123. Free Radical Biology and Medicine 16, 149-156, 1994.
[19] Beckman, J.S., Chen, J., Ischiropoulas, H., Crow, J.P. Oxidative chemistry of peroxynitrite. Methods in Enzimology 223, 229-240, 1994.
[20] Fernandes, E., Borges, F., Milhazes, N., Carvalho, F.D., Bastos M.L. Evaluation of superoxide radical scavenging activity of gallic acid and its alkyl esters using an enzymatic an non-enzymatic system. Toxicol. Lett. 109, 42, 1999.
[21] Cuéllar Cuéllar, A., González Yaque, J. Biological activities of Gossypitrin isolated from the flowers of *Taliparíti elatum* S.W. MBARARA University Medical Journal. Mbarara, Uganda. Volume 15. Pages 14-17. January 2009.
[22] González Yaque, J.; Cuéllar Cuéllar, A., Biological activities of Gossypitrin isolated from the flowers of *Taliparíti elatum* S.W. NCSI Magazine. Biological Sciencies. Special Edition 2010. Volume 41, 2010. ISSN: 0253-568.
[23] Rice-Evans CA and Miller NJ. Antioxidants activities of flavonoids as bioactive components of food. Biochemical Society Transactions. Vol 24. 790-795, 1996.

Experimental and Finite Element Analysis of Flow Behavior of 2A14 Aluminum Alloy during Multi-directional Forging

Ming Wang[1], Juan Wang[2], Wensheng Liu[3], Yunzhu Ma[4], Dongliang Liu[5], Lunwen Guo[6], Lanping Huang[7*], Boyun Huang[8]

[1-8]Science and Technology on High Strength Structural Materials Laboratory, Central South University, Changsha 410083, China

[7]School of Metallurgy and Environment, Central South University, Changsha 410083, China

Abstract— *The deformation flow behavior of 2A14 aluminum alloys during multi-directional forging (MDF) under various cumulative strains ($\sum\Delta\varepsilon$) has been investigated by combining experiment with finite element method (FEM). The forging process has been performed at 450^{o}C with a deformation speed of 0.15 mms^{-1} and a pass strain ($\Delta\varepsilon$) of 0.4. Numerical simulations of MDF using a commercial software (DEFORM-3D), have shown that the vortex, cross-flow and fold defect of flow lines of the forgings do not occur during deformation, and the degree of bent and inhomogeneity of flow lines also increase steadily with $\sum\Delta\varepsilon$ increases. The FEM analysis coincides well with experimental results. The effective strain in various areas of the forgings has been significantly enhanced during MDF. The dynamic recovery is dominant during deformation. The proportion of recrystallized grains and the degree of fragmentation of second phases in various areas of the annealed forgings increase with the increase of effective strain.*

Keywords— 2A14 aluminum alloy, Multi-directional forging, Flow behavior, Effective strain, DEFORM-3D.

I. INTRODUCTION

Severe plastic deformation (SPD), as an effective processing method to fabricate ultrafine or nanostructured metallic materials with excellent properties, has been the subject of intensive investigations over the last two decades [1]. Compared with high-pressure torsion (HPT), equal-channel angular pressing (ECAP) and accumulative roll-bonding (ARB), multi-directional forging (MDF) which involves repeating compression process with changing the axis of the applied strain in three orthogonal directions at each step to obtain fine-grained products and to improve their comprehensive properties, is the simplest and cost-effective method to fabricate bulk products for industrial applications [2-7]. Due to the repeating rotation of the loading direction with deformation passes during MDF, cumulative strain applied from various directions is very significant for the evolution of grain structure and flow behavior of the materials subjected to deformation. A large number of investigations on MDF have indicated that microstructure change during MDF, especially grain refinement, can be controlled by various process factors, such as strain pass, deformation temperature, strain rate, alloying elements, second phase, etc [8-13]. Sitdikov et al. have found that the grain size and its volume fraction in 7475 aluminum alloys during high-temperature multi-directional compression are obviously different from those subjected to uniaxial compression [14]. The reasons are that two deformation modes have different flow behaviors. However, conventional flow analysis only based on experiments is very difficult to use for explaining the deformation behavior very clearly because the flow of metallic materials cannot be observed, so the application of finite element method (FEM) simulation offers convenience to flow analysis of MDF, which makes flow lines behaviors can be seen [15]. Park et al. have predicted metal flows and volume change during die-forging with the rigid-plastic finite element analysis and successfully designed the preform for precision forging of an asymmetric rib-web component [16]. Petrov et al. have applied QFORM-3D for the numerical investigations of the metal flow of isothermal forging and determined the optimum process conditions for isothermal enclosed die forging to fabricate A92618 aluminum alloy part with irregular shape [17]. Otherwise, Zhang et al. investigated the influence of forging process parameters on the distribution of flow lines in 7075 aluminum alloy disk workpiece with complex shape [18]. However, there is almost no work on the flow behaviors of the whole metallic products. Therefore, in this work, the MDF process of 2A14 aluminum alloys has been investigated by finite element software-DEFORM 3D, and the obtained results on the flow behaviors are compared with those obtained by experimental investigations on MDF process.

II. FINITE ELEMENT ANALYSIS

A commercial finite element method (FEM)-code (DEFORM-3D) was used to investigate plastic deformation of 2A14 aluminum alloys during MDF. In the numerical simulations reported here the initial dimension of the billet was 15 mm×12.5 mm×10 mm [14]. The dimensions of the upper and lower anvils of the die were 60 mm in diameter and 20 mm

in length. The FE model of MDF was established by importing three-dimensional images constructed with the CAD software Pro/ENGINEER to DEFORM-3D software. The material of anvils was Inconel 718 alloy. 2014 aluminum alloy was chosen for the forged material. The mesh was generated according to absolute density. The initial mesh with the maximum edge length of 0.3 mm and its size ratio was 1:1, while the final mesh with the minimum edge length of 0.1 mm and its size ratio was 3:1. The isothermal and deformation stages were included in each MDF pass. In the isothermal stages, the initial die temperature and ambient temperature both were 450 ^{o}C, while the initial billet temperature was 25 ^{o}C. Heat transfer coefficient was set to 1 $kWm^{-2}K^{-1}$ and the isothermal time was 8 minutes. In the forging stage, heat transfer coefficient was set to 11$kWm^{-2}K^{-1}$ and the deformation speed 0.15mms^{-1}. A constant friction factor of (m=0.3) was used to define the friction condition at the die-billet interface because this value is often used for hot forging. The forging process ended when the height of the billet was 10 mm. The MDF process was shown in Fig. 1. The initial length (Lx_0), width (Ly_0) and height (Lz_0) of the billet were 12.5 mm, 10 mm and 15 mm, respectively. The pass strain $\Delta\varepsilon$ was all 0.4 and the accumulate strain $\sum\Delta\varepsilon$ was 3.6. In the simulation, the die was considered as a rigid body, while the billet as a rigid-plastic material. The analysis of flow line, effective strain and stress were carried out by the DEFORM-3D software.

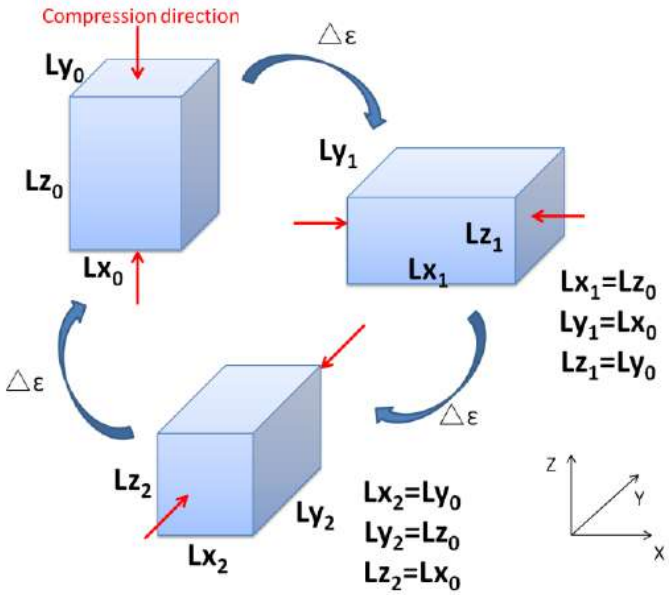

FIGURE. 1: SCHEMATIC ILLUSTRATION OF THE MULTIDIRECTIONAL FORGING (MDF) OF 2A14 ALUMINUM ALLOYS

III. EXPERIMENTAL PROCEDURE

The raw materials used in this work were commercial 2A14 aluminum alloy rods (supplied by Southwest Aluminum (group) Company Ld. China). Its actual chemical composition is 4.76 wt.% Cu, 0.66 wt.% Mg, 0.43 wt.% Si, 0.87 wt.% Mn, 0.20 wt.% Fe and balance Al. The rectangular samples with dimensions of 15 mm×12.5 mm×10 mm were cut from the same part of 2A14 aluminum alloy rods. After being homogenized at 495^{o}C for 12 hours followed by water quenching at room temperature, the samples were alternately forged with loading direction changed through 90°on high-temperature universal testing machine (WSM-200kN) with a deformation speed of 0.15 mms^{-1}. MoS2 was used as high-temperature lubricant between the interface of the anvil and the samples during deformation to alleviate inhomogeneous deformation. After each MDF pass, the sample was quickly quenched, patched and rotated for the next pass. Maximum 9 passes were used. Before MDF, the dies and samples were annealed in an electrical resistance at 450^{o}C for 1 h and 8 minutes, respectively. The material and dimension of the dies were the same as those used for FEM. To observe the recrystallization of the forged samples, the annealing treatment was carried out at 500^{o}C for 1 h. The T6 aging treatment was conducted by holding the annealed samples at 160°C for 12 h followed by air cooling for the micro-hardness measurement.

The central cross-sections of the samples parallel to the last loading axis were used for FEM and microstructural analysis. The schematic illustration was shown in Fig.2. Microstructural analysis was performed by optical microscopy (OM, Leica DFC 500) and scanning electron microscopy (SEM, FEI Nova Nano 230). The polished samples prepared for the low- and high-magnified OM were etched in 50% NaOH solution and Kerr agent containing 5 ml HNO_3, 2 ml HF, 3 ml HCl and 190 ml water, respectively. The micro-hardness measurement was performed using a typical Vickers hardness tester with an

applied load of 1 kg for a dwell time of 15 s and 8 spots for each sample were selected, and then average value and standard deviation were calculated.

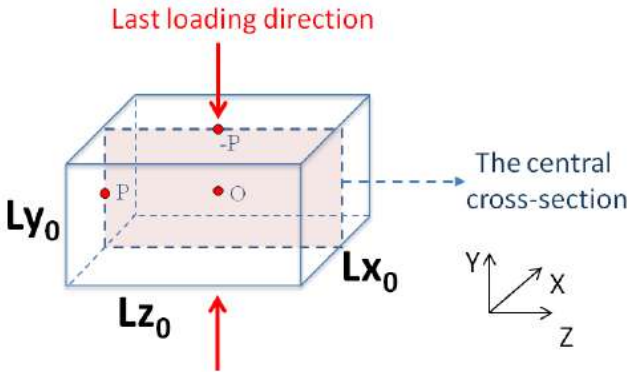

FIGURE. 2 VIEWING PLANE OF 2A14 ALUMINUM ALLOYS PROCESSED BY MDF AND ANALYTICAL PLANE OF FEM

IV. RESULTS AND DISCUSSION

4.1 Forging process

The FEM-simulated and experimental stress–strain curves of 2A14 aluminum alloys during the first MDF pass are shown in Figure 3. It can be seen that the two flow stress-strain curves are remarkably similar and both exhibit sharp stress peak just after yielding, followed by work softening. The experimental curve shows a steady stress with a significant decrease after $\Delta\varepsilon$ beyond 0.1. In contrast, the FEM-simulated curve presents a steady-state-like flow behavior. The difference of the flow stresses between FEM and experiments was mainly attributed to the constitutive equation used for 2A14 aluminum alloy in this work neglecting the softening of materials. Nevertheless, the subtle difference has little impact on the simulation results of flow line and effective strain distribution during MDF process.

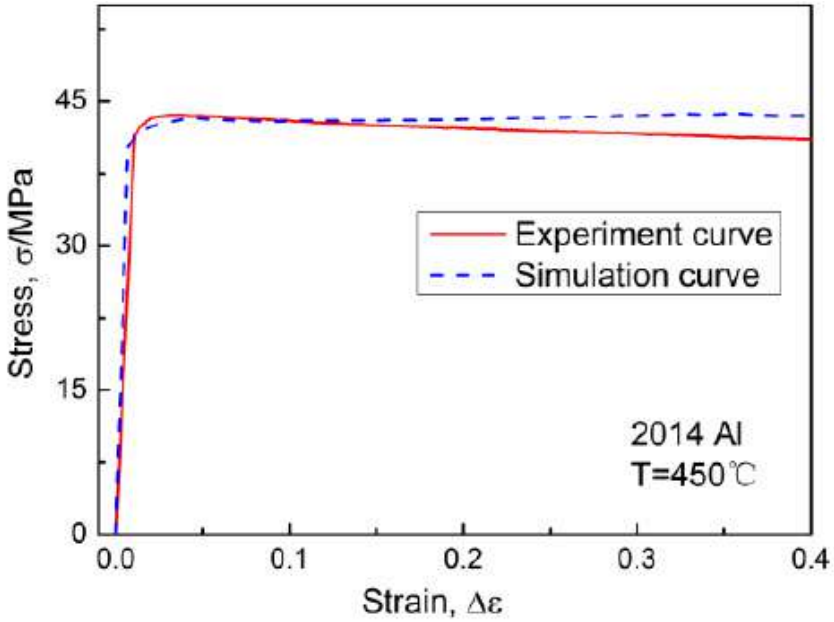

FIGURE 3 FEM-SIMULATED AND EXPERIMENTAL STRESS–STRAIN CURVES DURING THE FIRST MDF PASS OF 2014 ALUMINUM ALLOYS AT 450^{o}C AND AT A DEFORMATION SPEED OF 0.15 mms^{-1}

Figure 4 presents the appearances of the billets during MDF obtained by experiments and FEM. The experimental results show that the shapes of samples before and after MDF remain unchanged basically. However, there are some bulges in x direction and z direction, which are caused by the friction between billets and anvils. With the increase of forging passes, the bulges have a trend to become more obvious. The FEM analysis coincides well with experimental results, which indicates that the selected parameters used for the FEM analysis are suitable for the simulation of MDF process of 2A14 aluminum alloy.

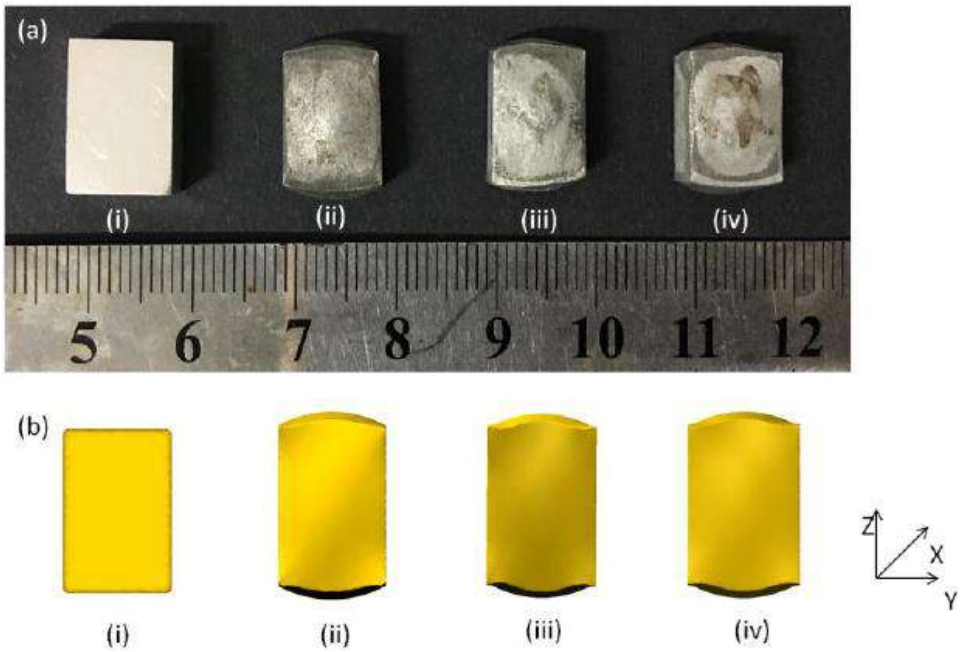

FIGURE 4 APPEARANCES OF THE 2A14 ALUMINUM ALLOY BILLETS DURING MDF OBTAINED BY (a) EXPERIMENTS AND (b) FEM: (i) BEFORE MDF; (ii) ∑Δ ε=1.2; (iii) ∑Δ ε=2.4; (iv) ∑Δ ε=3.6

4.2 Effects of cumulative strain on flow lines

To keep tracking of the materials flow during MDF, a flow-net technique was used in the FEM simulation. The flow lines distribution of the cross section of 2A14 aluminum alloys under various cumulative strain during MDF are shown in Figure 5. In Figure 5(a), the size of mesh was 0.42×0.42 mm, which was generated by setting the initial lateral and vertical flow lines. With the increase of cumulative strain, the vortex and outcrop defects did not exist, but flow lines in some areas were obviously bended, which led to the formation of considerable distorted meshes. When ∑Δ ε=0.4 (shown in Fig.5(b)), the billet was only subjected to compressed deformation in the axial direction, so the vertical flow lines were slightly bended toward the outer edge, and the lateral flow lines were bended toward the corners nearby. The meshes were stretched and the deformation extent in the center was relatively large, while the deformation extent on the surface between the die and billet were slightly small. The mesh deformation in various areas was obviously inhomogeneous. This inhomogeneity was attributed to non-uniform MDF deformation. The difference of deformation degrees during forging resulted into the formation of four deformation zones in the deformed billet, namely easy deformation zone I, shear deformation zone II, free deformation zone III and hard deformation zone IV, as shown in Fig. 5(c). The zone I and II showed an X-shape and were in the center of the sample, where high plastic deformation could be easily obtained. The zone III was close to the free end surfaces and exhibited two hemispheric shapes. During forging, the capacity of plastic deformation in this zone was between the easy deformation zone and hard deformation zone. The zone IV was close to the two anvils and its shape was similar to that of zone III. In this zone, the friction between the anvils and the sample impeded the flow of the metal leading to the hard-plastic deformation.

According to the distribution patterns of flow lines of the MDF samples, the meshes in the cross section could also be divided into the four deformation zones, as indicated in Fig. 5(b), (d), (e) and (f). When ∑Δ ε>0.4 (shown in Fig. 5(d)-(f)), the billet was subjected to multidirectional deformation, compared with uniaxial deformation, the characteristics of flow lines in this four zones were more apparent. In zone I, the meshes were square and its size slightly decreased compared with the initial ones, which were different from the tensile meshes normal to compression direction during uniaxial compression. The meshes in zone II were diamond and the bend degree of flow lines increased with cumulative strain increased. The meshes in zone III were also square, which were similar to those in zone I, and the mesh size slightly increased with cumulative strain increased. When ∑Δ ε=3.6 (shown in Fig. 3(d)), the mesh size was equal to that of the initial mesh. In zone IV the meshes were stretched along compression direction and mesh density also increased with cumulative strain increased. Compared with the free forging process, MDF changed flow lines distribution in zone IV and enhanced the degree of deformation. Therefore, the inhomogeneous degree of the formed meshes gradually increased with the evolution of flow lines during MDF.

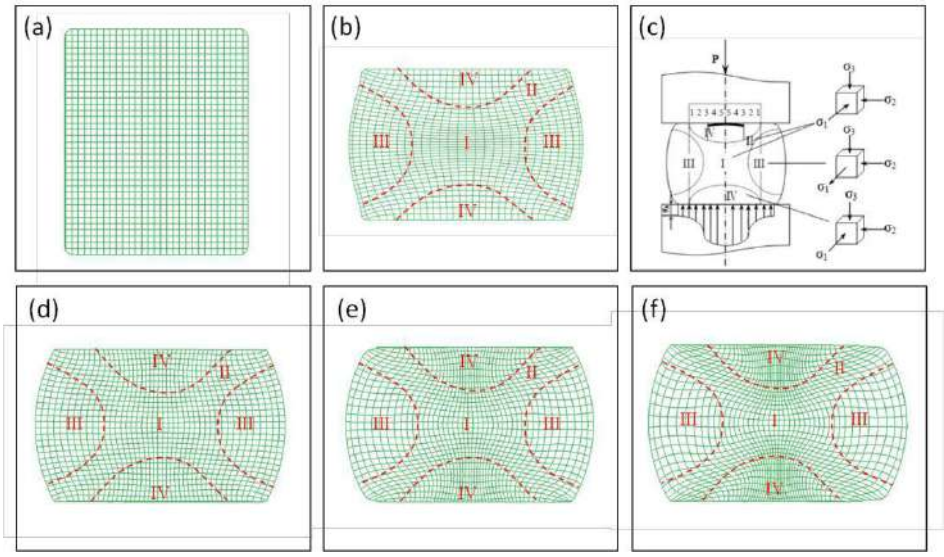

FIGURE 5: CROSS SECTIONS OF THE SIMULATED FLOW LINES OF 2A14 ALUMINUM ALLOYS PROCESSED BY MDF UNDER VARIOUS CUMULATIVE STRAINS: (a) ΣΔε=0; (b) ΣΔε=0.4; (c) SCHEMATIC DIAGRAM OF FOUR DEFORMATION ZONES DURING MDF; (d) ΣΔε=1.2; (e) ΣΔε=2.4 (f) ΣΔε=3.6

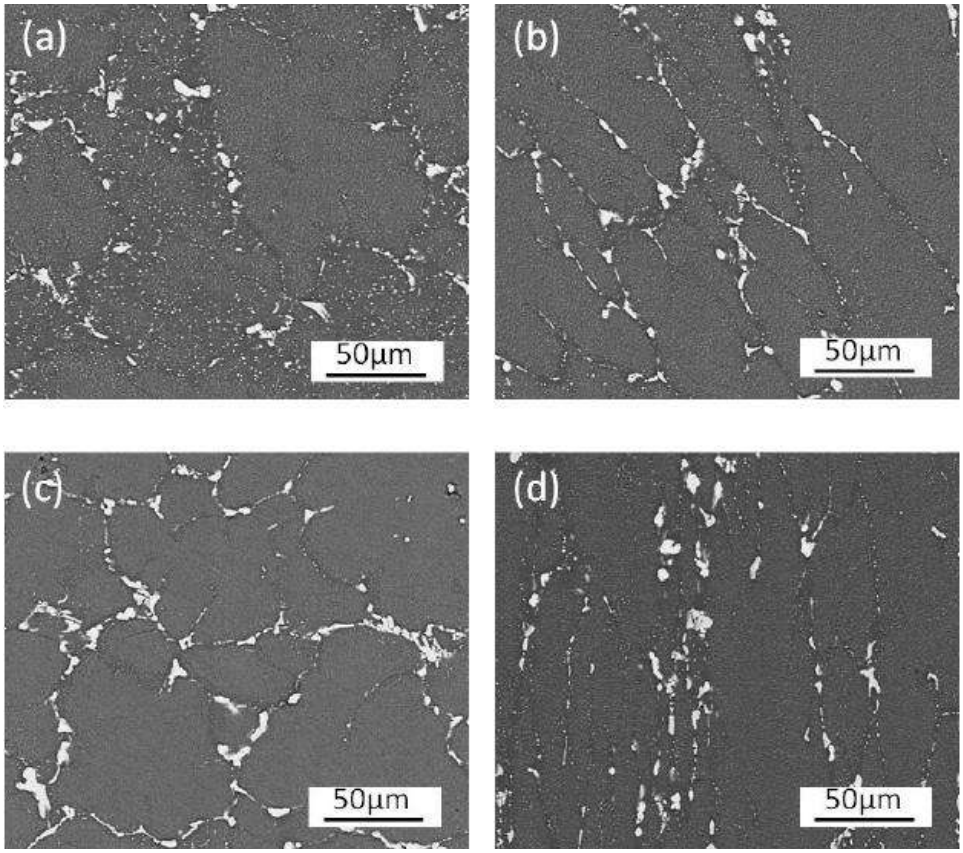

FIGURE 6: SEM IMAGES OF 2A14 ALUMINUM ALLOYS PROCESSED BY MDF IN DIFFERENT ZONES WITH ΣΔε=3.6: (a) Zone I; (b) Zone II; (c) Zone III; (d) Zone IV

Figure 6 presents the SEM images of the 2A14 aluminum alloy obtained by MDF. As shown in Fig. 6, the intensity and orientation distribution of flow lines of the 2A14 aluminum alloy forgings coincided well with the simulated results. The high magnified SEM images were described as follow: the grains in zone I (shown in Fig. 6(a)) were repeatedly tensioned and compressed, so the second phase particles were completely broken. Besides, a great number of second phase particles existed in grain interiors. In zone II flow lines were bent and the direction along which the grains were stretched was at a 45° to compression direction. The grains in zone III were near isometric, which corresponds to the almost unchanged meshes in

this zone during MDF process. On the contrary, the grains in zone IV were stretched along compression direction and their distortion degree was large. During MDF process, the position of zone III and zone IV were exchanged, so there were some broken second phase particles along grain boundaries in hard-plastic deformation zone IV. Since the flow lines of aluminum alloy forgings have obvious effects on their mechanical properties, the control of flow lines is always one of the key in the production of forgings [18]. The accurate prediction for flow lines during MDF provides a convenient and effective way for the control of flow lines in the practical forging process.

4.3 Effects of cumulative strain on effective strain

Figure 7 shows the effective strain distribution of the deformed 2A14 aluminum alloy workpieces with various cumulative strains during MDF. It can be seen that the distribution of the effective strain is inhomogeneous in the workpieces and the values of the effective strain gradually increase with the increase of cumulative strain. Large deformation occurs in the center and corners of the workpiece, while the plastic deformation is very difficult at the regions between the workpiece and the die due to high friction. In addition, it can be also seen from the strain values that the strain level in the larger cumulative strain is the higher. Overall, the values of effective strain gradually decrease from the center (point O in Fig. 2) toward the contact surface (point P in Fig. 2) and the edge (point –P in Fig. 2). The quantitative comparison of the effective strain from point –P to point O, then to point P of the deformed workpieces with various cumulative strains is shown in Fig. 8. It can be found that the minimum value of the effective strain is 0.428, and its maximum value in the center with large deformation is 0.843 when $\sum\Delta\varepsilon=0.4$. The effective strain in various regions continuously accumulates with increasing the total cumulative strain. When $\sum\Delta\varepsilon=3.6$, the minimum value of the effective strain is 1.94, and its maximum value in the center is up to 6.9. This means that the MDF process can obviously enhance the effective strain in various regions, and thus improve the microstructure and properties of the 2A14 aluminum alloys. Meanwhile, when the workpiece is subjected to uniaxial compression ($\sum\Delta\varepsilon=0.4$), the minimum value of the effective strain is distributed at the contact surface of the workpiece (point P), when subjected to MDF ($\sum\Delta\varepsilon>0.4$), its minimum value is alternately distributed at the contact surface (point P) and the edge (point –P). Therefore, the distribution of the effective strain during MDF exhibits different characteristics compared with uniaxial compression. It is favorable for improving the deformation characteristic of hard deformation zone at the contact area between the workpiece and the die by steadily changing the compression direction during forging.

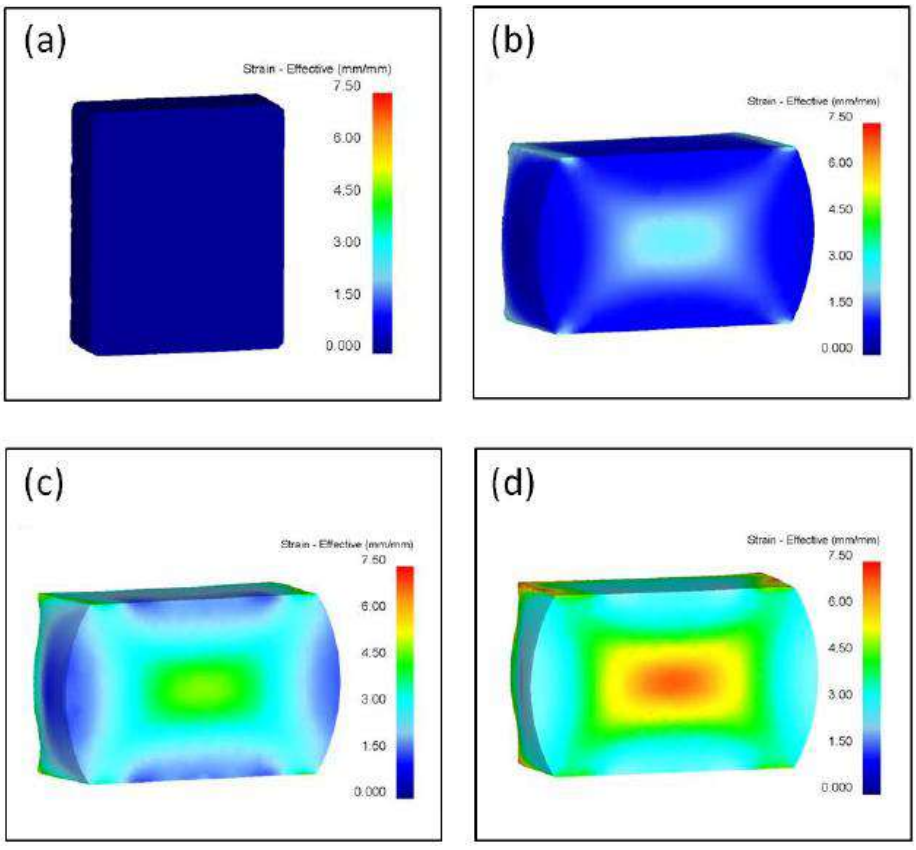

FIGURE 7 DISTRIBUTION OF EFFECTIVE STRAIN IN CROSS SECTION OF 2A14 ALUMINUM ALLOYS PROCESSED BY MDF WITH VARIOUS CUMULATIVE STRAINS: (a) $\Sigma\Delta\varepsilon=0$; (b) $\Sigma\Delta\varepsilon=1.2$; (c) $\Sigma\Delta\varepsilon=2.4$; (d) $\Sigma\Delta\varepsilon=3.6$

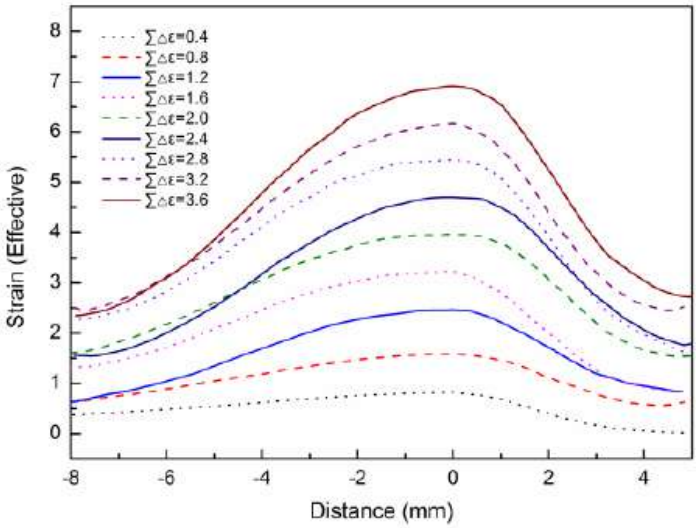

FIGURE 8: RELATIONSHIP BETWEEN EFFECTIVE STRAIN AND THE DISTANCE FROM THE EDGE OF THE DRUM SHAPE (POINT –P) TO THE CENTER (POINT O), THEN TO THE CONTACT SURFACE (POINT P)

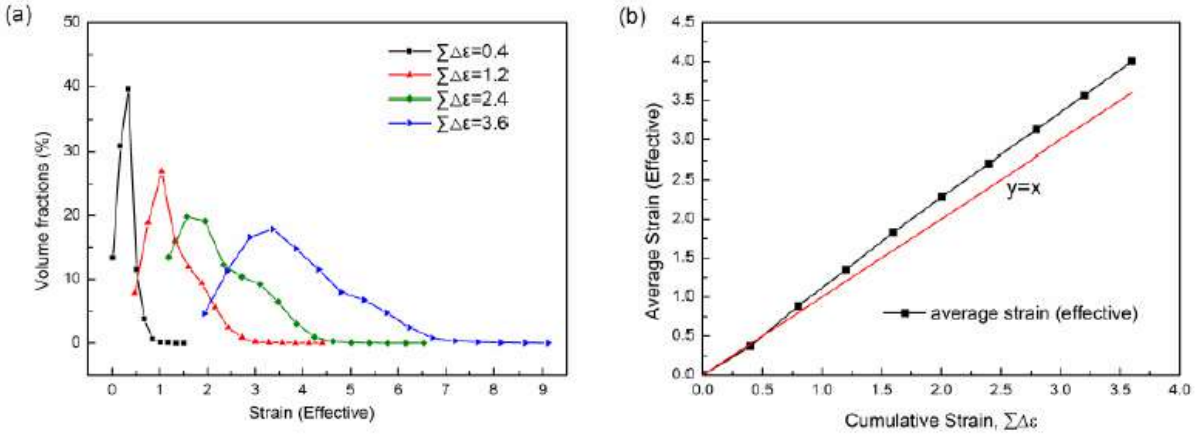

FIGURE 9: (a) EVOLUTION OF THE VOLUME FRACTION OF EFFECTIVE STRAIN WITH AVERAGE EFFECTIVE STRAIN; (b) EVOLUTION OF AVERAGE EFFECTIVE STRAIN WITH CUMULATIVE STRAIN

To further investigate the distribution of the effective strain during MDF, the analysis of the volume fraction of the effective strain and average effective strain are also carried out. Figure 9(a) shows the relationship between the volume fractions of the effective strain and cumulative strain of 2A14 aluminum alloy during MDF. With cumulative strain increases the effective strain in various areas are all enhanced but its heterogeneity also gradually increases. It can be also seen in Fig. 9(b) that the distribution range of the effective strain also becomes wider and the average effective strain is also higher. When $\sum\Delta\varepsilon>0.6$, the average effective strain is higher than the total cumulative strain and the difference between them becomes larger. This means that the steadily increase of cumulative strains can enhance the mobility of metals in hard deformation region. Therefore, it is a feasible way for enhancing the properties of the forgings by steadily increasing cumulative strain during MDF, but how to improve its homogeneity needs to be further studied in the future.

4.4 Effects of cumulative strain on recrystallization microstructure

Figure 10 shows the optical microstructures of zone I, II, III and IV of the deformed and annealed forgings. When $\sum\Delta\varepsilon=3.6$, it can be seen from Fig. 10(a) that the microstructure exhibits the characteristic of dynamic recovery and the deformed microstructures at different regions are obviously different. The size and appearance of grains coincide well with the simulation results of flow lines. As above mentioned, the value of effective strain in these four zones are ranged as follows: I>II>IV≈III. This shows that the degree of fragmentation of second phase particles gradually increases with the increase of effective strain. To further investigate the recrystallization of 2A14 aluminum alloy forgings, the optical microstructures of the annealing samples are shown in Fig. 10(b). It can be found that partial recrystallized grains exist on the boundary of the initial grains, and the recrystallization in various regions is also different. The size of recrystallized grains gradually decreases with the increase of cumulative strain, while volume fraction increases. The difference of effective strain in various

regions is mainly responsible for the inhomogeneity of recrystallization. It is generally believed that dynamic recrystallization does not occur in aluminum alloys due to its high fault energy, but recently some work have shown that the distinct dynamic recrystallization microstructure can be found during the compression deformation of some Al-Zn-Mg-Cu and Al-Cu-Mg-Ag aluminum alloy systems [19-22]. In 2A14 aluminum alloys the dislocation easily moves and cross slips, so the steady sub-microstructure can be formed during deformation process, and thus continuous dynamic recrystallization only occurs in the range of sub-grains [23]. Dynamic recovery has a predominant role in the MDF of 2A14 aluminum alloys, while dynamic recrystallization is difficult to proceed completely. After annealing treatment, the energy stored in sub-grain nearby is released, so continuous dynamic recrystallization takes place and recrystallized grains completely grow up. The different of effective strain results in the difference of the accumulation and the degree of entanglement of the dislocation in various regions, and thus leads to the difference of the recrystallization nucleation rate. Therefore, the fraction of recrystallization is also non-uniformly distributed.

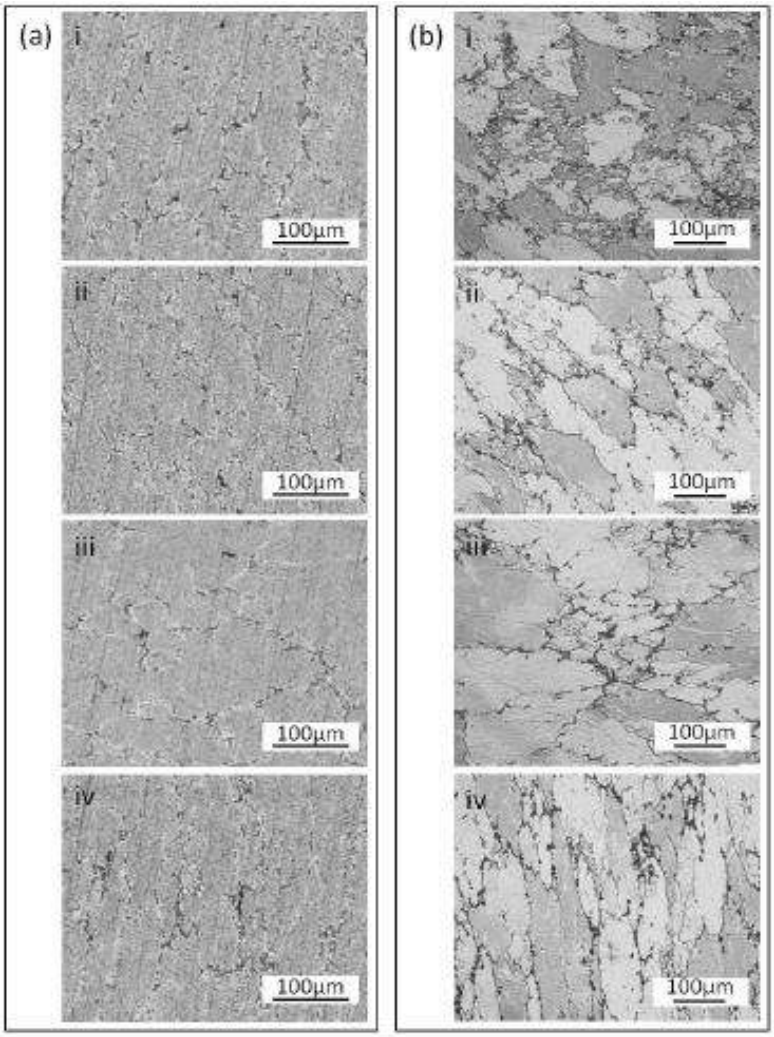

FIGURE 10: OPTICAL MICROSTRUCTURES OF THE DEFORMED (a) and annealed (b) 2A14 aluminum alloys obtained by MDF in different zones with ∑Δε=3.6: (i) Zone I; (ii) Zone II; (iii) Zone III; (iv) Zone IV

The inhomogeneity of the strain increases with the increase of ∑Δε in the forging process, but its homogeneous degree can be improved with the increase of ∑Δε. In order to evaluate the relationship between mechanical property and strain during MDF process, the Vickers hardness in various zones of the center interface of this alloy was measured. As shown in figure 11, the microhardness values in various zones are slightly different due to the difference of deformation degree. The microhardness values are ranged as followed: I>II>IV≈III, which coincide well with the simulation results of effective strains. This suggests that the distribution of equivalent strain simulated by FEM can predict the changing trends of the hardness. Meanwhile, the difference of the microhardness in various zones gradually decreases with the increase of cumulative strain. This means that the inhomogeneity of deformation of 2A14 aluminum alloy during forging can be improved by increasing ∑Δε.

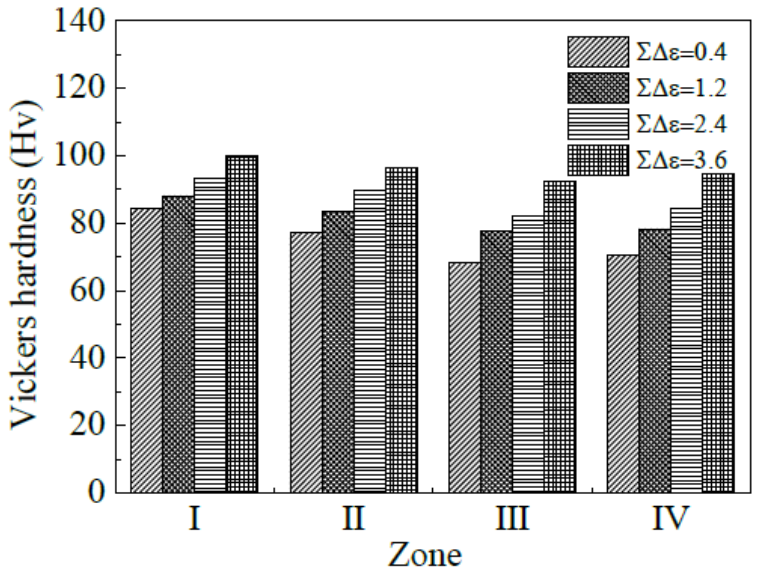

FIGURE 11: DISTRIBUTION OF VICKERS HARDNESS IN FOUR DEFORMATION ZONES FOR 2A14 ALUMINUM ALLOYS WITH DIFFERENT NUMBERS OF MDF PASSES

V. CONCLUSION

In this work, the deformation flow behavior of 2A14 aluminum alloy processed by MDF has been investigated by combining experiment with finite element method (FEM). Experiments were carried out to validate the simulated results. The results are summarized as follow:

(1) The evolution with respect to the metal flow in 2A14 aluminum alloy forgings during MDF can be accurately simulated by FEM. With cumulative strain increases the heterogeneity of flow lines is obviously enhanced. The meshes in some areas are steadily stretched and flow lines are significantly bent.

(2) The effective strain in various areas of 2A14 forgings is steadily accumulated with the increase of cumulative strain.

When cumulative strain $\sum\Delta\varepsilon=3.6$, the minimum value of effective strain is 1.94, and its maximum value is up to 6.9 in the center with high deformation degree. It is favorable for the improvement of deformation capacity of hard deformation area by MDF.

(3) The degree of fragmentation of grains and second phases on the grain boundary is obviously enhanced with the steady accumulation of effective strain in various areas of 2A14 forgings. It can be effectively predicted that the refinement degree of grains and second-phase particles in various areas by using FEM to simulate the evolution of effective strain of the forgings.

(4) The dynamic recovery microstructure can be found in the 2A14 aluminum alloy forgings processed by MDF. After annealing treatment, the size of recrystallized grains gradually decreases while its volume fraction steadily increases with the increase of effective strain.

ACKNOWLEDGEMENTS

This work was primarily financial supported by the National Natural Science Foundation of China (Grant No. 51201186) and National High-technology Research and Development Program of China (863 Program) (Grant No. 2009AA034300) as well as State Key Laboratory for Powder Metallurgy and Science and Technology on High Strength Structural Materials Laboratory, Central South University.

REFERENCES

[1] R. Z. Valiez, R. K. Islamgaliev and I. V. Alexandrov, "Bulk nanostructured materials from severe plastic deformation," Prog Mater Sci. vol.45 (2), pp. 103-189, 2000.

[2] R. Yoda, K. Shibata, T. Morimitsu, D. Terada and N. Tsuji, "Formability of ultrafine-grained interstitial-free steel fabricated by accumulative roll-bonding and subsequent annealing," Scripta Mater. vol.65, pp. 175-178, 2011.

[3] A. A. Mazilkin, B. B. Straumal, M. V. Borodachenkova, R. Z. Valiev, O. A. Kogtenkova and B. Baretzky, "Gradual softening of Al-Zn alloys during high-pressure torsion," Mater Lett. vol.84, pp. 63-65, 2012.

[4] M. Zha, Y. Li, R. H. Mathiesen, R. Bjørge and H. J. Roven, "Microstructure evolution and mechanical behavior of a binary Al-7Mg alloy processed by equal-channel angular pressing," Acta Mater. vol.84, pp. 42–54, 2015.

[5] K. B. Nie, K. K. Deng, X. J. Wang, F. J. Xu, K. Wu, M. Y. Zheng, "Multidirectional forging of AZ91 magnesium alloy and its effects on microstructures and mechanical properties," Mater Sci Eng A. vol.624, pp. 157-168, 2015.

[6] M. R. Jandaghi, H. Pouraliakbar, M. Khanzadeh, G. Khalaj and M. Shirazi, "On the effect of non-isothermal annealing and multi-directional forging on the microstructural evolutions and correlated mechanical and electrical characteristics of hot-deformed Al-Mg alloy," Mater Sci Eng A. vol.657, pp. 431-440, 2016.

[7] D. Desrayaud, S. Ringeval and S. Girard, "A novel high straining process for bulk materials-The development of a multi-Pass forging system by compression along three axes," J Mater Process Technol. vol.172(1), pp. 152-158 , 2006.

[8] A. Danno, C. C. Wong, S. Tong, A. Jarfors, K. Nishino and T. Furuta, "Effect of cold severe deformation by multi directional forging on elastic modulus of multi functional Ti + 25 mol% (Ta, Nb, V) + (Zr, Hr, O) alloy," Mater Des. vol.31(6), pp. 61–65, 2010.

[9] H. Miura, G. Yu, X. Yang and T. Sakai, "Microstructure and mechanical properties of AZ61 Mg alloy prepared by multi directional forging," Trans Nonferrous Met Soc China. vol.20(7), pp. 1294-1298, 2010.

[10] H. Miura, T. Maruoka, X. Yang and J. J. Jonas, "Microstructure and mechanical properties of multi-directionally forged Mg–Al–Zn alloy," Scripta Mater. vol.66(1), pp. 49-51, 2012.

[11] O. Sitdikov, T. Sakai, H. Miura and H. Hama, "Temperature effect on fine-grained structure formation in high-strength Al alloy 7475 during hot severe deformation," Mater Sci Eng A. vol.516(1-2), pp. 180-188, 2009.

[12] O. Sitdikov, T. Sakai, A. Goloborodko and R. Kaibyshev, "Effect of pass strain on grain refinement in 7475 Al alloy during hot multidirectional forging," Mater Trans. vol.45(7), pp. 2232-2238, 2004.

[13] A. Belyakov, K. Tsuzaki, H. Miura and T. Sakai, "Effect of initial microstructures on grain refinement in a stainless steel by large strain deformation,"Acta Mater. vol.51(3), pp. 847-861, 2003.

[14] O. Sitdikov, T. Sakai, A. Goloborodko and H. Miura, "Grain fragmentation in a coarse-grained 7475 Al alloy during hot deformation," Scripta Mater. vol.51(2), pp. 175-179, 2004.

[15] A. N. Bramley and D. J. Mynors, "The use of forging simulation tools," Mater Des. vol.21(4), pp. 279-286, 2000.

[16] J. J. Park and H. S. Hwang, "Preform design for precision forging of an asymmetric rib-web type component," J Mater Process Technol. vol.187–188, pp. 595–599, 2007.

[17] P. Petrov, V. Perfilov and S. Stebunov, "Prevention of lap formation in near net shape isothermal forging technology of part of irregular shape made of aluminium alloy A92618," J Mater Process Technol. vol.177(1-3), pp. 218–223, 2006.

[18] Y. Q. Zhang, D. B. Shan and F. C. Xu, "Flow lines control of disk structure with complex shape in isothermal precision forging," J Mater Process Technol. vol.209(2), pp. 745-753, 2009.

[19] J. Zhou, T. J. Zhang, X. M. Zhang, G. L. Ma, F. Tian and L. Zhou, "The influence of forge mode on dynamic recrystallization for 7075 aluminum alloy during forging," Rare Metal Mater Eng. vol.33(8), pp. 827-830, (2004.

[20] T. Sakai, H. Miura, A. Goloborodko and O. Sitdikov, "Continuous dynamic recrystallization during the transient severe deformation of aluminum alloy 7475," Acta Mater. vol.57(1), pp. 153-162, 2009.

[21] S. Yang, D. Q. Yi, H. Zhang and S. J. Yao, "Flow stress behavior and processing map of Al-Cu-Mg-Ag alloy during hot compression," J Wuhan Univ Technol Mater Sci Ed. vol.23(5), pp. 694-698, 2008.

[22] X. Y. Liu, Q. L. Pan, Y. B. He, W. B. Li, W. J. Liang and Z. M. Yin, "Flow stress behavior and microstructure of Al-Cu-Mg-Ag alloy during hot compression deformation," Chin J Nonferrous Met. vol.19(2), pp. 201-207, 2009.

[23] J. P. Lin, X. Y. An and T. Q. Lei, "A dynamic recrystallization model of Al-alloys," J Univ Sci Technol Beijing. vol.15(30), pp. 262-266, 1993.

Investigation of Formation Laws of Clays Composition under High Pressures

Valeriy V. Seredin[1], Alexander V. Rastegaev[2], Vladislav I. Galkin[3], Panova E.G.[4*], Tatyana Yu. Parshina[5]

[1]Professor and Head of engineering geology department of Perm state national research university
[2]Professor of oil and gas geology department of Perm national research polytechnic university
[3]Head of oil and gas geology department of Perm national research polytechnic university
[*4]Professor of geochemistry department, institute of Earth science, Saint- Petersburg state university
[5]Graduate student of engineering geology, department of Perm state national research university

Abstract— *It is found experimentally, that while building-up of pressure applied to natural clay, observed is general tendency of clay fraction content decrease and pulverescent fraction content increase. In montmorillonite natural clay, granulometric changes progress more intensively, than in kaolinite one. Within the pressure range of 0 – 125MPa processes of change of natural clay fractional compositions progress more intensively, than at higher pressures. Under pressures within the ranges of 125-750MPa and 800-2200MPa revealed is different intensity of natural clay fractional compositions formation. Based on pressure index, three classes are defined; each is featuring different intensity of aggregation and dispersion processes progressing. While compression of natural clay defects are formed on crystallite surfaces, increasing energy potential of crude ground. Additional energy enables formation of molecular attractive forces, which cause particles aggregation.*

Keywords— Clay, Pressure, Granulometric Analysis, Fraction, Kaolin, Montmorillonite.

I. INTRODUCTION

Natural clay properties are defined, to a large extent, by specific area of particle active surface, which can be controlled by granulometric or micro-aggregative ground compositions. In the processes of sedimentation, diagenesis, hypergenesis and technogenesis, «primary» particles of natural clays are transformed to «secondary» particles, forming micro-aggregates.

The issues of micro-aggregates formation in grounds are presented in the following studies [Krivosheeva et al., 1977; Osovetsky, 1993; Osipov, Sokolov, 2013; Savko, 2015]. Thus, the consider of information on formation of granulometric and micro-aggregative composition of natural clays during the processes of their natural formation and transformation. In previously investigations the data on natural clays, exposed to technogenic effect by the following solutions $MgCl_2$, $CaCl_2$, KCl and NaCl [Seredin et al., 2013; Seredin, 2014]. Authors concluded that aggregation process is connected with concentration of salt solution and mineral composition of particles. «Primary» particles of natural clays, exposed to oil contamination are connected between each other by electrostatic forces, which are determined by contamination volume and type of hydrocarbons [Boiko et al., 2009; Seredin, Yadzinskaya, 2014; Ilic et al., 2016].

Effect of mechanical factor is of importance, for example, effect of pressure on formation of aggregates in dispersed crude grounds [Krivosheeva et al 1977; Stefani et al., 2014; Friedlander et al., 2016]. The studies carried out [Sergeev, 1946] exhibited, that under pressures to 200 MPa, observed is insignificant change of crude ground aggregative compositions. Under pressure of 300 MPa applied to pulverescent ground, content of fine sand fraction increased from 13% to 51%, pulverescent fraction from 5% to 23%, and clay one from 2,15% to 5,42%. Hence it appears, that formation of clay aggregates at natural conditions as the result of mechanical exposure, progresses in rather limited volumes. While testing of blanket loams under pressures of P=2000 MPa and P=3660 MPa analogous results were received [Sergeev, 1946 a]. Procedures of prediction of ground granulometric compositions regarding not only earthy grounds [Boiko et al, 2009], but moon ones as well [Korolyov, 2016] are being developed based on experimental investigations.

The above mentioned discloses, that issues of pressure effect on formation of natural clay micro-aggregative compositions are studied not thoroughly enough. In this connection, the aim of the study is investigation of formation of natural clay micro-aggregative compositions exposed to high pressure.

II. SUBJECT, TESTING METHODS AND INVESTIGATION PROCEDURES

Subjects of investigation are montmorillonite and kaolinite natural clays. Under the results of X-ray diffraction analysis, montmorillonite natural clay consists (mass. %) of: montmorillonite – 75; kaolin - 3,6; quartz - 11,4; albite - 6,7; calcite - 3,3. Kaolinite natural clay contains (mass. %): kaolin - 76,7; montmorillonite – 15,6; quartz - 7,7.

High pressure device (was developed and produced to apply pressure to clay samples (Fig 1). Test spaces of the device (pos. 3, Fig.1) were produced out of hard-alloy material, their area constituted S=0,75sm^2. Press PLG-20 mark was used as loading device.

Preparation of clay samples for granulometric analysis was provided as follows: initial clayey ground (powder) was grinded in mortar by pistil. It was followed by mounting of the ground sample of about 0,2 g mass in testing space (pos. 3, Fig.1) of the device. Then press (pos. 6, Fig .1) was used to apply vertical pressures to the ground under the following scheme: the first stage - initial material (P=0 MPa), the second and subsequent stages – vertical pressure was increased by P=10-50 MPa. Maximum pressure constituted P=2200 MPa. Then upper holder (pos. 2, Fig.1) traveled relative to lower holder (pos. 1, Fig.1) by 90° by turning handles (pos. 4, Fig.1).

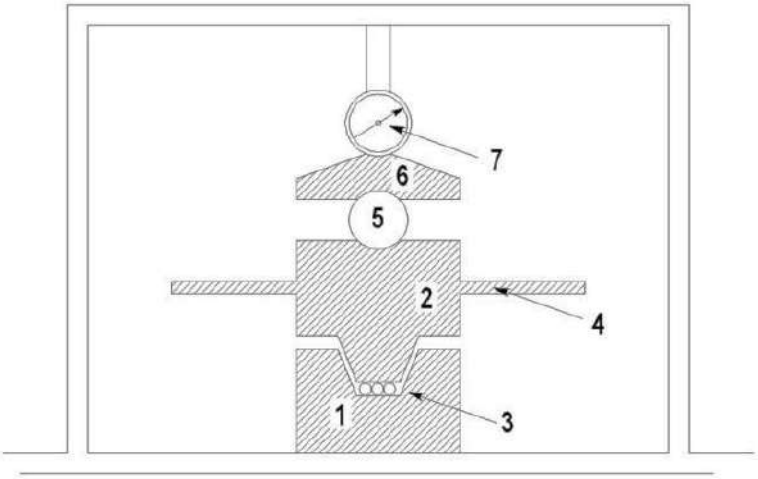

FIG.1. SCHEME OF DEVICE TO STUDY GROUNDS AT HIGH PRESSURES
1-lower holder; 2-upper holder; 3-test space of 0,75 sm^2 area;
4- handles to turn upper holder; 5-centering ball; 6-upper plate of loading device (press); 7- recorder to record load transferred to ground.

Natural clay granulometric composition was defined using laser diffraction-type analyzer «Analizette-22 MicroTec plus» under the procedure, described in [Seredin et al, 2017]. The device capabilities allow to provide diagnostics of 0,08 μm to 20000 μm size particles. In the studies of [Lepoytevin et al., 2014; Sun D et al., 2015] it was disclosed, that fine clay fraction, the sizes of which are lower, than 1 μm, defines, to a large extent, physicochemical properties of clays. That is why, on the basis of the device capabilities and significant effect of fine-dispersed particles on ground properties, we investigated the following fractions: $F_{<0,1}$, $F_{0,1-0,2}$, $F_{0,2-0,5}$, $F_{0,5-1}$, F_{1-2}, F_{2-5}, F_{5-50}.

There were carried out 319 identifications of granulometric composition of montmorillonite and 385 – of kaolinite natural clays. To evaluate changes of clay crystal lattice parameters there was provided X-ray diffraction analysis using the diffractometer «D2 Phase Bruker». The device characteristics: X-ray tube with copper anode (radiation – Cu Kα, λ=1,54060 Å), generator, voltage – 30 кW, current strength – 10 мА; linear detector – LYNXEYE; filter – Ni.

Representative sample hanging was abraded with alcohol in agate mortar to the sizes of 20-40 мсм, it was followed by its mounting in cuvette, and then diffraction pattern survey was provided. The survey conditions: divergent slot 0,2 mm, Soller's slots – primary 2,5°, secondary 2,5°; angular range 5 to 70° 2θ; impulse rate increase at each point 1,0 sec; pitch – 0,02°. The survey of oriented preparations was carried out within the interval of 4 to 35º 2θ.

The oriented preparations were produced out of clay fraction aqueous suspension by deposition on degreased slides, followed by drying at room temperature. One sample (air-dry) was surveyed, two next were additionally treated: saturation with glycerin during 24 hours, ignition in muffle furnace during 1 hour at the temperature of 600˚C.

The program «Diffrac Eva» was used for processing of curves, measurement of basal reflection width at height midpoint, as well as its area.

III. RESULTS AND DISCUSSION

The study was carried out in successive steps**.**

At the first stage investigated was effect of natural clay mineral compositions on change of ground fractional compositions, subjected to pressure.

Granulometric studies revealed, that in initial samples of montmorillonite and kaolinite natural clays, fraction content, accordingly, is as follows (mass %): $F_{<0,1}$ - 0,48 and 0,70; $F_{0,1-0,2}$ - 0,77 and 1,22; $F_{0,2-0,5}$ - 2,66 and 5,54; $F_{0,5-1}$ -8,30 and 14,8; F_{1-2} -17,73 and 30,10; F_{2-5} - 32,95 and 41,22; F_{5-50} - 37,11 and 6,42.

Change of clay fractional compositions at pressure build-up is shown in Fig. 2.

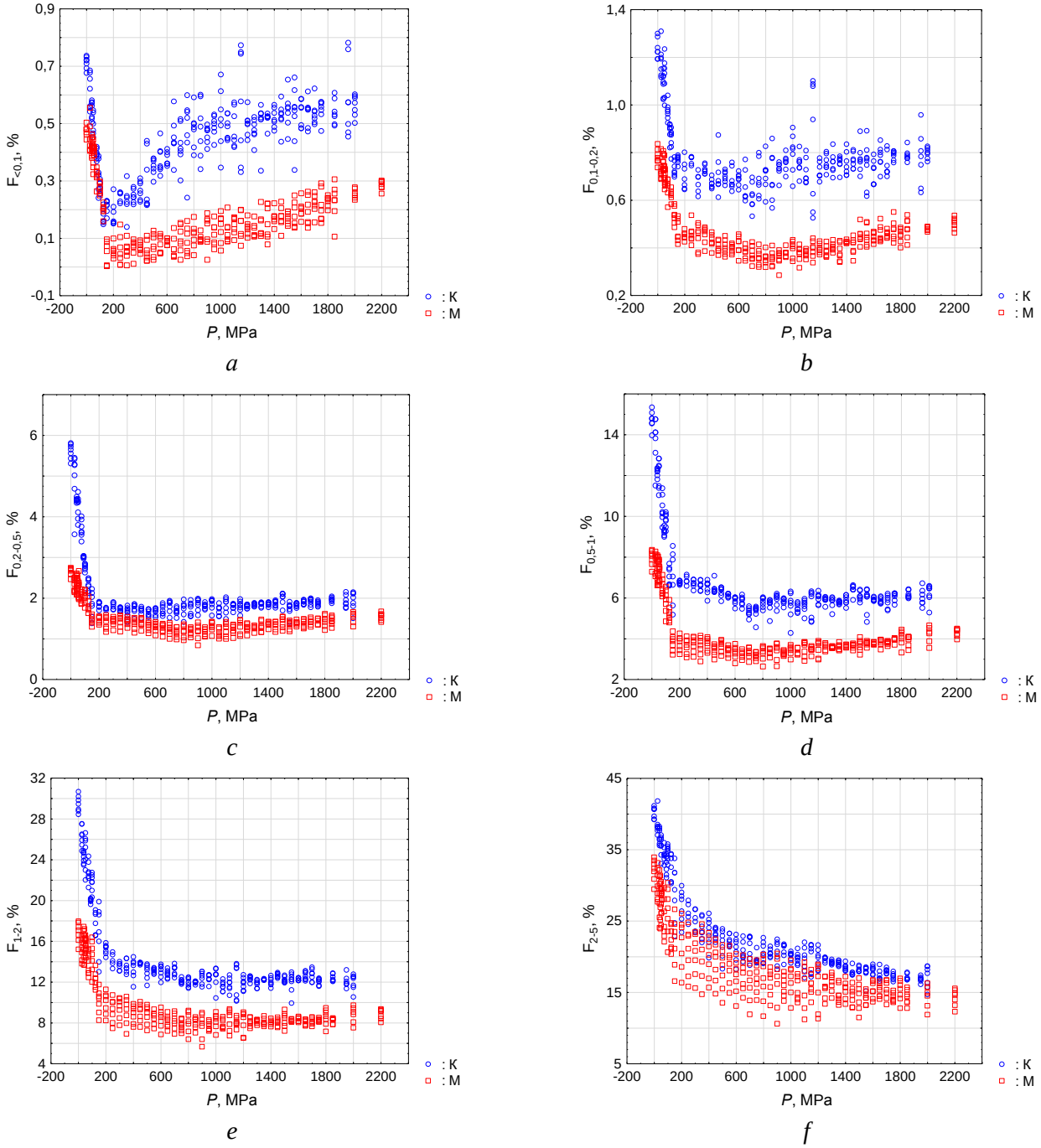

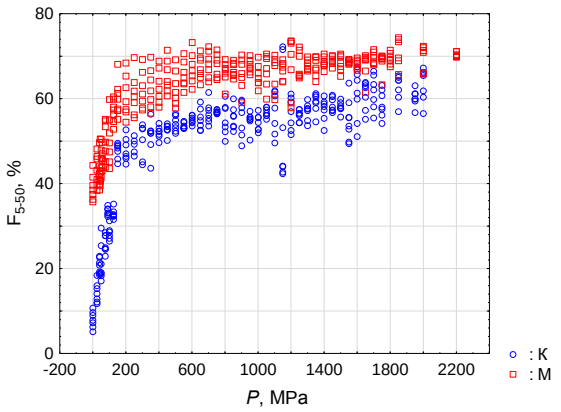

g

К – kaolin,
M – montmorillonite

FIG. 2. CHANGE OF FRACTIONAL COMPOSITION OF MONTMORILLONITE (M) AND KAOLINITE (К) OF NATURAL CLAYS UNDER PRESSURE. FRACTIONS: *a* - $F_{<0,1}$, *b* - $F_{0,1-0,2}$, *c* - $F_{0,2-0,5}$, *d* – $F_{0,5-1}$, *e* - F_{1-2}, *f* - F_{2-5}, *f* - F_{5-50}

It is evident in figure, that correlation fields have approximate behavior for different fractions. However, fraction correlation fields $F_{<0,1}$–F_{2-5} of kaolinite natural clay are positioned above applicable fields of montmorillonite natural clay, and on the contrary, for F_{5-50} fraction. The above fact reveals, that pressure effects differently formation of fractional composition of kaolinite and montmorillonite natural clays that is: mineral composition of natural clays effects significantly change of clay fraction contents in ground, when compressed.

Statistical methods [Galkin, 2013] were used to confirm the conclusion on effect of natural clay mineral compositions on formation of their granulometric composition. The matter of them is that, if mineral composition effects change of crude ground fraction contents under pressures, statistical discrepancies will be observed between samples of kaolinite and montmorillonite natural clays. Measure of discrepancy is to be evaluated as per Student's criterion (t). In case, when the calculated value (t_p) is higher, than the tabulated one ($t_т$), it is considered, that mineral composition effects change of ground fraction contents under pressures. Student's criterion constitutes $t_т$=0,03 at the degrees of freedom $\kappa=n_1+n_2-2=704$ and the significance level α=0,05. Calculated statistical parameters are exhibited in table 1.

TABLE 1
CLAY STATISTICS

Fractions, %	Kaolinite natural clay		Montmorillonite natural clay		Calculated value of Student's coefficient, t_p	Identification of samples, %		
	Mean	Stat. deviation	Mean	Stat. deviation		Kaolinite natural clay	Montmorillonite natural clay	Total
$F_{<0,1}$	0,45	0,14	0,18	0,12	25,9	80,0	85,9	83,0
$F_{0,1-0,2}$	0,79	0,15	0,47	0,12	29,2	93,4	85,0	89,1
$F_{0,2-0,5}$	2,18	0,94	1,51	0,40	11,8	42,3	83,4	63,3
$F_{0,5-1}$	6,96	2,29	4,26	1,42	17,8	83,6	83,4	83,5
F_{1-2}	14,64	4,54	9,67	2, 80	16,5	67,5	82,1	75,0
F_{2-5}	23,20	6,64	18,81	5,33	9,1	44,6	74,6	59,9
F_{5-50}	49,96	13,96	62,69	9,20	-13,5	58,4	81,8	70,4
Z	-1,76	1,02	1,68	0,98	-42,9	97,0	93,4	95,2

The table demonstrates, that calculated values of Student's coefficient for each studied fraction are higher, than $t_т$=0,03, so it can be concluded, that mineral composition effects significantly formation of crude ground fractional compositions subjected to pressure. Student's criterion reveals that samples are statistically different.

Linear discriminant analysis was used for quantitative estimation of differentiation. Calculation results of samples identification are shown in table1. The table exhibits, that maximum difference between kaolin and montmorillonite is observed for fractions $F_{0,1-0,2}$ and $F_{<0,1}$, and minimum – for fraction F_{2-5}. The rest of the fractions have intermediate position.

For them, t-criterion changes from 9,1 to 17,8, and total identification correctness – from 59,5 to 83,5%. It should be mentioned, that for prevailing majority, fractions of montmorillonite natural clay are identified better, than fractions of kaolinite natural clay.

Maximum difference of kaolinite natural clay from montmorillonite natural clay is observed as the result of complex analysis of all the fractions using step-by- step LDA. LDF expression is as follows:

$$Z = 3.32537 – 7.50608F_{0,1\text{-}0,2} + 3.15488F_{0,2\text{-}0,5} - 0.93596F_{1\text{-}2} + 0.32878F_{2\text{-}5},$$

at R = 0,86, χ = 854,3, multidimensional centers of groups Z_K = -1,76, Z_M = 1,68.

The calculations indicate that degree of sample difference of kaolinite natural clay from montmorillonite natural clay is maximum as per t-criterion (Table 1) and identification correctness, regarding both – total and each class value.

Thereby, it was found experimentally and proved statistically, that formation of micro-aggregative composition of kaolinite and montmorillonite natural clays has different scenarios, when compressed with shear. It can be explained from the position of mineral crystal lattice structures. One tetrahedral sheet and one octahedral sheet forming structural layer provide kaolin structure. They are connected between each other by hydrogen bonds, strength of which constitutes 5-40 кJ/mole [Osipov, Sokolov, 2013], that is why, kaolin crystal is featuring sufficient rigidity in common case. As to montmorillonite natural clay, structural layers consisting of two tetrahedral and one octahedral sheets are connected between each other by molecular bonds, strength of which twice and more as lower, than of hydrogen ones. Due to the abovementioned, montmorillonite crystal rigidity is lower, than that of kaolin. Therefore, processes of aggregation and dispersion progress more intensive in montmorillonite natural clays at application of vertical load and shear, compared to kaolinite natural clays. The result of this is that clay fraction content in kaolinite natural clay varies not so significantly, as in montmorillonite natural clays.

The second stage included investigation of pressure effect on general laws of natural clay micro-aggregative compositions change (revealing of classes).

Changes of natural clay fractional compositions at pressure build-up are shown in Fig 2. It is evident, that building-up of pressure to P=125 MPa leads to significant reduction of clay fraction ($F_{<5}$) contents and increase of pulverescent ($F_{5\text{-}50}$) fraction content. Content of clay fractions changes differently directed, and pulverescent one – increases under pressure build-up to P=750 MPa. Further building-up of pressure to P=2200 MPa results in increase of clay fraction contents and chaotic change of pulverescent fraction content.

Thus, with regard to qualitative feature, it can be assumed, that pressure effects formation of granulometric composition of natural clays. Two terminal pressures P=125 MPa and P=750 MPa are revealed, at which aggregation and dispersion processes have different intensity of progressing.

Linear discriminant analysis (LDA) was used to confirm the assumption on availability of terminal pressures of P=125 MPa and P=750 MPa, the main point of which is that, if boundaries between classes are acceptable, then there should be maximum identification between them (classes) [Galkin, Silaycheva, 2013]. For this purpose, all samples were divided to three classes under the "pressure" criterion. Class 1 includes the experimental data (n=61) obtained at P=0÷125 MPa inclusive, class 2 – the data (n=91) at P=150÷750 MPa inclusive and class 3 – the data (n=167) at P=800÷2200 MPa.

Two discriminant functions for each were provided for kaolinite and montmorillonite natural clays: the first one – to validate the boundary between Cl.1 and Cl. 2 ($Z_{1\text{-}2}$), the second – between Cl. 2 and Cl. 3 ($Z_{2\text{-}3}$). The natural clay fractional compositions data were used for calculations.

For kaolinite natural clay the following functions were obtained:

$$Z_{K\ 1\text{-}2} = –43,0310 – 3,0265F_{<0,1} – 1,0016F_{0,1\text{-}0,2} + 1,9803F_{0,2\text{-}0,5} + 1,5040\ F_{0,5\text{-}1} – 0,3170\ F_{1\text{-}2} + 0,2595F_{2\text{-}5} + 0,6258\ F_{5\text{-}50}$$

Multidimensional centers of classes: $Z_{Cl.1}$ = -4,54344 and $Z_{Cl.\ 2}$ = 2,79596,

R = 0,96, χ^2 =52,01.

$$Z_{K\ 2\text{-}3} = -32,4909 + 21,3266F_{<0,1} + 11,5974F_{0,1\text{-}0,2} + 9,8014F_{0,2\text{-}0,5} + 1,0194\ F_{0,5\text{-}1} – 1,7571\ F_{1\text{-}2} + 0,6667F_{2\text{-}5} – 0,0143F_{5\text{-}50}$$

Multidimensional centers of classes : $Z_{Cl\ 2}$ = -3,26488 and $Z_{Cl.3}$ = 1,8437,

R = 0,93, χ^2= 60,96.

For montmorillonite natural clay LDF are as follows:

$Z_{M\ 1\text{-}2}$ = -38,8093 – 0,7017$F_{<0,1}$ – 3,0345$F_{0,1\text{-}0,2}$ - 1,6975$F_{0,2\text{-}0,5}$ +1,7205$F_{0,5\text{-}1}$ + 2,4931$F_{1\text{-}2}$ - 0,4997$F_{2\text{-}5}$ + 0,3155 $F_{5\text{-}50}$

Multidimensional centers of classes: $Z_{Cl.1}$ = 5,17712 and $Z_{Cl.2}$ = -3,58416,

R = 0,98, χ^2 = 50,55.

$Z_{M\ 2\text{-}3}$ = 61,7964 + 41,3331$F_{<0,1}$ – 6,8428$F_{0,1\text{-}0,2}$ – 12,5794$F_{0,2\text{-}0,5}$ +2,2471$F_{0,5\text{-}1}$ – 0,2790 $F_{1\text{-}2}$ – 0,5695$F_{2\text{-}5}$ – 0,6605$F_{5\text{-}50}$

Multidimensional centers of classes: $Z_{Cl.2}$ = -2,96914 and $Z_{Cl.3}$ = 1,60828,

R = 0,91, χ^2 = 56,69.

Discriminant function calculations exhibited, that correct identification of all the samples constitutes 100%.

Thereby it is proved, that pressure terminal values P=125 MPa and P=750 MPa are well-grounded choice. That means, that each class has different intensity of aggregation and dispersion processes progressing, that is why conditions of natural clay fractional compositions formation are featuring their individual specific character as well.

The third stage concerned study of pressure effect on change of natural clay micro aggregative compositions, with regard to classes revealed *(inside classes).* Correlation analysis was provided, the essence of which is that, if observed are statistical relations ($r>r_т$, where r – pair correlation coefficient) between natural clay fractional compositions (F) and pressure (P), it is considered, that pressure effects formation of clay micro-aggregative compositions. It should be mentioned, that the tabulated value of correlation coefficient constitutes $r_т$=0,25 at α=0,05 and n=61 for class 1, $r_т$=0,20 at α=0,05 and n=91 for class 2 and $r_т$=0,17 at α=0,05 and n=167 for class 3. Let's consider correlation analysis results for each class.

Class 1 (P=0-125 MPa): mean content of clay fractions is lower, than that of initial sample (table 2). This change, probably, concerns clay particle aggregation processes, resulting in increase of pulverescent fraction $\Phi_{5\text{-}50}$ content.

TABLE 2
MAIN STATISTICAL CHARACTERISTICS OF CLAYS

Fraction	Class	Kaolinite clay					Montmorillonite clay				
		$\bar{x}$	σ	*r*	*a*	*k*	$\bar{x}$	σ	*r*	*a*	*k*
$F_{<0,1}$	Cl.1	0,44	0,18	-0,98	0,7163	-0,0043	0,37	0,09	-0,93	0,5047	-0,0023
	Cl.2	0,32	0,11	0,83	0,1013	0,0005	0,07	0,04	0,36	0,0395	0,000069
	Cl.3	0,52	0,08	0,34	0,4190	0,000074	0,17	0,06	0,77	-0,0047	0,0001
$F_{0,1\text{-}0,2}$	Cl.1	1,01	0,17	-0,95	1,2735	-0,0042	0,69	0,08	-0,87	0,8030	-0,0019
	Cl.2	0,70	0,06	-0,46	0,7638	-0,0001	0,42	0,05	-0,70	0,4976	-0,0002
	Cl. 3	0,76	0,08	0,18	0,7033	0,000041	0,42	0,05	0,81	0,2618	0,0001
$F_{0,2\text{-}0,5}$	Cl.1	3,90	1,11	-0,97	5,5854	-0,027	2,23	0,29	-0,80	2,5963	-0,0064
	Cl.2	1,74	0,14	-0,29	1,8336	-0,0002	1,36	0,15	-0,62	1,5705	-0,0005
	Cl.3	1,85	0,13	0,38	1,6461	0,0001	1,33	0,15	0,69	0,9355	0,0003
$F_{0,5\text{-}1}$	Cl.1	11,20	2,44	-0,96	14,8988	-0,0591	6,96	0,99	-0,88	8,3198	-0,0236
	Cl.2	6,27	0,67	-0,78	7,5343	-0,0028	3,53	0,36	-0,55	4,0035	-0,001
	Cl.3	5,90	0,38	0,35	5,3675	0,0004	3,67	0,34	0,75	2,7079	0,0007
$F_{1\text{-}2}$	Cl.1	23,43	3,60	-0,94	28,7528	-0,085	14,97	1,67	-0,71	16,8207	-0,0322
	Cl.2	13,66	1,44	-0,68	16,0368	-0,0052	8,87	1,11	-0,59	10,4361	-0,0035
	Cl.3	12,18	0,65	0,08	11,9696	0,0002	8,18	0,64	0,32	7,4068	0,0006
$F_{2\text{-}5}$	Cl.1	35,72	2,85	-0,86	39,5856	-0,0617	27,67	3,51	-0,73	31,6779	-0,0697
	Cl.2	23,38	3,18	-0,81	29,6140	-0,0137	19,14	3,23	-0,55	23,3908	-0,0094
	Cl.3	18,86	1,57	-0,79	23,6591	-0,0035	15,40	1,92	-0,34	17,8553	-0,0018
$F_{5\text{-}50}$	Cl.1	23,02	8,70	0,93	10,2629	0,2036	46,31	6,32	0,80	38,3612	0,1381
	Cl.2	52,57	3,69	0,81	45,3052	0,0159	64,07	4,65	0,57	57,6770	0,0142
	Cl.3	57,69	4,83	0,47	48,7852	0,0065	67,93	2,93	0,42	63,3412	0,0033

Notes: $\bar{x}$ – mean value, σ – standard deviation, r – correlation coefficient, a –free term of the equation, *k* – angular coefficient, tangent of line inclination in equation of P and F relation.

Calculations revealed that statistical relations are provided between P and F, the evidence of which is significant coefficients of pair correlation (Table 2). Availability of negative values r between P and $F_{<5}$ confirms our conclusion that, content of clay fractions is reduced, if pressure increases. Positive values r between pressure and content of pulverescent fraction, on the contrary, prove that build-up of pressure causes increase of F_{5-50} content.

To evaluate degree of pressure effect on change of investigated fraction contents, there is used index *k* – angular coefficient, which is the tangent of line inclination in equation of pressure P and F relation. It can be interpreted as follows: the higher are *k* values; more is effect of pressure on change of investigated fraction content. Calculation results are presented in Table 2 and Fig. 3.

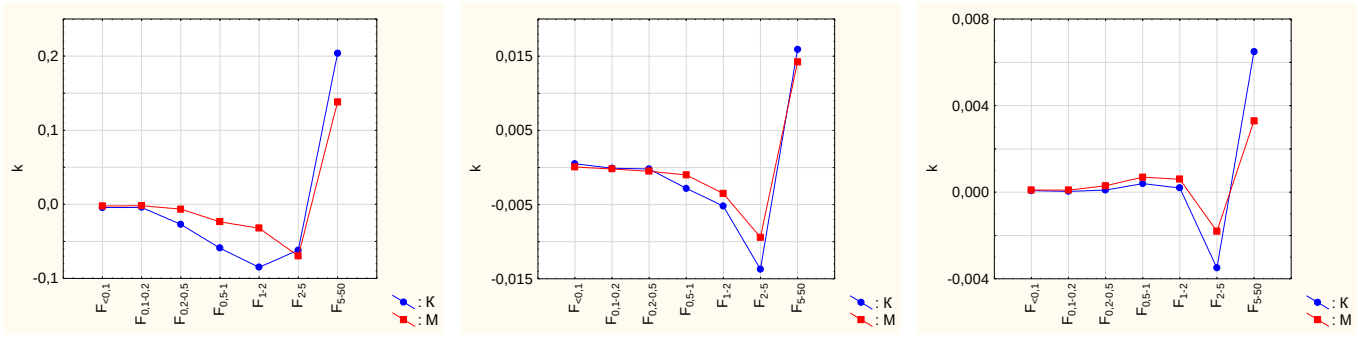

Cl.1 Cl.2 Cl.3

FIG. 3. DEPENDENCE OF PRESSURE EFFECT DEGREE ON CHANGING OF INVESTIGATED FRACTION CONTENTS FOR KAOLINITE AND MONTMORILLONITE NATURAL CLAYS REFERRING TO CLASSES 1, 2 AND 3

The figure illustrates, that less is particle size, less is effect of pressure on these fraction contents change, meanwhile, the most sensitive to pressure is pulverescent fraction F_{5-50}, and less sensitive – clay fraction $F_{<0,1}$. It should be mentioned, that fractions F_{1-2} and F_{2-5} of montmorillonite and kaolinite natural clays, accordingly, are subjected to pressure more among all the clay fractions.

Rate of clay fraction contents change at pressure increase in kaolinite natural clay is higher, compared to montmorillonite one; higher values of *k* index are evidence of the abovementioned (Fig. 3).

Class 2 (P=150÷750 MPa): similar to class 1, reduction of content of clay fraction $F_{<5}$ and increase of pulverescent fraction F_{5-50} are observed (Table 2). For fraction $F_{<0,1}$ different law is exhibited: build-up of pressure results in increase of $F_{<0,1}$ content, conditioned by dispersion processes of another fractions. Increase of F_{5-50} content is connected with aggregation processes of clay particles to the sizes of pulverescent fraction.

There are statistical relations between P and F, significant coefficients of pair correlation prove it (Table 2). Hence it appears that pressure effects significantly formation of clay fractional compositions. The largest effect pressure has on formation of fraction F_{5-50}, the least – on formation of fraction $F_{0,1-0,2}$ (Fig.3).

Among all clay fractions, the most sensitive to pressure is fraction F_{2-5}. Meanwhile, pressure effects more kaolinite natural clay, compared to montmorillonite one, higher values of *k* index are evidence of the above mentioned.

Class 3 (P=800÷2200 MPa): effect of pressure on change of clay fractional compositions is basically different from classes 1 and 2. While pressure building up, content of all the fractions, except F_{2-5} increases, confirmation of this are positive values r. There are statistical relations between P and F, significant coefficients of pair correlation are evidence of the above (Table 2). The largest effect pressure has on formation of fraction F_{5-50}, and the least – on formation of $F_{<0,1}$fraction.

Among all clay fractions, similar to foregoing classes, the most sensitive to pressure is fraction F_{2-5}. Meanwhile, pressure effects kaolinite natural clay more significant, compared to montmorillonite one, higher values of *k* index are evidence of the above mentioned.

Thus, reduction of clay fraction content and increase of pulverescent one – is the general tendency, while pressure build-up. Alongside with this law, each class shows local changes of clay fractional compositions content, subject to pressure. So, class 1 exhibits, that build–up of pressure P leads to decrease of clay fraction ($F_{<5}$) content and increase of pulverescent one. Class 2, taking into the account the abovementioned law (of class 1), demonstrates inversion only for the fraction of less, than 0,1 мсм, build-up of pressure causes increase of $F_{<0,1}$ content. Concerning class 3, formation of fractional composition is

provided based on opposite to classes 1 and 2 scenario, that is, build-up of pressure results in increase of all fractions content, and F_{2-5} fraction, on the contrary is decreased.

The fourth stage included study of conditions of natural clay microaggregative compositions formation, when compressed. Change of content of natural clay ground fractional compositions are connected with particles aggregation and dispersion processes. Aggregation of particles is effected by pressure (compression) being exhibited as physicochemical processes, causing formation of new structural relations under the attractive forces [Osipov, Sokolov, 2013; Zhu et al., 2016]. Forces of compression and shear also effect dispersion (grinding) of particles, resulting in destruction of structural relations and grinding of particles.

The following assumption is the basis of clay particles aggregation process, caused by pressure applied to ground: when clay is compressed with shear (by displacement of device upper holder relative to lower one) additional energy centers should be provided on surface of ground particles. Due to free energy, structural relations are formed between particles, causing their aggregation.

To prove the abovementioned assumption, it was required to choose evaluation criterion of clay particle surface energy state. The investigation results analysis [Shlykov, 2006; Cora et al., 2014; Zhu et al., 2016] revealed, that it is available to use as the above criterion – the size of coherent –scattering region (CSR) of X-rays in the direction of ***c*** axis (crystallographic direction). This index correlates with particles structure (micro-assemblies) and their energy activity. Small values of CSR demonstrate that micro-assemblies have small sizes and are featuring high values of cation-exchange capacity, typical for kaolin [Shlykov, 2006]. Besides, the study [Radiography.., 1983; Trofimof et al, 2005] exhibited, that in case of CSR small value, there are, as usual, water molecules between micro-assemblies, which facilitate unrestricted displacement of sub-packings relative to each other, and this, in turn, leads to increase of particles energy activity. So, coherent–scattering region, expressed as Мк index (quantity of elementary layers in defect-free blocks) can be compared with cation-exchange capacity (CEC, as index of particle energy activity). In case of Мк > 40, CEC constitutes 2-5 mg-equiv/100 g, at Мк=40-25 capacity is increased to 6-12 mg-equiv/100 g, and at Мк<25 capacity takes the value of CEC>12 mg-equiv/100 g [Shlykov, 2006].

The results of diffractometer analysis carried out by us presented in table 3, do not conflict with the investigation Shlykov`s results.

TABLE 3
RESULTS OF CLAY DIFFRACTOMETER ANALYSIS

Clay	Pressure (P), MPa	Class	Diffraction angle, 2Ɵ	Interplanar spacing (d), Å	Half-width of basal reflection, B/2	Peak area (intensity of basal reflection)	Quantity of elementary layers in defect-free blocks, Мк
Montmorillonite	initial		6,061	14,570	0,574	4,988	16,6
	0-125	1	6,230	14,173	0,631	3,054	14,7
	150-750	2	6,243	14,148	0,600	1,836	15,6
	800-2200	3	6,202	14,242	0,523	0,961	17,7
Kaolinite	initial		12,348	12,162	0,386	4,271	26,3
	0-125	1	12,324	7,176	0,435	3,153	20,7
	150-750	2	12,321	7,178	0,441	2,953	20,3
	800-2200	3	12,323	7,177	0,476	2,577	18,8

The table exhibits, that when crude grounds are compressed, crystallite surfaces defectiveness (energy capacity) of montmorillonite natural clay is higher (M=14,7-17,7), than that of kaolinite natural clay (M=18,8-26,3). Hence it follows, that particle aggregation processes are more intensive in montmorillonite natural clay, than in kaolinite one. This conclusion conforms to the experimental data of the first stage of the studies.

Let's consider conditions of clay fractional compositions formation as per classes revealed.

Class 1. Extra energy centers are formed on crystallite surfaces at pressures from 0 to 125 MPa, due to defectiveness increase (displacement of crystal lattice vacancies or relative displacements of layers). Free energy of centers enables formation of molecular attractive forces, which cause aggregation of 0,1 мсм to 5 мсм particle sizes. Due to the abovementioned, there is observed decrease of clay fraction content and increase of pulverescent one in the experiment carried out. It should be

mentioned, that if pressure range constitutes from 0 to 125 MPa, formation of extra energy centers on particle surfaces is more intense, than formation of 2 and 3 classes, numerical values of Mк index are confirmation of this.

Class 2. Defects on crystallite surfaces, probably, are «healed», at pressure build-up 125 MPa to 750 MPa in montmorillonite natural clay, that is why there is observed some increase of coherent–scattering region from Mк=14,7 – class 1 to Mк=15,6 – class 2. In kaolinite natural clays mean values of Mк practically do not change. Insignificant variation of Mк index confirms that energy potential on crystallite surfaces changes insignificantly as well. Thereby, clay particle aggregation processes are less intensive within the range of these pressures and in the first place effect change of fraction $F_{0,1-0,2}$ and F_{1-2} contents.

Reduction of clay particles, except $F_{<0,1}$ fraction, reveals, that molecular attractive forces are formed between them causing their aggregation. It is important, that based on abovementioned law, for particle sizes of less, than 0,1 мсм, build-up of pressure results in increase of their content. The indication of this is, that energy on crystallite surfaces, composing $F_{<0,1}$ fraction, is realized in the form of electrostatic repulsion forces, that can lead to process of fraction particles dispersion. Meanwhile, the second scenario version is available: dispersion of larger fractions is provided, due to which content of $F_{<0,1}$ is increased.

Class 3. Pressures of 800 MPa to 2200 MPa cause further «healing» of defects on crystallite surfaces of montmorillonite natural clay, which is conditioned by some increase of coherent-scattering region from Mк=15,6 – class 2 to Mк=17,7 – class 3. This process reduces energy on crystallite surfaces. Kaolinite natural clays are featuring opposite law: CSR index is decreased from Mк=20,3 – class 2 to Mк=18,8 – class 3. Therefore, in kaolinite clay pressures of 800 MPa to 2200 MPa cause further deteriorations of crystallite surfaces, which are realized in the form of crude ground energy potential increase. Based on the results obtained, it can be concluded, that this class of montmorillonite natural clay is characterized mainly by dispersion processes and kaolinite one, on the contrary, by aggregation processes.

Thereby, compression of natural clay on crystallite surfaces causes mainly formation of the defects, which increase crude ground energy potential. Free energy enables formation of molecular attractive forces, which result in particles aggregation. Dispersion processes, being the result of particles grinding are provided in small volumes, which is not in conflict with the data [Sergeev,1946].

IV. CONCLUSION

1. It is found experimentally, that while building-up of pressure applied to natural clay, there is general tendency of clay fraction content decrease and pulverescent fraction content increase. Montmorillonite natural clay changes are more intensive, compared to kaolinite ones.
2. It is revealed, that processes of natural clay fractional compositions change are featuring higher intensity of progressing under pressures within the range of 0–125 MPa, than under higher pressures. It is revealed, that there is different intensity of natural clay fractional compositions formation under pressures within the range of 125-750 MPa and 800-2200 MPa. Thereby, three classes are identified regarding «pressure» index, each has different intensity of aggregation and dispersion processes progressing. Due to the abovementioned, conditions of natural clay fractional compositions formation have their individual specific character as well.
3. It is disclosed, that when clay is compressed, defects are formed on crystallite surfaces, which increase energy potential of crude ground. Extra energy enables to form molecular attractive forces, which cause particles aggregation. Dispersion processes, referring to particles grinding, progress in small volumes.

REFERENCES

[1] Boiko, V.F., Verkhoturov, A.D., Ershova, T.B., Vlasova, N.M., 2009. Dependence of granulometric characteristics of dispersed nemalite on storage time. Refractories and technical ceramics 6, 47-49.

[2] Cora, I., Dódony, I., Pekker, P., 2014. Electron crystallographic study of a kaolinite single crystal. Applied Clay Science 90, 6-10.

[3] Friedlander, L.R., Glotch, T.D., Phillips, B.L., Vaughn, J.S., Michalski, J.R., 2016. Examining structural and related spectral change in marsrelevant phyllosilicates after experimental impacts between 10-40 GPA. Clays and Clay Minerals 64, №3, 89-209.

[4] Galkin, V.I., Silaycheva, V.A., 2013. Development of statistical model of permeability coefficient prediction on the basis of geological and technological indices. Petroleum engineering 9, 10-12.

[5] Ilic, B., Mitrović, A., Radonjanin, V., Malešev, M., Zdujić, M., 2016. Effect of mechanical and thermal activation on pozzolanic activity of kaolin containing mica. Applied clay science 123, 173-181.

[6] Korolyov, V. A., 2016. Modeling of granulometric composition of moon rocks. Engineering geology 5, 40–50.

[7] Krivosheeva, Z.A., Zlochevskaya, R.I., Korolyov, V.A., Sergeev, E.M., 1977. On nature of change of clay rocks composition and properties during lithogenesis. Bulletin of Moscow University 4. 60-73.

[8] Lepoitevin M., Janot J.-M., Dejardin P., Balme S., Jaber M., Guégan R., Henn F., 2014. BSA and lysozyme adsorption on homo-ionic montmorillonite: influence of the interlayer cations. Applied Clay Science 95, 396-402.

[9] Osipov, V.I., Sokolov, V.N., 2013. Clays and their properties. Composition, structure and properties formation. M.: GEOS, 576 p.

[10] Osovetsky, B.M., 1993. Fractional granulometry of alluvium. Perm: Perm university. 343 p.

[11] Radiography of main types of rock-destroying minerals (layered silicates and tectosilicates). Edited by V.A. Frank-Kamenestky. L.:Nedra, 1983. 359 p.

[12] Savko, A.D. Sviridov, V.A., 2015. Evolution of clay mineral compositions depending on conditions of their sedimentation and diagenesis. Evolution of sedimentary processes in Earth history. Materials of VIII Russian lithologic conference. pp. 293-296.

[13] Seredin, V.V., 2014. To the issue on solidity of saline clayey grounds. Engineering geology 1, 66-69.

[14] Seredin, V.V., Kachenov, V.I., Siteva O.S., Paglazova D.N., 2013. Study of laws of clay particles coagulation. Fundamental researches 10, 3189-3193.

[15] Seredin, V.V., Rastegayev, A. V., Panova, E. G., Medvedeva, N. A., 2017. Changes in physical-chemical properties of clay under compression. International Journal of Engineering and Applied Sciences V.4, 3, 18-26.

[16] Seredin, V.V., Yadzinskaya, M.R., 2014. Investigation of mechanism of particles aggregation in clay grounds when contaminated by hydrocarbons. Fundamental researches 6, 1408-1412.

[17] Sergeev, E.M., 1946 a. Compressibility of large fragmental and sand grounds. Pedology 3, 13-19.

[18] Sergeev, E.M., 1946. To the issue of pulverescent ground compression by high loads. Bulletin of Moscow University 1, 91-93.

[19] Shlykov, V.G., 2006. X-ray analysis of mineral composition of dispersed grounds. M.:GEOS, 176 p.

[20] Stefani, V.F., Conceição, R.V., Balzaretti, N.M., Carniel, L.C., 2014. Stability of lanthanum-saturated montmorillonite under high pressure and high temperature conditions. Applied Clay Science 102, 51-59.

[21] Sun, D., Zhang, L., Zhang, B., Li, J., 2015. Evaluation and prediction of the swelling pressures of GMZ bentonites saturated with saline solution. Applied Clay Science 105-106, 207-216.

[22] Trofimov, V.T., Korolyov, V.A., Voznesensky, V.A., Golodkovskaya, G.A., Vasilchuk, Yu.K., Ziangirov, R.S., 2005. Pedology, M.: MSU, 1024 p.

[23] Zhu, X., Zhu, Z., Lei, X., Yan, C., 2016. Defects in structure as the sources of the surface changes of kaolinite. Applied Clay Science 124-125, 127-136.

Analysis of Deformation Data of a Deep Foundation Pit in Karst Poor Geological Conditions

Wei-yu Wang[1], Xing-Gao[2], Qi-Zhao[3]

[1,2]Hebei Jian Ke Tang Qin Building Science and Technology Co. Ltd.
[3]College of Civil Engineering Hebei University, Baoding , Hebei, China

Abstract— *This paper is based on a deep foundation pit project under the geological conditions of karst. The monitoring data is analyzed, and the deformation rule of the foundation pit is obtained. At the same time, the influence factors of foundation pit deformation are studied, and the relationship between the displacement of slope of foundation pit at different stages is studied. Get conclusions as following, in the excavation of the foundation pit, the different supporting forms of foundation pit have great influence on the horizontal displacement of foundation pit. The horizontal displacement deformation of slope at the excavation stage is larger, accounting for 68%~78% of total deformation. The horizontal displacement deformation of slope at the backfill stage is significantly smaller, accounting for 22%~32% of the total deformation.*

Keywords— Foundation pit; deformation analysis, The foundation pit monitoring, Horizontal deformation of slope top, The vertical displacement of the slope.

I. INTRODUCTION

The deformation analysis of foundation pit is based on the phenomenon of deformation. The causes and factors of deformation are analyzed. Thorough study of deep foundation pit deformation mechanism, the foundation pit deformation is effectively controlled, and the stability of foundation pit is maintained. At present, at home and abroad, many scholars have studied the deformation of deep foundation pit. Woo[1],Ou[2],Wong[3] studied the relationship between the maximum lateral movement of support structure and excavation depth of foundation pit. Yu jianlin and gong xiaonan[4] verified the influence of space effect on deep foundation pit. Sun jianping and wei huanwei[5] showed that the horizontal displacement and subsidence ratio of slope top of foundation pit gradually tended to value over time. This paper mainly studies the effect of different supporting forms on the deformation of deep foundation pit. Meanwhile, the relationship between the displacement of slope of foundation pit at different stages is studied.

II. GENERAL SITUATION OF ENGINEERING

The length of foundation pit is 198.3m and width 87.5m. The grade of foundation pit safety is grade one. The bottom elevation of the foundation is -10m, and the excavation depth is about 11m. The east of 20m is Xueyuan Road, the south side of 5m is the hospital road, and the west side of 10m is the hospital hardening road. The south side of the foundation pit adopts the pile bolt support, and the other parts are supported by bolts. The number of monitoring points for foundation pit is 18, the horizontal displacement monitoring points and settlement monitoring points are shared. s1, s2, s3, s4, s5, s6, s7, s8, s9, s10 are bolt support, s11, s12, s13, s14, s15, s16, s17 are pile anchor support. The layout of the measuring points is shown in Figure 1.

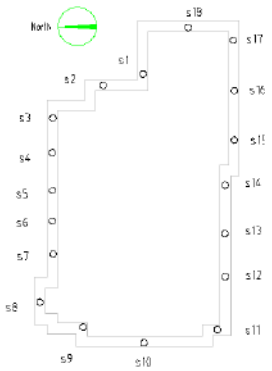

FIGURE 1. LAYOUT OF MONITORING POINTS

The lithology of the engineering field is divided into 14 layers from top to bottom, as shown in Table 1.

TABLE 1
SOIL PARAMETERS

Layer	Thickness/m	Modulus of compressibility (MPa)	Gravity density (kN/m³)	Cohesion c_k (kPa)	Internal friction angle (°)
Miscellaneous fill	0.30m～1.40m				
Silty soil	0.40～2.40m	5.18	19.3	26.4	22.8
Fine sand	0.80m～2.70m	12*	20.3*	3.0*	23.0*
Fine sand	6.70m～9.10	14*	20.6*	3.0*	26.0*
Clay	1.30m～4.50m	6.86	17.8	38.2	17.5
Fine sand	0.50m～3.40m	22*	20.0*	2.0*	28.0*
Clay	0.80m～5.20	7.18	17.9	35.4	19.8
Fine sand	0.40m～3.60m	25*	20.3*	0*	31.0*
Silty clay	2.40m～6.10	7.89	19.0	36.1	22.0
Fine sand	5.80m～8.10	26*	20.4*	2.0*	30.0*
Clay	0.40m～6.60m	7.40	18.8	62.2	23.2
Fine sand	0.40m～5.40m	28*	20.4*	0*	30.0*
Pebble	1.20m～4.70m	42*	20.2*	0*	36.0*

Note: take * as empirical value

The main unfavorable geological action of the site is karst collapse. There are carbonate rocks in the lower strata of downtown Tangshan. Carbonate is eroded by ground water to form karst caves. After the development of the karst cavity, the permeability is good, and the pipeline has a flow pattern. It has enough storage and diversion space, and can guide a large number of fine materials. An energy release zone is formed along the structural fracture zone under the action of crustal stress and earthquake dynamics. The red clay impermeable layer between the soil and the rock mass is affected. The endless supply of karstic water causes erosion of the soil on the upper part of it. Over time, "soil caves" are formed, leading to land subsidence.

III. DEFORMATION ANALYSIS

Two support methods are adopted in the supporting process of the foundation pit. The south side adopts pile bolt support mode. The other sections are supported by bolts. In the analysis of deformation data, in order to analyze the deformation of the foundation pit conveniently, two kinds of support methods are explored respectively.

3.1 Deformation Analysis of Pile Anchor Support Form

The foundation pit project is divided into two stages: foundation pit excavation and backfill stage. The excavation is a process of stress unloading, and the backfill stage is at the bottom of the loading process of stress. The stress mechanism of foundation pit in two stages is different, so two stages are considered separately

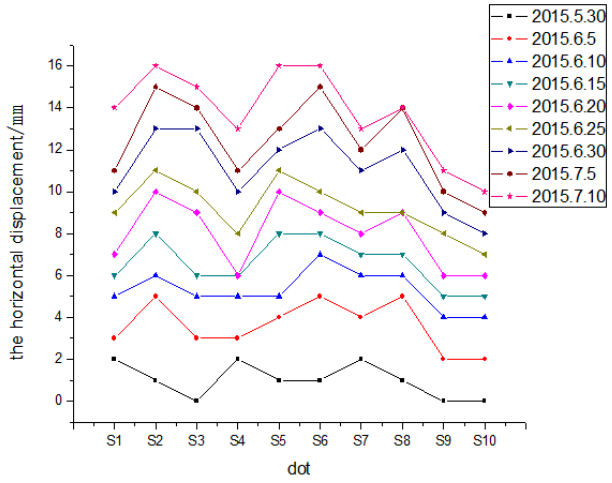

FIGURE 2. THE HORIZONTAL DISPLACEMENT OF DIFFERENT TIME S1~S10

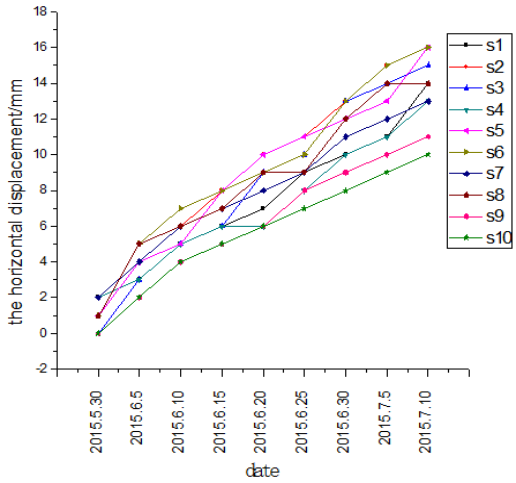

FIGURE 3. THE HORIZONTAL DISPLACEMENT CURVE OF S1~S10 CHANGES WITH TIME

Figure 2 shows that in the stage of excavation, bolt supporting monitoring points of s1~s10 under different time the amount of the horizontal displacement. Figure 3 shows that in the stage of excavation, curve of horizontal displacement of bolt supporting monitoring points of s1~s10 with time change. According to Figure 2 and Figure 3, the horizontal direction of the foundation pit excavation stage of inward migration trend is very obvious. With the increase of excavation depth, the horizontal displacement is increasing. The maximum horizontal displacement during the excavation slope is located in the middle part of the rectangular pit on the north side of S5 point and S6 point. They reach 16mm. The analysis finds that the effects caused by space, the horizontal displacement of the slope top increases and reaches the maximum. The minimum displacement point is located in the west of the pit near the southwest corner of the S10.The displacement is only 11mm.Through analysis, it is found that the monitoring point S10 is closer to the side of the pile anchor support structure, and is affected by the two supporting forms in the excavation process. The constraint of S10 point is the superposition of two supporting forms on the soil mass.

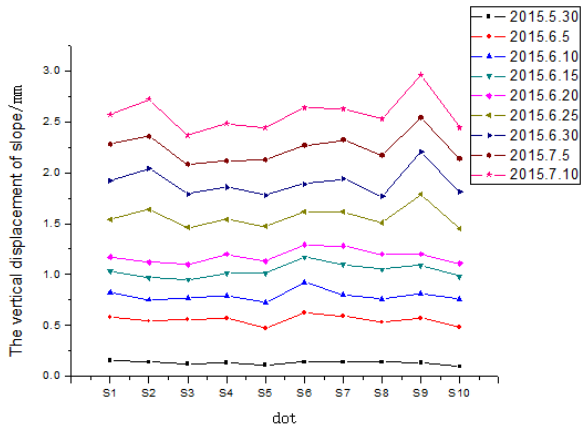

FIGURE 4. THE VERTICAL DISPLACEMENT AT DIFFERENT TIME S1~S10

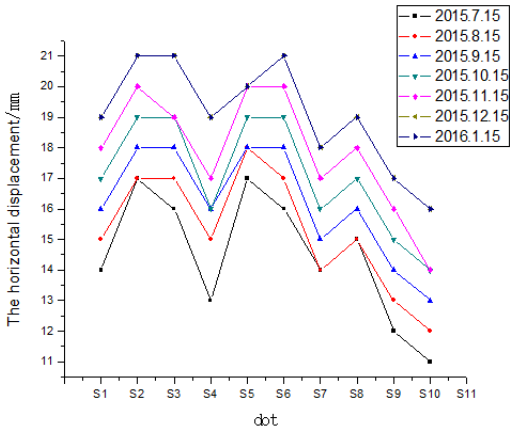

FIGURE 5. THE HORIZONTAL DISPLACEMENT OF DIFFERENT TIME S1~S10

Figure 4 shows that in the stage of excavation, bolt supporting monitoring points of s1~s10 under different time the amount of the vertical displacement. As can be seen from figure 4 the vertical displacement of foundation pit slope is increasing, the growth rate is relatively stable. The overall settlement of the enclosure structure is even. In the bolting period, the maximum vertical displacement of slope displacement is in the northwest corner location S9 and reach 3.10 mm. After analysis, the S9 point is the positive angle. In addition, in the vicinity of the S9 point, there is a 6 story building. Due to the dual role of temporary load and space function, the point of foundation pit is easy to be damaged; the vertical displacement is relatively large.

Figure 5 shows that in the stage of backfill, bolt supporting monitoring points of s1~s10 under different time the amount of the horizontal displacement. It can be seen from Figure 5 that the deformation of the retaining structure is restrained and the deformation rate is slowed down. The analysis shows that the deformation of the retaining structure is restrained after the base cushion and the floor are poured and rammed. The horizontal displacement of s1~s10 monitoring points with time the growth rate is more uniform.

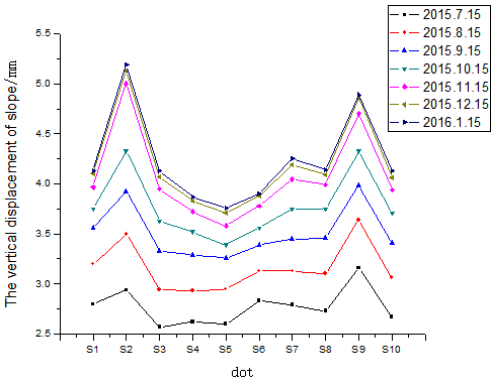

FIGURE 6. THE VERTICAL DISPLACEMENT AT DIFFERENT TIME S1~S10

Figure 6 shows that in the stage of backfill, bolt supporting monitoring points of s1~s10 under different time the amount of the vertical displacement. .As can see from figure 6, during the construction of underground and main structure, vertical

displacement of foundation pit slope is increasing. The settlement rate decreases with time, and finally tends to 0. The maximum vertical displacement of the foundation pit supported by the bolt is located at the S2 point near the northeast corner, reaching 5.19mm. There is a lot of open space near the S2 site for accumulating building material. Large displacement of vertical displacement of S2 point is caused by surcharge loading.

3.2 Deformation Analysis of pile Anchor Support Form

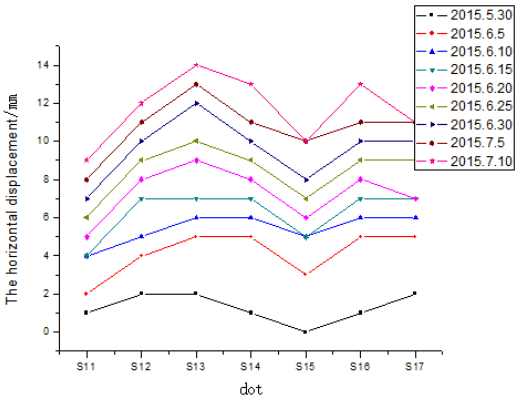

FIGURE 7. THE HORIZONTAL DISPLACEMENT OF DIFFERENT TIME S11~S17

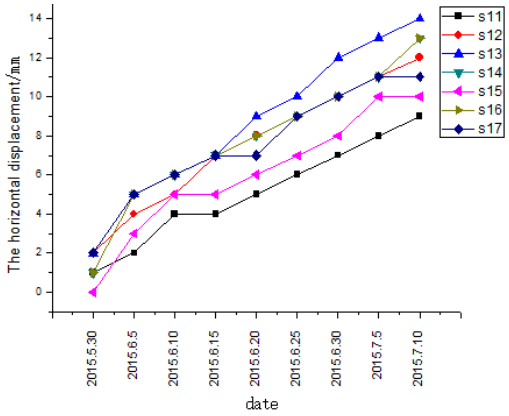

FIGURE 8. THE HORIZONTAL DISPLACEMENT CURVE OF S11~S17CHANGES WITH TIME

Figure 7 shows that in the stage of excavation, pile bolt supporting monitoring points of s11~s17 under different time the amount of the horizontal displacement. Figure 8 shows that in the stage of excavation, curve of horizontal displacement of pile bolt supporting monitoring points of s11~s17 with time change. See from figure 7 and figure 8, the horizontal displacement increases steadily with time. The maximum horizontal displacement of the foundation pit under this type of support is S13 point, reaching 14 mm. The monitoring point is located at the middle side of the south side of the foundation pit. The analysis is caused by the space action of the foundation pit. In the southwest corner, the displacement of the monitoring point S11 at the junction of the two supporting forms is the minimum, reaching 9mm. S11 point is bound by two kinds of support forms. It can inhibit the deformation of S11 point.

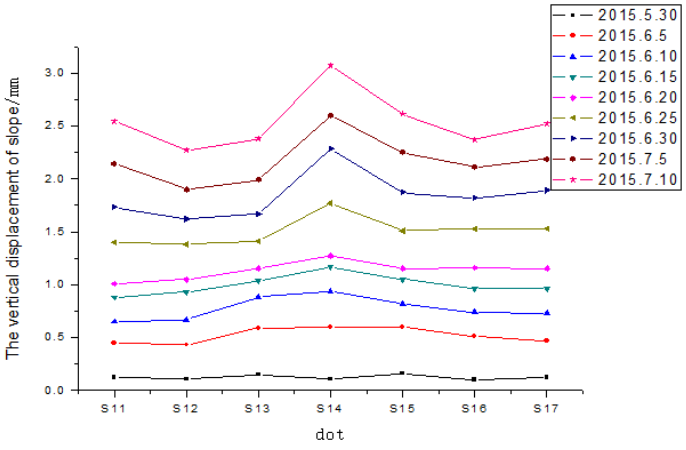

FIGURE 9. THE VERTICAL DISPLACEMENT AT DIFFERENT TIME S11~S17

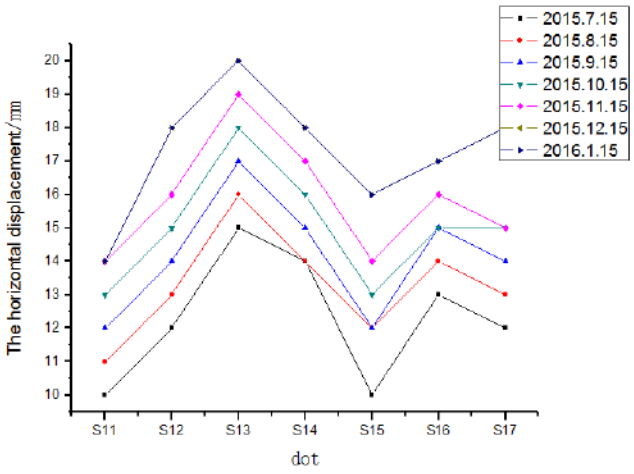

FIGURE 10. THE HORIZONTAL DISPLACEMENT OF DIFFERENT TIME S11~S17

Figure 9 shows that in the stage of excavation, pile bolt supporting monitoring points of s11~s17 under different time the amount of the vertical displacement. As can be seen from the figure 9, the accumulated value of the overall settlement is increasing. The settlement of the retaining structure is more uniform as a whole. In the stage of excavation, the maximum vertical displacement of foundation pit slope is S14, reaching 3.07mm.The S14 point is located at the middle of the long side of the south side of the foundation pit and is close to the positive angle. The S14 point is located on the south side of the foundation pit, near the street. At the same time, the S14 point is not only the middle point of the south side of the foundation pit, but also the positive angle. Because of the space effect and the force relation, this is the weakest place of the whole foundation pit.

Figure 10 shows that in the stage of backfill, pile bolt supporting monitoring points of s11~s17 under different time the amount of the horizontal displacement. As can be seen from the figure 10, the main body structure construction stage, the horizontal displacement of all monitoring points evenly along increases with the time. The horizontal deformation rate increases steadily.

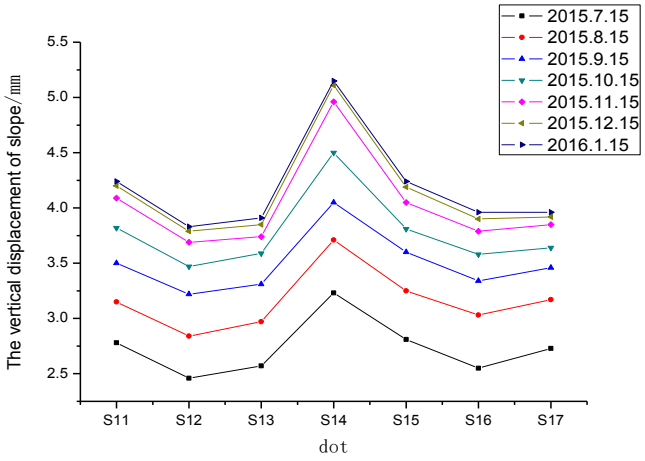

FIGURE 11. THE VERTICAL DISPLACEMENT AT DIFFERENT TIME S1~S10

Figure 11 shows that in the stage of backfill, pile bolt supporting monitoring points of s11~s17 under different time the amount of the vertical displacement. Figure 11 can be seen from the main structure of the construction stage, foundation pit deformation tends to be smooth. Monitoring points does not occur mutation. The vertical displacement of all monitoring points the growth rate gradually decreases. Deformation gradually convergences.

3.3 Comparative Analysis of Deformation between Bolt and Pile Anchor Support

TABLE 2
ANCHOR AND ANCHOR PILE SUPPORT FORM SLOPE DISPLACEMENT IN EXCAVATION STAGE

Support form	The horizontal displacement			The vertical displacement		
	Maximum displacement/ mm	Average displacement/ mm	Minimum displacement/ mm	Maximum displacement/ mm	Average displacement/ mm	Minimum displacement /mm
Bolt support	17	14.3	11	3.10	2.702	2.49
Pile anchor Support	14	12.14	10	3.19	2.673	2.40

Table 2 shows the anchor and pile anchor supporting slope top displacement at excavation stage. Can be seen from table 2, bolting slope maximum horizontal displacement at the excavation stage is s2 point. It is located near the northeast corner of the foundation. The horizontal deformation amount is 17mm. The average horizontal displacement is 14.3mm. Pile bolting slope maximum horizontal displacement at the excavation stage is s13 point, which is located near south side long edge midpoint displacement of the pit. The maximum horizontal deformation is only 14mm, and the average horizontal displacement is 12.14mm. Due to pile force control on slope deformation, resulting in the horizontal deformation of pile anchor is less than the horizontal deformation of bolt. Under the pile anchor support mode, the horizontal displacement change rate is smaller, and the change is more uniform. In the analysis of the maximum horizontal displacement of slope, the bolt support form is 3mm larger than the pile anchor support form. In the analysis of the average horizontal displacement of slope, the bolt support form is 2.16mm larger than the pile anchor support form. The effect of different supporting forms on the horizontal displacement of the excavation stage is large.

It can be seen from table 2, bolting slope maximum vertical displacement at the excavation stage is s9 point. It s located in the northwest corner. The maximum vertical deformation amount is 3.10mm. The average displacement is 2.702mm. Pile bolting slope maximum vertical displacement at the excavation stage is s14 point, which is located the south side of the foundation pit. The deformation is only 3.19mm, and the average displacement is 2.673mm. In the analysis of the maximum vertical displacement of slope, the bolt support form is 0.09mm larger than the pile anchor support form. In the analysis of the average vertical displacement of slope, the bolt support form is 0.029mm larger than the pile anchor support form. The effect of different supporting forms on the vertical displacement of the excavation stage is small.

TABLE 3
ANCHOR AND ANCHOR PILE SUPPORT FORM SLOPE DISPLACEMENT IN BACKFILL STAGE

Support form	The horizontal displacement			The vertical displacement		
	Maximum displacement/ mm	Average displacement/ mm	Minimum displacement/ mm	Maximum displacement/ mm	Average displacement/ mm	Minimum displacement/ mm
Bolt support	17	14.3	11	3.10	2.702	2.49
Pile anchor support	14	12.14	10	3.19	2.673	2.40

Table 3 shows the anchor and pile anchor pile supporting form slope displacement in backfill stage. Can be seen from table 3, bolting slope maximum horizontal displacement at the backfill stage is s9 point. It s located in the northwest corner. The horizontal deformation amount is 6mm. The average horizontal displacement is 4.8mm. The maximum horizontal displacement of pile anchor supporting the top level is 6mm, and the average horizontal displacement is 5.18mm. In the analysis of the maximum horizontal displacement of slope, two kinds of supporting forms are the same. In the analysis of the average horizontal displacement of slope, the bolt support form is 0.34mm smaller than the pile anchor support form. The effect of different supporting forms on the horizontal displacement of the backfill stage is small.

Can be seen from table 2, the maximum vertical displacement of pile anchor supporting is S2, which is located near the northeast corner of the foundation pit. The maximum vertical deformation amount is 2.34mm. The average displacement is 1.537mm. The maximum vertical displacement of pile anchor supporting is S14, which is located the south side of the foundation pit. The deformation is only 1.96mm, and the average displacement is 1.51mm. In the analysis of the maximum vertical displacement of slope, the bolt support form is 0.803mm larger than the pile anchor support form. In the analysis of the average vertical displacement of slope, the bolt support form is 0.027mm larger than the pile anchor support form. The monitoring points of bolting slope of the maximum vertical displacement are S2 point. S2 point settlement is caused by the piling up of building materials, and the support structure has nothing to do with it. The effect of different supporting forms on the horizontal displacement of the backfill stage is small.

IV. RELATIONSHIP BETWEEN FOUNDATION PIT DEFORMATION AT EXCAVATION STAGE AND BACKFILL STAGE

TABLE 4
THE HORIZONTAL DISPLACEMENT OF THE EXCAVATION STAGE AND FILLING STAGE OF PROPORTION

dot	s1	s2	s3	s4	s5	s6	s7	s8	s9
Accumulative value of excavation stage/mm	14	17	16	13	16	16	14	15	11
Accumulated value during backfill stage/mm	5	4	5	6	4	5	4	4	6
Total displacement/mm	19	21	21	19	20	21	18	19	17
Proportion of displacement at excavation stage	73.68%	80.95%	76.19%	68.42%	80%	76.19%	77.77%	78.95%	64.71%
Proportion of displacement in backfill stage	26.32%	19.05%	23.81%	31.58%	20%	23.81%	22.23%	21.05%	35.29%
dot	**s11**	**s12**	**s13**	**s14**	**s15**	**s16**	**s17**	**s18**	**AVG.**
Accumulative value of excavation stage/mm	10	12	14	14	10	13	12	12	13.33
Accumulated value during backfill stage/mm	4	6	6	4	6	4	6	5	4.94
Total displacement/mm	14	18	20	18	16	17	18	17	18.27
Proportion of displacement at excavation stage	71.43%	66.67%	70%	77.78%	62.5%	76.47%	66.67%	70.59%	72.65%
Proportion of displacement in backfill stage	28.57%	33.33%	30%	22.22%	37.5%	23.53%	33.34%	29.41%	27.35%

Table 4 shows the proportion of the horizontal displacement at different stages. It can be seen from table 4, the horizontal displacement deformation at excavation stage is large, about the total amount of deformation 68%~78%. The horizontal displacement deformation at backfill stage is large was significantly smaller, about the total amount of deformation 22%~32%.

TABLE 5
THE VERTICAL DISPLACEMENT OF THE EXCAVATION STAGE AND FILLING STAGE OF PROPORTION

dot	s1	s2	s3	s4	s5	s6	s7	s8	s9
Accumulative value of excavation stage/mm	2.74	2.85	2.49	2.58	2.54	2.75	2.73	2.66	3.10
Accumulated value during backfill stage/mm	1.39	2.34	1.64	1.29	1.22	1.15	1.52	1.48	1.79
Total displacement/mm	4.13	5.19	4.13	3.87	3.76	3.90	4.25	4.14	4.89
Proportion of displacement at excavation stage	66.34%	54.91%	60.29%	66.67%	67.55%	70.51%	64.24%	64.25%	63.39%
Proportion of displacement in backfill stage	33.66%	45.09%	39.71%	33.33%	32.45%	29.49%	35.76%	35.75%	36.61%
dot	s11	s12	s13	s14	s15	s16	s17	s18	AVG
Accumulative value of excavation stage/mm	2.70	2.40	2.52	3.19	2.76	2.49	2.65	2.51	2.68
Accumulated value during backfill stage/mm	1.54	1.43	1.39	1.96	1.48	1.47	1.31	1.38	1.52
Total displacement/mm	4.24	3.83	3.91	5.15	4.24	3.96	3.96	3.89	4.20
Proportion of displacement at excavation stage	63.68%	62.67%	64.45%	61.94%	65.09%	62.87%	66.91%	64.52%	63.84%
Proportion of displacement in backfill stage	36.32%	37.33%	35.55%	38.06%	34.91%	37.13%	33.09%	35.48%	36.16%

Table 5 shows the proportion of the vertical displacement at different stages. It can be seen from table 5, the vertical displacement deformation at excavation stage is large, about the total amount of deformation 61%~67%. The vertical displacement deformation at backfill stage is significantly smaller, about the total amount of deformation 33%~39%.

V. CONCLUSION

1 In the foundation pit project, the horizontal displacement and settlement of slope changes over time gradually increasing.

2 In the excavation stage, different supporting forms have great influence on the horizontal displacement of foundation pit slope. The effect of different supporting forms on the vertical displacement of the excavation stage is small.

3 The horizontal displacement of the excavation stage accounted for about 68%~78% of total displacement, the vertical displacement of slope deformation accounted for about 61%~67%.

4 Two different kinds of support form have very little effect on the vertical displacement and horizontal displacement of foundation pit slope.

5 In the backfill stage, horizontal displacement is smaller, accounting for about 22%~32% of total displacement. The vertical displacement of slope deformation is smaller, about the total amount of deformation 33%~39%.

REFERENCES

[1] Woo S M, Moh Z C. Geotechnical characteristics of soils in Taipei basin. In: Proceedings of the 10^{th} South Asian Geotechnical Conference, Special TaiwanSession, Taipei, 1990(2): 51-65

[2] Ou C Y, Hsieh P G Chiou D C. Characteristics of ground surface settlement during excavation. Canadian Geotechnical Journal, 1993, 30: 758-767

[3] Wong I H, Poh T Y, Chuah H L. Performance of excavations for depressed express way in Singapore. Journal of Geotechnical and Geoenvironmental Engineering, ASCE, 1997, 123(7): 617-625

[4] Jianli Yu, Xiaonan Gong. Study on Deformation Properties of Poundation Pit Engineering[J]. China Civil Engineering Journal,2002,04:86-90.(In Chinese)

[5] Huanwei Wei, Fengbo Song, Min Yang, Jianping Sun. Simplified Calculation Method for Deformation of Composite Soil Nailing Wall[J]. Engineering Mechanics,2011,S1:156-161+166.(In Chinese).

Experimental of surface roughness and tool wear on coolant condition technique using Aluminium alloy 319 used in automotive industries

S. Zainal Ariffin[1*], M. Alias[2], AR Yusof[3], MM Rahman[4]

[1,2]Faculty of Manufacturing Engineering Technology, TATI University College, Kemaman, Terengganu, Malaysia
[3]Faculty of Manufacturing Engineering, University Malaysia Pahang, Gambang, Kuantan, Pahang, Malaysia
[4]Faculty of Mechanical Engineering, University Malaysia Pahang, Gambang, Kuantan, Pahang, Malaysia

Abstract**—** *The present day the applications of machining part tolerances, like the automotive industries aimed to reduce the fuel consumption of their vehicle by reducing the total mass per vehicle and the method process for machining. Understanding of the interaction and significance machining parameters are important to improve the efficiency of any machining process and the accuracy part produced. The objective of this research is to analyze the machining parameters (spindle speed, depth of cut and feed rates) in a three machining conditions (dry, wet and 1.0 mm coolant nozzle size on the surface roughness and tool wear using Respond Surface Method (RSM) on the CNC Lathe machine with 2 axes movements. The synthetic soluble oils, and coated cemented carbide Al2 O3 insert were used as a workpiece material and cutting tool respectively. The result of the machining experiment for Aluminum alloy 319 was investigated to analyze the main factor affecting surface roughness using the analysis of Variance (ANOVA) method. The optimum selection of the cutting conditions effectively contributes to the increase in the productivity and reduction in the production cost; therefore almost attention is paid to this problem. In cutting process, optimization of cutting parameters is considered to be a vital tool for improvement in output quality of a product as well as reducing the overall production time. The acquired results showed that the coated cemented carbide Al_2O_3 insert gives the optimum overall performance in terms of surface roughness and tool wear with the smallest orifice size coolant. The research also beneficial in minimizing the costs incurred and improving productivity of manufacturing firms using the mathematical model and equations, generated by CCD based on RSM method.*

Keywords**— Turning, infrared, cutting temperature, coated carbide tool, Response Surface Method.**

I. INTRODUCTION

In metal cutting industries, machining types, especially turning operation is very basic type of machining [1]. Traditionally, the selection of cutting conditions for machining was left to the manufacturing engineer, machine operator or machine setup technician is often expected to utilize experience and published shop guidelines for determining the proper machining parameters to achieve a specified level of requirement condition like surface roughness. In such cases, the experience of the operator plays a major role, but even for a skilled operator has a problem to obtain the optimum values each time[2] [3]. Usually machining parameters used in metal cutting are cutting speed, feed rate, depth of cut and condition of coolant. The setting of these parameters determines the quality characteristics of machined parts. Application of with combination machining condition parameter using new approach of designing a 1.0 mm size nozzle is highlighted as one of the more important areas of research due to the move toward high removal rates and higher quality. Most of CNC Turning machine equipped with soluble oil which is a type of flood coolant. A review of nozzle designs presently available and an analysis of the suitability of each for different applications is presented. The objectives of this project are to evaluate the effects of the surface roughness of a three machine condition (design sizes nozzle 1.0 mm, dry, wet coolant) using coated carbide tool when machining Aluminium alloy 319. This research applies RSM method approach to studying the impact of turning parameters on the roughness of turning surfaces. RSM analysis method approach is quality control methodology that combines control charts and process control with product and process design to achieve a robust total design [4].

Aluminum alloy 319 has become a preferred materials for the automotive components because of its lightweight and good mechanical properties, hence offers the better strength-to-weight ratio material to these industries [5]. It is widely used for structural application such as cylinder head component. This is account on its excellent casting characteristics and good mechanical properties. Aluminum alloy 319 is a precipitation hardening Aluminium alloy 319, containing magnesium and silicon as its major alloying elements. It has good mechanical properties and exhibits good weld ability. It is one of the most common alloys of aluminum for general purpose use. The mechanical properties of Aluminum alloy 319 depend greatly on the temperature, or heat treatment, of the material. Aluminum alloy 319 is widely used for construction of aircraft structures,

such as wings and fuselages, more commonly in homebuilt aircraft than commercial or military aircraft. It is also used for yacht construction, including small utility boats [3]. Others than that it is also used in automotive parts, such as wheel spacers and used in the manufacture of aluminum cans for the packaging of foodstuffs and beverages [6].

Most of the researches are focused on the cutting speed, feed rate, depth of cut, during the cutting tool process. In this research, there is an investigation on the technique coolant influence of available three machine condition (sizes nozzle 1.0 mm, dry, wet (flood cooling) over the range of turning operation parameter on Aluminum alloy 319. The effectiveness of the three machine condition (sizes nozzle 1.0 mm, dry, wet coolant) systems is evaluated of surface roughness (microstructure and micro hardness). Although manufacturing techniques have become more sophisticated, many processes and tool designs are still based on experience and intuition. Advances in computer and material sciences have greatly enhanced the ability to develop predictive capability and to achieve the goal of optimization for a wide variety of applications. These techniques have resulted in reduction in friction and heat at the cutting zone, hence improved productivity of the process.

1.1 History of Recent Machining Optimization coolant condition techniques in metal cutting process

Over the past century, Besides, [7]in the article Investigation of Cryogenic Cooling By Liquid Nitrogen in the Orthogonal Machining Process believed that cryogenic cooling is able to cut down the cutting temperature which strengthen the chip tool interaction, preserve the cutting edge and has a better dimensional accuracy than dry and wet machining. The article "Hydrogen gas generation in the wet cutting of aluminium and its alloys." stated that the wet cutting of aluminum and alloys by the generation of hydrogen gas is because of the chemical reaction between the fresh surface of aluminum and water. Finally, the article "The effect of applying high-pressure coolant (HPC) jet in Machining of 42crmo4 steel by uncoated carbide inserts" by [6], opined out that Supply of high-pressure coolant (HPC) on high velocity might give an excellent control to decrease the cutting temperature and tool wear besides increasing the tool life.

Workpiece material is very important in choosing tools, machining parameters and cooling strategy. According to [8], is quantified by various parameters, such as, tool life, chip size, achievable surface finish and/or the amount of specific power consumed. It is influenced by a material's alloy chemistry, additives, microstructure, heat treatment, temper and physical and mechanical properties [9]. In addition, different workpiece materials have different degrees of sustainability for near dry and dry machining. There are various workpiece materials to enhance machinability. In addition, according to [10], lead acts as a lubricant, thus reducing the friction coefficient of friction between the chip and the tool. It also creates discontinuities in the atomic structure, which promotes chip fragmentation, reduce cutting forces and also reduce tool wear. However, lead has caused recent environmental concern, which has made metal manufacturers looking for alternative additives.

Minimum Quantity Lubrication (MQL), which is also known as near dry machining, is an alternative to traditional flood coolant. It is also known as dry machining that applies a small amount of oil, commonly 10-50 mL/hr [11]. MQL is a useful, environmentally-friendly alternative to flood cooling when dry machining is not practicable [12]. It can be applied to all machining operations. Furthermore, studies have shown that MQL is effective at reducing temperature , material adhesion [11], tool wear and thermal distortion, when compared to dry machining. A study by [9] showed that near-dry machining is implementation-ready for drilling, milling, reaming and tapping, with that production rate and also quality were equal to wet machining. Technique of temperature measurement includes: (1) thermocouple – artificial and natural thermocouple, (2) infra- red photography, (3) Optimal infrared pyrometer, (4) thermal paints, (5) Metallurgical change in work piece/cutting tool material, (6) Thermal Camera technique. Several detailed review is available in literature for these techniques of temperature measurement. Every method has its own pros and cons depending upon physically arrangements developed in an analytical prediction model for the measurement of cutting temperature. They came with conclusion that cutting temperature is a function of cutting speed and feed rate with following equation:

$$8_t = V^{0.5} f^0 \quad (1)$$

where 8_t is the average cutting temperature, V is the cutting speed and f is feed rate.

In this study of temperature measurement, the most widely used infrared thermometer laser was selected for the measuring of cutting tool's average temperature during turning operation. The values within certain range of cutting parameters like cutting speed, depth of cut and feed rate were selected and used for building the mathematical model using CCD based Response Surface Method (RSM). The temperature data of cutting tool was obtained by experimentation and the optimization of selected cutting parameters obtained successfully.

II. EXPERIMENTATION WORKS

Experiment were conducted on CNC PUMA 250 Daewoo to study the technique cooling condition used in this research that will bring for better cutting performance like cutting temperature. The experimental setup is shown in Fig.1. Furthermore, the range of the operating parameters for experimentation has also been discussed

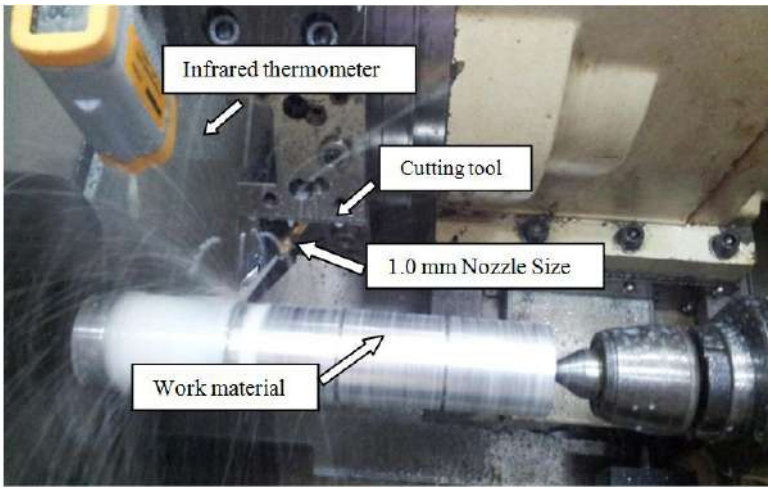

FIG.1. THE EXPERIMENTAL SETUP

This machine is equipped with a pump system, whereby the flow rate from this pump is kept constant throughout the experiment. The tool holder remains the same with coolant technique cooling condition used. The workpiece is mounted on the jaw in to spindle in order to ensure that workpiece is fixed in its position during machining.

Fig. 2. shows the experiment setting, equipment, and workplace. Surface roughness (Ra) was measured with a Mitutoyo Surftest S-J-301 portable surface roughness tester. The average value of surface roughness was used in the analysis. Surface roughness (Ra) = 6.0μm. For tool wear, the average value of surface roughness was used in the analysis. For tool wear, the most commonly used criteria for the straight cut is flank wear, which was measure by SEM TM3030 plus Tabletop Microscope -Hitachi. The tool life criteria were set at maximum flank wear width of 0.3 mm or failure

FIG. 2. EXPERIMENT EQUIPMENT, WORKPLACE, DESIGN OF 1.0 mm SIZE NOZZLE ORIFICE AND ANALYSIS SETTING

2.1 Material and Methods

The workpiece material used for this investigation is Aluminum alloy 319 with an axial length of 250 mm and the Ø 60 mm. The physical characteristics of the material are present Table 1. The cutting tool used for this study, Cemented Coated Carbide, is designated as ISO VCGT 160404. The turning process was performed in an environment coolant condition technique, (1.0 mm nozzle size, Wet and dry)

TABLE 1
PHYSICAL DATA OF ALUMINUM ALLOY 319

Physical Data	Value
Density	2.79 g/cm^3
Melting Point	2.79 g/cm^3
Modulus of Elasticity Tension	10
Modulus of Elasticity Torsion	3.8

RSM is a dynamic, important tool of the design of experiment (DOE) and is based on fitting empirical models with experimental data. These data are obtained from the relationship between response and input decision variable to maximize or minimize response properties. RSM is a set of statistical technique that employ linear or square polynomial function to describe and explore experimental conditions of a study system until its optimization. This method is useful for any field of engineering [6, 13].

2.2 Experiment Conditions

The turning process was performed in an environment condition cutting fluids. Since wet (flood cooling), dry cutting and 1.0 mm orifice nozzle sizes internal diameter following the experiment condition as shown in Table 2. The Central Composite Design (CCD) based RSM was used for the determination of optimum control factors 3- level factor design with center point six was selected. Values of those factors had been achieved with consideration of the machine tool capacity. There were total 30 combinations of the turning runs were carried out using design expert software to complete experimentation.

TABLE 2
EXPERIMENT CONDITIONS AND THEIR LEVELS STANDARD CUTTING CONDITIONS

Experimental conditions		
WORKPIECSE	Material Shape Diameter Length	Aluminum alloy 319 Cylindrical rod with axial or Round 60 mm 350 mm
TOOL	Material Insert type Holder Type	Al_2O_3-coated cemented carbide VCGT 160404 TH K10 SVJCL - 2525M16
CUTTING DATA	Operation Cutting Speed Feed rate Depth of cut	Turning 150 – 270 m/min 0.08 – 0.24 mm/rev 0.2 – 1.0 mm
CUTTING ENVIROMENT	Coolant Research Method	Synthetic soluble oil Various parameter of coolant (1.0 mm orifice nozzle sizes , Dry, Wet Coolant
RESPONSES	Cutting Environments	Surface Roughness, Temperature and tool wear

III. RESULT AND DISCUSSION

The observation made during the 30 run experiment. Table 3 implies the effect of surface roughness on individual cutting parameters. The change in depth of cut has very high effect on surface roughness while cutting speed and feed rate have moderate effect on surface roughness. For the given range of cutting parameters, feed rate has been found as the most significant parameter. Figure 3, which was generated by software, shows the correlation between feed rate and surface roughness with points indicates that the significance rate between feed rate and surface roughness is 0.7667 Central Composite Design based RSM was selected in this work [22]. RSM requires more data compare to the Taguchi method to ensure the optimum condition [23, 24]. RSM relates the independent input variables with output (process response). Design Expert software was used and obtain the set of experimental runs of CCD which would help to investigate the influence of three cutting parameters (cutting speed, depth of cut and feed rate) on the output (surface roughness and temperature). Show in table 4, the CCD with its output as a surface roughness and temperature. Again this data had been utilized to analyze through Design-Expert Software. The result of Analysis of Variance (ANOVA) has been carried out and as per Table 3 and 4 the value of R-squared (0.8352) and predicted R-squared (0.6814) were obtained

TABLE 3
VALUE OF R-SQUARED AND ADJUSTED R-SQUARED

Std. Dev	0.25	**R-Squared**	0.8352
Mean	1.47	**Adj R-Squared**	0.6814
C.V	17.14	**Pred R-Squared**	0.3094
PRESS	3.98	**Adeq Precision**	7.317

TABLE 4
ANOVA AND R-SQUARED TABLE FOR AVERAGE SURFACE ROUGHNESS (Ra)

Source	Sum of Squares	DF	Mean Square	F Value	Value Prob > F	significant
Model	924.15	14	66.01	3.52	0.0106	significant
Residual	281.22	15	18.75			
Lack of Fit	217.72	10	21.77	1.71	0.2870	not significant
Pure Error	63.50	5	12.70			
Cor Total	1205.37	29				

FROM THIS ANOVA RESULT THERE WAS ALSO RELATIONSHIP OBTAINED IN FORM OF EQUATION AS SHOWN IN EQUATION 1 WHICH RELATES THE INPUT AND OUTPUT PARAMETERS AFTER BACKWARD ELIMINATION INSIGNIFICANT MODEL TERMS FROM IT. FOLLOWING IS THE FINAL EQUATION IN TERMS OF CODED FACTORS.

Temperature = + 62.9466 + 0.41185 ± 4.66598 + 0.50203 - 8.56037e004 + 1002.85416 + 5.21418 + 1.687771 - 0.13021 + 0.041667 + 1.6667E-003 + 11.71875 - 35.93750 - 4.29080

Fig 3 shows the main effect plots for surface roughness, which had the most significant influence of feed rate on surface roughness in the dry turning process. The slot of Ra line verses feed rate showed that Ra value substantially increased when feed rate increased from 0.08 mm/rev to 0.24 mm/rev (Figure 3b). Surface roughness did not change significantly when change speed from 150 - 270 m/min (Figure 3a). The Ra value was slightly influenced by cutting speed, followed by depth of cut. Therefore, feed rate is a significant factor that influences the value of surface roughness, similar to [40], feed rate is the main parameter that influences the turning of Aluminum alloy 319.

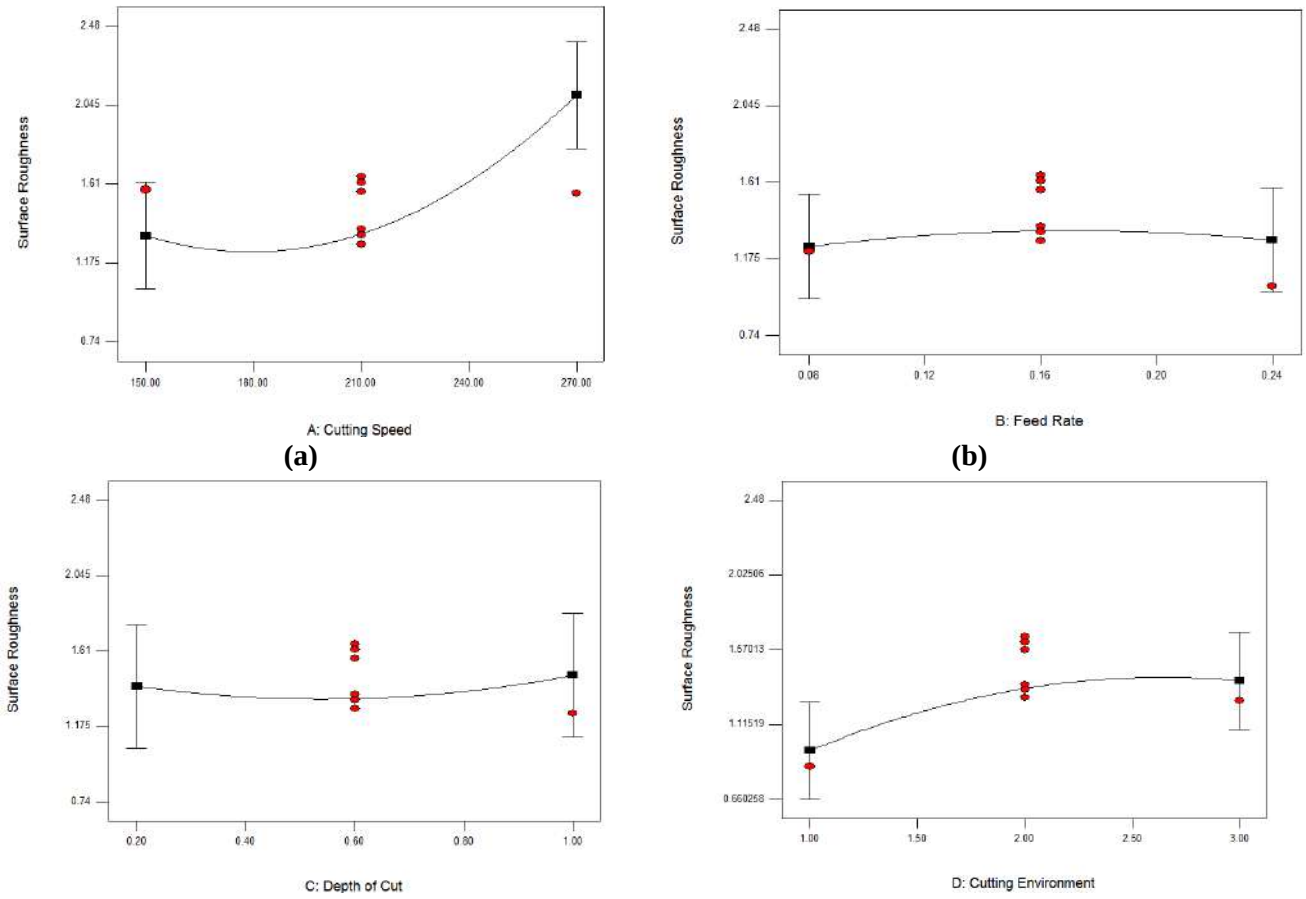

FIG. 3: MAIN PLOTS OF SURFACE ROUGHNESS (RA) VERSUS (A) CUTTING SPEED (B) FEED RATE (C) DEPTH OF CUT (D) CUTTING INVEROMENT

THE 3D SURFACE PLOT BETWEEN FEED RATE AND DEPTH OF CUT IS PRESENTED IN FIG 4. SURFACE ROUGHNESS WAS MINIMIZED WHEN FEED RATE AND DEPTH OF CUT WARE AT LOWEST LEVELS. A SIGNIFICANT MUTUAL INTERACTION OCCURED BETWEEN CUTTING SPEED , FEED RATE, AND DEPTH OF CUT WITH CUTTING INVIROMENTAL. THE OPTIMAL DEREASE IN SURFACE ROUGHNESS WAS FROM 0.56 (µM) TO 2.45 (µM), WHERE FEED RATE WAS WITHIN THE RANGE OF 0.08 - 0.24 MM/REV, DEPTH OF CUT IN THE RANGE OF 0.8 - 1.0 MM, AND CUTTING SPEED IN THE RANGE OF 110 -270 M/MIN. THESE FINDINGS WERE REPORTED BY HANAFI ET AL. (2012) AND CAMPOSECO -NEGRETE (2013).

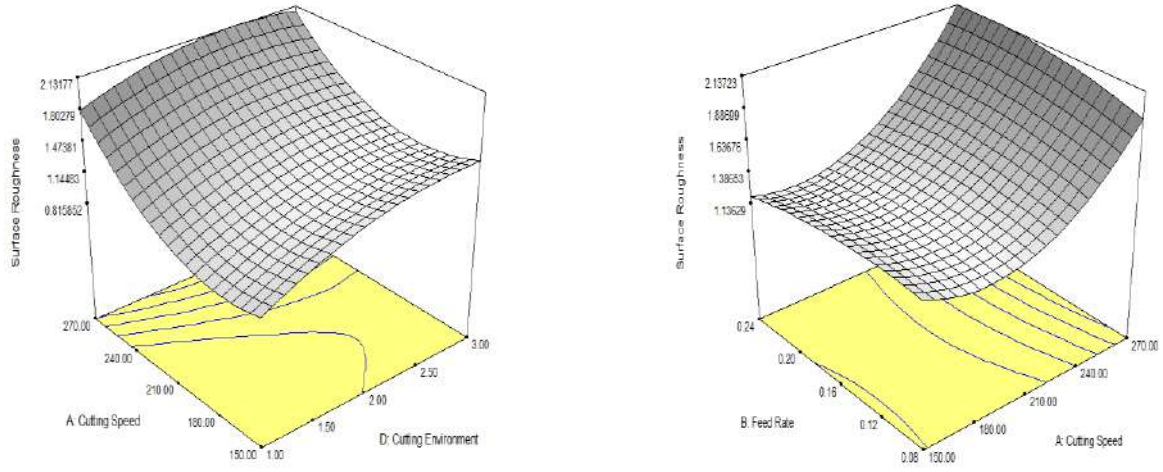

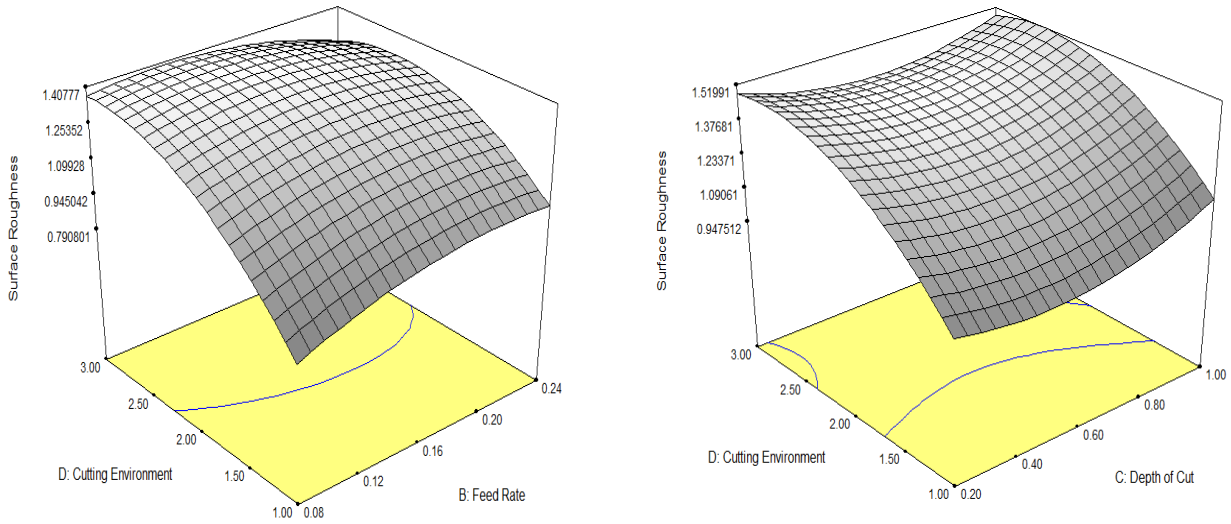

(c) **(d)**

FIG. 4: MAIN AND 3D SURFACE PLOTS OF SURFACE ROUGHNESS (RA) (A) EFFECT OF CUTTING SPEED AND CUTTING ENVIROMENT (B) FEED RATE OF AND CUTTING SPEED (C) EFFECT OF CUTTING ENVISOMENTAL AND FEED RATE (D) EFFECT OF CUTTING ENVIROMENT AND DEPTH OF CUT

3.1 Surface Roughness

Severe deterioration in the machined Surface roughness was observed at flank wear of approximately 0.30 mm. A phenomena similar to the coolant technique effect (1.0 mm nozzle size, wet and dry) in machining of hardened steel occurred gradually on the part surface when turning with a worn insert. 25 x 25 mm metallographic sample were extracted from the surfaces obtained with both sharp and worn inserts and then analyzed obtained using SEM. The result is present in Fig. 5. As illustrated, it can be see that the cutting coolant technique with machining parameter was a factor in the occurrence of the described phenomena. As the cutting increases, higher cutting temperature is generated in the tool workpiece interface, which increases the volume of materials adherence to the machined surface and cutting edge. Upon completion of the experiment tests, all work pieces were examined for the burr formation. Based on SEM examination of the parts, it can be concluded that the severity of the burr formation is a direct function of the method of coolant technique and cutting speed and the progress of tool wear.

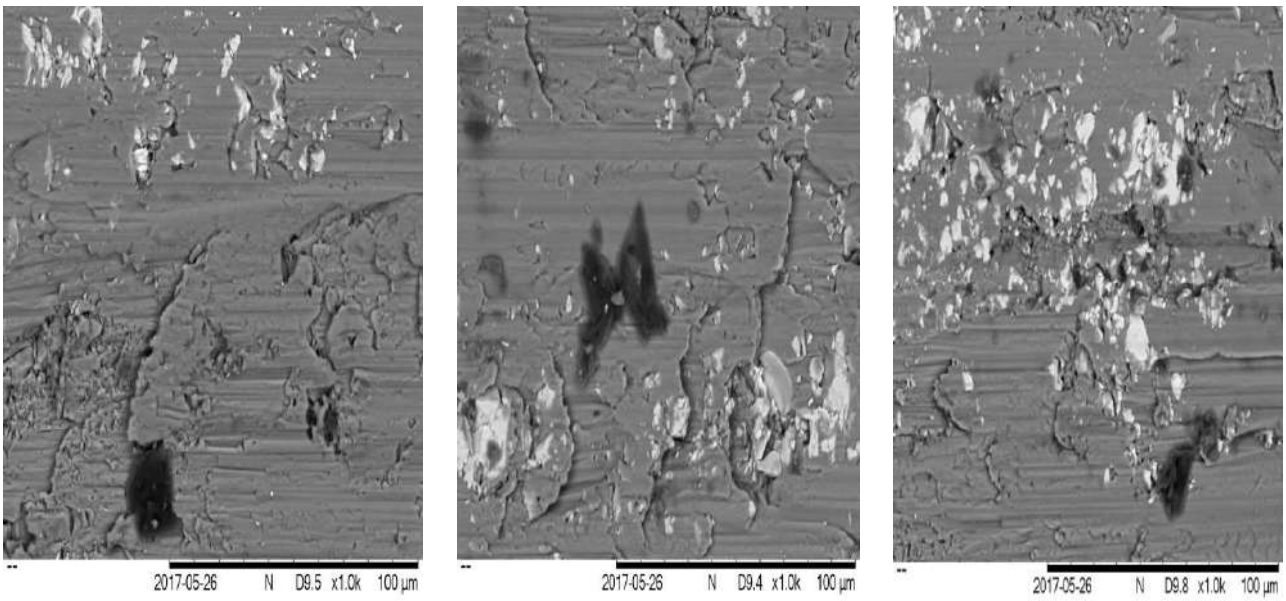

(a) 1.0 mm nozzle orifice **(b) wet coolant** **(c) Dry machining**

FIGURE 5. SCHEMATIC ILLUSTRATION SURFACE ROUGHNESS BETWEEN 1.0 mm NOZZLE ORIFICE, WET COOLANT, AND DRY MACHINING

3.2 Tool Wear

3.2.1 Effect of tool wear

NORMAL INSERT

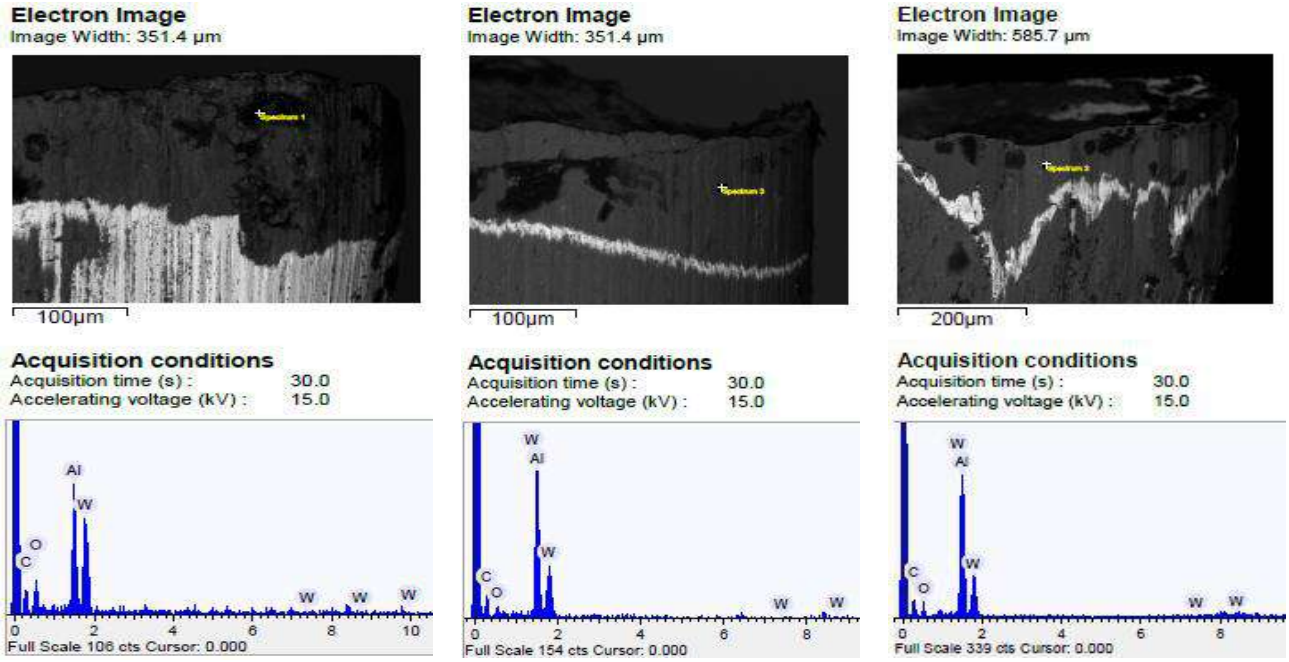

(a) 1.0 mm nozzle orifice (b) wet coolant (c) Dry machining

FIGURE 6. SCHEMATIC ILLUSTRATION BETWEEN 1.0 mm NOZZLE ORIFICE, WET COOLANT, AND DRY MACHINING

Fig. 6a, 6b, and 6c shows the variation in flank wear with machining time under 1.0 mm nozzle orifice, wet coolant and dry machining under coolant technique condition. 1.0 mm nozzle orifice reduces average auxiliary flank wear on auxiliary cutting edge. The temperature also grew very low considerably. It appears on Figure 3 that temperature and flank wear grows quite fast under dry machining due to more intensive temperature and stress at the too-tips. 1.0 mm nozzle orifice technique appeared to be more effective in reducing tool wear and temperature. However, it is evident that coolant technique condition appeared to be effective in reducing tool wear and temperature as well as controlling the deterioration of the auxiliary cutting edge by thermal effect to adhesive wear and built - up edge formation.

IV. OPTIMIZATION

In this study, RSM has been utilized for single response optimization. The use of response surface optimization helps to calculate the optimal values of input in order to minimize the surface roughness during the turning process of Aluminum alloy 319. The constraints for optimization of cutting parameters have been shown in table 5. Table 6 shows the values for the input parameters for minimizing surface roughness. It is clearly seen that obtained optimal value is 0.74 (µm) for the respective values of cutting speed, depth of cut and feed rate.

TABLE 5
CONSTRAINTS FOR OPTIMIZATION OF PARAMETER

Parameter	Lower limit	Higher limit
Cutting speed (rpm)	150	270
Depth of cut (mm)	0.2	1.0
Feed Rate (mm/rev)	0.05	0.24
Environments Cutting	Dry , Wet and Nozzle Size 1.0 mm	

TABLE 6
OPTIMIZATION RESULTS

Cutting Speed	Depth of Cut	Feed Rate	Flank wear	Desirability
150	0.2	0.08	0.34	0.8352

4.1 Confirmation Test

Fig. 7. shows the variation in flank wear with cutting speed under aluminum alloy 319 with 1.0 mm nozzle size) wet and dry coolant environments. As 1.0 mm nozzle size reduces average auxiliary flank wear on auxiliary cutting edge, temperature also grew very lower under 1.0 mm nozzle size coolant condition. It appears that temperature and flank wear grows quite fast under dry machining due to more intensive temperature and stresses at the tool-tips, 1.0 mm nozzle coolant techniques appeared to be effective in reducing tool wear. However, the variation in machining time with flank wear, it is evident that 1.0 mm nozzle coolant techniques improves and mainly through controlling the deterioration of the auxiliary cutting edge by thermal effect to adhesive wear and built - up edge formation.

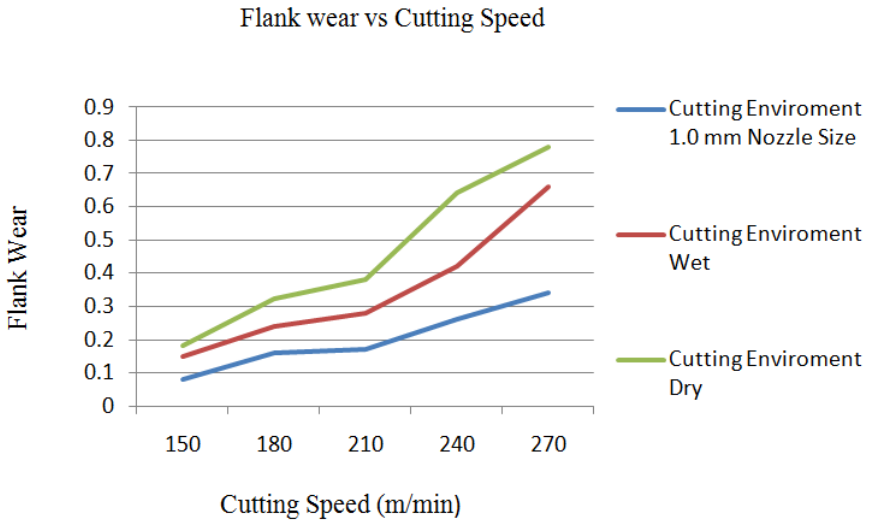

FIG.7. EFFECT OF TECHNIQUE COOLANT APPLICATION METHOD ON THE RESULTANT FLANK WEAR (VS 150, DEPTH OF CUT 0.2 AND FEED RATE 0.08, CEMENTED COATED CARBIDE)

V. CONCLUSION

In conclusion, the effects of surface roughness and tool wear on coolant condition technique on different parameters like cutting speed, feed rate and depth of cut can be summarized as below:

- Data extrapolated from experiment result average resultant of surface roughness and flank wear progress indicated that the optimal performance of the cemented coated carbide insert was obtained when using 1.0 mm nozzle size method of coolant.
- Tool wear management is also an issue that needs further investigation; the result indicated that up to a cutting speed of 270 mm/min, a tool wear are generated and course surface roughness.

- The optimization values of cutting parameters have been achieved for minimum surface roughness with desirability of 0.8352 %, which is highly acceptable.
- The technique condition nozzle size 1.0 mm, mean smaller nozzle opening focuses the coolant flow to a smaller area, eliminating the waste of wide spray of coolant and provides a more concentrated flow which is a relatively new technique of technology that allows cutting fluid to penetrate tool workpiece and tool chip interfaces.

ACKNOWLEDGEMENT

The author would like to thanks TATI University College (TATIUC) for fully supported by TATIUC grant, no. (9001 – 1201), University Malaysia Pahang (UMP) for providing the equipments and supervision makes this important research viable and effective.

REFERENCES

[1] K. Wegener, F. Kuster, S. Weikert, L. Weiss, and J. Stirnimann, "Success Story Cutting," *Procedia CIRP*, vol. 46, pp. 512-524, 2016.

[2] M. C. Shaw and J. Cookson, *Metal cutting principles* vol. 2: Oxford university press New York, 2005.

[3] R. Nur, M. Noordin, S. Izman, and D. Kurniawan, "Machining parameters effect in dry turning of AISI 316L stainless steel using coated carbide tools," *Proceedings of the Institution of Mechanical Engineers, Part E: Journal of Process Mechanical Engineering*, p. 0954408915624861, 2015.

[4] C. Camposeco-Negrete, "Optimization of cutting parameters using Response Surface Method for minimizing energy consumption and maximizing cutting quality in turning of AISI 6061 T6 aluminum," *Journal of cleaner production*, vol. 91, pp. 109-117, 2015.

[5] A. J. Makadia and J. Nanavati, "Optimisation of machining parameters for turning operations based on response surface methodology," *Measurement*, vol. 46, pp. 1521-1529, 2013.

[6] V. Kryzhanivskyy, V. Bushlya, O. Gutnichenko, I. Petrusha, and J.-E. Ståhl, "Modelling and Experimental Investigation of Cutting Temperature when Rough Turning Hardened Tool Steel with PCBN Tools," *Procedia CIRP*, vol. 31, pp. 489-495, 2015.

[7] M. Dhananchezian, M. P. Kumar, and A. Rajadurai, "Experimental investigation of cryogenic cooling by liquid nitrogen in the orthogonal machining process," 2009.

[8] Y. Isik, "An Experimental investigation on effect of cutting fluids in turning with coated carbides tool," *J. Mech. Eng*, vol. 56, pp. 195-201, 2010.

[9] A. Kus, Y. Isik, M. C. Cakir, S. Coşkun, and K. Özdemir, "Thermocouple and infrared sensor-based measurement of temperature distribution in metal cutting," *Sensors*, vol. 15, pp. 1274-1291, 2015.

[10] Z. A. Selamat, N. B. Baba, M. Alias, A. R. Yusoff, and M. M. Rahman, "Effect of coolant nozzle sizes on turning aluminum alloy AL319," *Indian Journal of Science and Technology*, vol. 9, 2016.

[11] L. Abhang and M. Hameedullah, "Chip-tool interface temperature prediction model for turning process," *International Journal of Engineering Science and Technology*, vol. 2, pp. 382-393, 2010.

[12] E. Ezugwu, A. Machado, I. Pashby, and J. Wallbank, "The effect of high-pressure coolant supply when machining a heat-resistant nickel-based superalloy," *Lubrication Engineering*, vol. 47, pp. 751-757, 1991.

[13] M. S. Kasim, "Comparison between Taguchi method and response surface methodology (RSM) in optimizing machining condition," in *Proceeding of 1st International Conference on Robust Quality Engineering*, 2013, pp. 60-68.

Fabrication of 3D Thin Films by Spray Pyrolysis Method from Metal Phthalocyanines

Antonio Alanis[1], Oxana Kharissova[2]*, Servando Aguire[3], Romeo Selvas[4], Carlos Luna[5], Idalia Gomez[6], Jiechao Jiang[7]

[1,2,4,5]Department of Fisico-Mathematical Sciences, Universidad Autónoma de Nuevo León, Ave. Universidad s/n, Ciudad Universitaria, San Nicolas de los Garza, Nuevo Leon,C.P. 66455, México.
[3]CIMAV, Alianza Norte 202, Parque de Investigación e Innovación Tecnológica, Apodaca, Nuevo Leon, C.P. 66628, Mexico.
[6]Department of Chemical Sciences, Universidad Autónoma de Nuevo León, Ave. Universidad s/n, ciudad Universitaria, San Nicolas de los Garza, Nuevo Leon, C.P. 66455, México
[7]Materials Science and Engineering Department, University of Texas at Arlington, Arlington, TX 76019, USA.

Abstract*—Carbon 3D structures were obtained by spray pyrolysis using toluene solution containing suspended nickel or magnesium phthalocyanines as precursors of metallic particles serving as catalysts for carbon phase formation. The process was conducted in a range of temperatures in a quartz tube in inert atmosphere on borosilicate glass supports where the nanometric layers of nanoparticles were deposited. The samples were analyzed by Scanning Electron Microscopy (SEM), Transmission Electron Microscopy (TEM), Infrared Spectroscopy Fourier Transform (FTIR) and Raman spectroscopy; their condusctivity was measured via Kelvin technique. The properties of formed nanolayers were analyzed according to metal nature in the phthalocyanine, temperature, carrier gas speed, and other process parameters. Possible MEMS applications of thus fabricated nanolayers are discussed.*

***Keywords*—carbon nanotubes,phthalocyanines, Raman, spray pyrolysis, TEM.**

I. INTRODUCTION

One of the emerging research areas aimed at improving the physicochemical properties of metallophthalocyanines is "nanostructuring". The spectrum of nanomaterials used in sensors is wide; the analysis of recent publications has made possible to identify various nanomaterials that have found applications as chemical sensors [1-9]. These include the following groups of nanomaterials: 1) nanoparticles, nanoclusters, nanocrystals and quantum dots, used mainly in optical, including biochemical immunosensors, less often in electrochemical sensors; 2) nanotubes, nanorods, nanowires, nanowires, used primarily in electrical (field effect transistor) and electrochemical sensors, less often in optical (biochemical) and piezosensors; 3) sensors based on the use of nanoscale organized film structures (Langmuir-Blodgett films and self-assembled mono- and multilayers), used mainly in optical, surface-acoustic and piezo-quartz (volume-acoustic) sensors. All kinds of nanoscale particles can be embedded in various organic or inorganic matrices (monolayers or films). Nanosensors based on such composite materials are used mainly for the detection of gases, although there are examples of their use in the analysis of liquid media. Carbon nanotubes have a number of unique properties that make their use promising in chemical sensors [10,11], and a wide range of electrical properties. Most of the tubes are semiconductors, but there are excellent conductors (in particular, better than silver) and even insulators. The conductivity of a nanotube depends on its geometric structure.

Phthalocyanine-based macrocycle systems (Pc) and their metal complexes (MPc) are promising candidates for classic applications, such as, for example, pigments [12], solar [13] and fuel cells [14], catalysts [15], semiconductors [16], gas sensors [17], corrosion inhibitors [18], electronic [19] and optical [20] devices, liquid crystalline materials [21], but also for design of nanomaterials [22,23]. Their surface chemistry [23] is a relatively young and growing field of research, caused by the tremendous versatility of these molecules and their metal complexes. Phthalocyanine complexes are formed with most metallic elements of the periodic system and, depending on the type of metal center, enormous variations in reactivity, electronic and magnetic properties and biological functionality can be found. Phthalocyanines share the conjugated π-extended system with porphyrins and, therefore, also share the ability of a strong absorption of light in the visible range. These macrocycles are thermally very stable and up to 500-800 K, so their thin films can be easily prepared by organic molecular beam epitaxy (OMBE) in vacuum [24]. Exploiting the intrinsic electronic, optic and spintronic properties of novel low-dimensional molecular materials, it is required that the electronic coupling with the supporting substrate is kept as low as possible. In this context, metal-supported ultra-thin insulating films on phthalocyanine basis have attracted great interest as

substrates to study the intrinsic properties of organic and inorganic nanostructures. Obtaining matrices of uniformly oriented carbon nanotubes (CNTs) will significantly accelerate their use in electronics. Vertically oriented (with respect to the substrate) CNTs, used, for example, for field emission cathodes, are synthesized using various variants of the CVD method. It is much more difficult to lay the CNT horizontally, but this is what is required for most electronic devices. It is also known that several phthalocyanines are capable to form composites with carbon nanotubes (CNTs) [25] and graphene [26], as well as to destroy completely CNTs [27]. So, the main goal of this work was the *in situ* study of formation of thin films from the toluene-phthalocyanine system by spray pyrolysis, characterization and search of possible applications.

II. EXPERIMENTAL PART

Metal phthalocyanines MPc (M = Cu, Ni, Mg, Zn; 97% purity) were purchased from Sigma-Aldrich Company and used as supplied. Toluene and ethanol were purchased in CTR (Monterrey, Mexico). Electron microscopy images were made in SEM and TEM equipment at the University of Texas at Arlington (TX, USA). IR-spectra were measured in ThermoScientific Nicolet equipment. Raman spectra (DXR Raman Microscope ThermoScientific) were collected using an excitation wavelength of 785 nm (1.58 eV).

Using MPc (M = Cu, Ni, Mg, Zn) as precursors, carbon thin films were prepared by a spray-pyrolysis technique using the powders of MPc, dispersed in a mixture of toluene (C_7H_8) and EtOH o mixture of toluene (C_7H_8) and ferrocene. The MPc concentration in each sample was in the range of 0.05 wt.%, 0.5 wt.% and 1.wt.%. Solvent(20 mL, toluene and alcohol (1:1) and MPc o solvent(20 mL, toluene andferrocene (0.05 wt.%) and MPc was injected to the system at a rate of 1 mL/min in a preheater set to 200^{0}C while nitrogen gas is supplied at a ratio of 1 L/min. After the preheater, the gas passed into a quartz tube which entered in an oven heated at 760°C. This quartz tube contained borosilicate glass substrates, where thin nanofilms were deposited by 20 min. (Fig. 1).

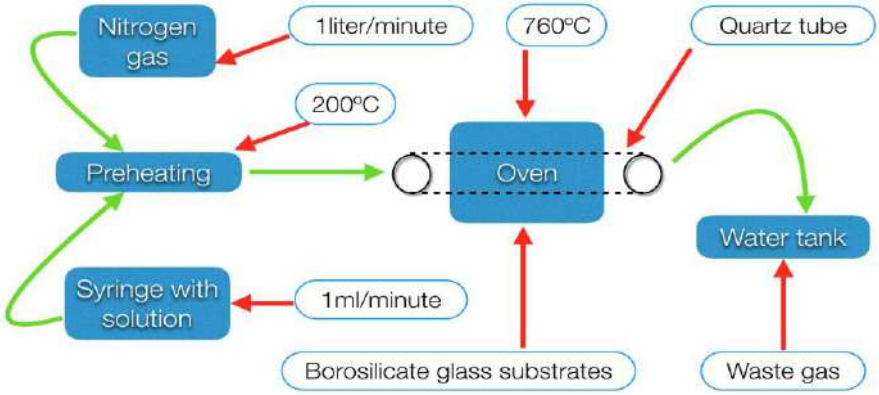

FIG. 1. The spray pyrolysis system.

The samples were characterized through scanning electron microscopy (SEM), transmission electron microscopy (TEM), by Raman and infrared spectroscopy (IR). The electrical measurements were carried out using the technique Kelvin-4 points. This method of measurement is the Kelvin, or 4-wire method. Special connecting clips called Kelvin clips are made to facilitate this kind of connection across a subject resistance (Fig. 2).

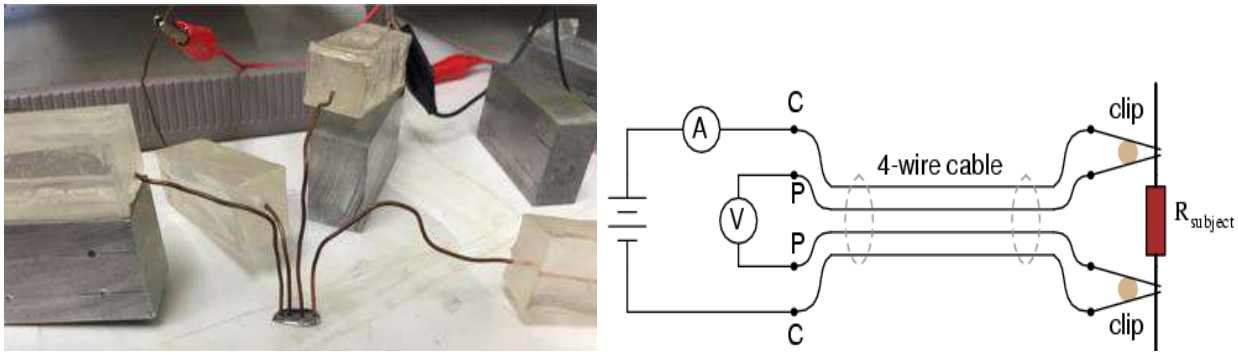

FIG. 2. Kelvin (4 wire sensing) measurements.

III. RESULTS AND DISCUSSION

As a result of this work, the nanometric layers of carbon nanoparticles were deposited on quartz glass. These films were analyzed by scanning electron microscopy. First, the mixture of toluene (C_7H_8) and EtOH with different concentration of MPc in each sample (0.05 wt.%, 0.5 wt.% and 1 wt.%) (Fig. 3) was analyzed. As it is seen in SEM images, the morphology and thickness of the thin films varies (Table 1).

TABLE 1
DEPOSITION PARAMETERS AND RESULTING THIN FILM THICKNESS.

Precursor	Concentration (wt.%)	Temperature of deposition (°C)	Time of deposition (min)	Thickness (nm)
MgPc	1. 0	760	20	1050
MgPc	0.5	760	20	481
MgPc	0.05	760	20	175
NiPc	1.0	760	20	3458
NiPc	0.5	760	20	1037
NiPc	0.05	760	20	420
CuPc	1.0	760	20	439
CuPc	0.5	760	20	158
CuPc	0.05	760	20	12
ZnPc	1.0	760	20	854
ZnPc	0.5	760	20	857
ZnPc	0.05	760	20	48

The SEM and TEM data (Fig. 3) show that the MgPc blends allow obtaining the nanoparticles of 5-20 nm sizes (Fig. 3B) for 0.5 wt.% concentrations. The morphology of deposited particles at concentrations of 0.5 wt. % and 1.0 wt.% is shown in Fig. 3D. The morphology of the particles of larger sizes of 22-37 nm is present in the samples with ZnPc for concentrations 0.05 wt.% (Fig. 3J) and increasing to 285-857 nm for concentrations of 1.0 wt.% (Fig. 3M).According to the obtained results, different polymorphic phases of thin carbonaceous films were observed. Structural and morphological changes were found to be dependent on the nature of MPc.SEM data (Fig. 3) show that MgPc nanoparticles have sizes from 10 to 25 nm (Fig. 3B) and 20 nm (Fig. 3A), respectively. In the image profile of the sample of 0.5% NiPc as precursor (Fig. 3G), it is shown how the nanoparticles are joined to the surface of borosilicate glass substrate.

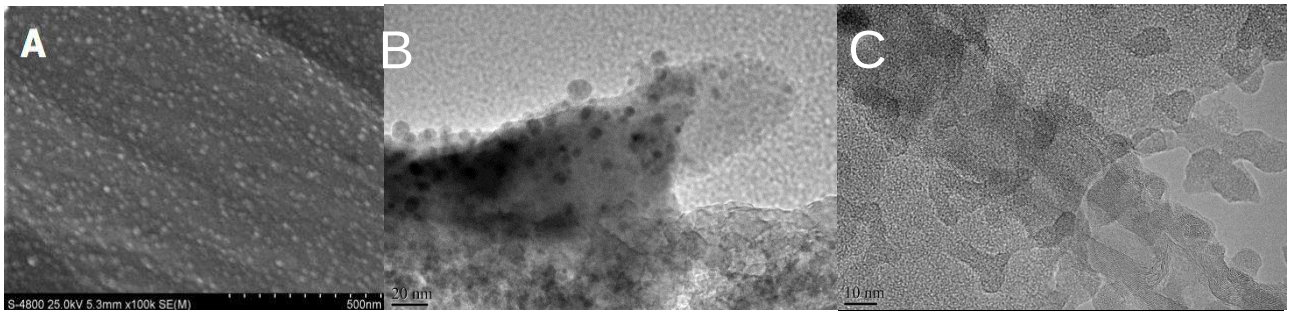

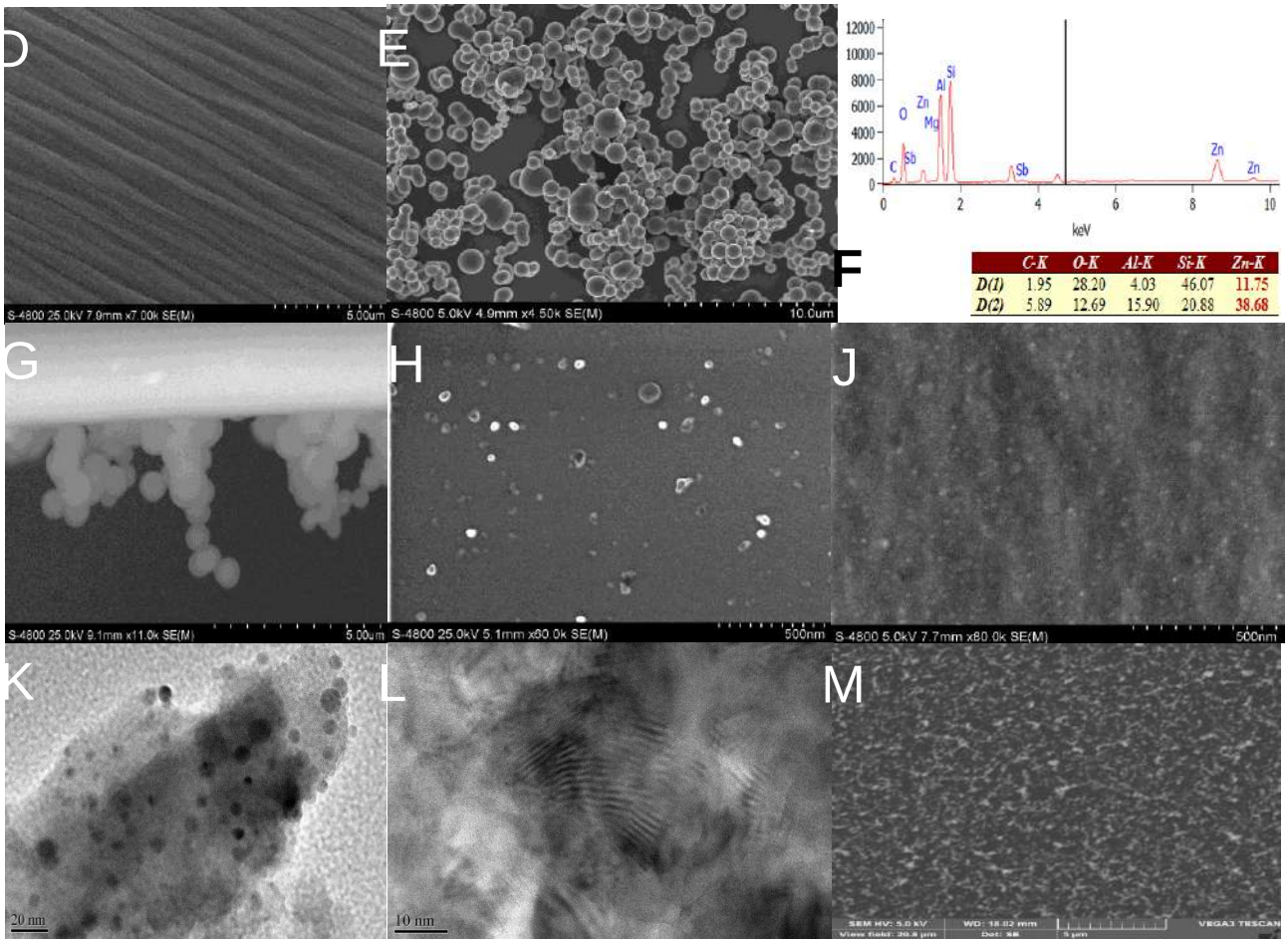

FIG. 3. Images of samples prepared using the following metal phthalocyanine precursors: A) SEM of MgPc 0.5 wt.%; B) TEM of MgPc 0.5 wt.%; C) TEM of MgPc 1.0 wt.%; D) SEM of MgPc 1.0 wt.%; E) SEM of NiPc 1.0 wt.%; F) EDS of ZnPc 1.0 wt.%; G) SEM of NiPc 0.5 wt.%; H) SEM of NiPc 0.05 wt.%; J) SEM of ZnPc 0.05 wt.%; K) TEM of ZnPc 0.5 wt.%; L) TEM of NiPc 1.0 wt.%; M) SEM of ZnPc 1.0 wt.%.

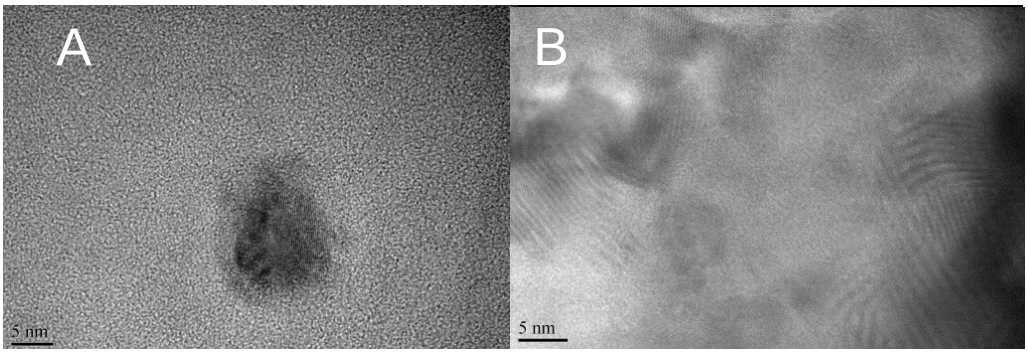

FIG. 4. TEM images of samples prepared using the CuPc precursors: A) TEM of CuPc 0.5 wt.%; B) TEM of CuPc 1.0 wt.%.

They have a size of 10-12 nm of the sample of 0.05% NiPc as precursor (Fig. 3H). The diameter of nanoparticles in case of CuPc use as a precursor is 15 nm (Fig. 4A). The thickness of thin film of the sample was found to be in the range of 20÷1000 nm in case of homogeneous deposition (samples NiPc, CuPc and MgPc); however, in case of the sample Fig. 3E (ZnPc as a precursor) the deposition was not homogeneous and the thickness varies up to 3400 nm (Table 1). The TEM data reveal (Fig. 3 y Fig. 4) that the mixture with NiPc and CuPc allows obtaining nanoparticles of sizes 5-10 nm (Fig. 4A and Fig. 3H) for concentrations of 0.05 wt.%, 0.5 wt.% and formation of carbon nanotubes of SWCNT with diameter of 1.25 nm (Fig. 3L y Fig. 4B) for concentrations of 1.0 wt.%.

The Raman spectra of the samples are shown in Fig. 5. The modes of radial respiration (RBM) at $140 \leq \nu \leq 350$ cm^{-1} is characteristic for SWCNTs, they are clearly present in all samples. The tangential G band at 1600 cm^{-1}, whose profile indicates the metallic or semiconductor character of the CNTs, and the bands D at 1332 cm^{-1} (disorder-induced) and G' at 2650 cm^{-1} (overtone D) are also observed. The band D is indicative of the presence of defects in the walls, so the ratio of intensities of the D and G bands can testify about the number of defects [28]. In the Raman spectrum of samples, in addition to the bands G, D and G', a group of very intense bands centered at 200 cm^{-1} was observed, which are characteristics of SWNTs ($140 \leq \nu \leq 350$ cm^{-1}) corresponding to the characteristic respiratory mode in radial direction (radial breathing mode RBM) of SWCNTs and inverse linearly depends CNT diameter. Since the radial breathing mode frequency ω_{RBM} depends linearly on the reciprocal nanotube diameter d_t.

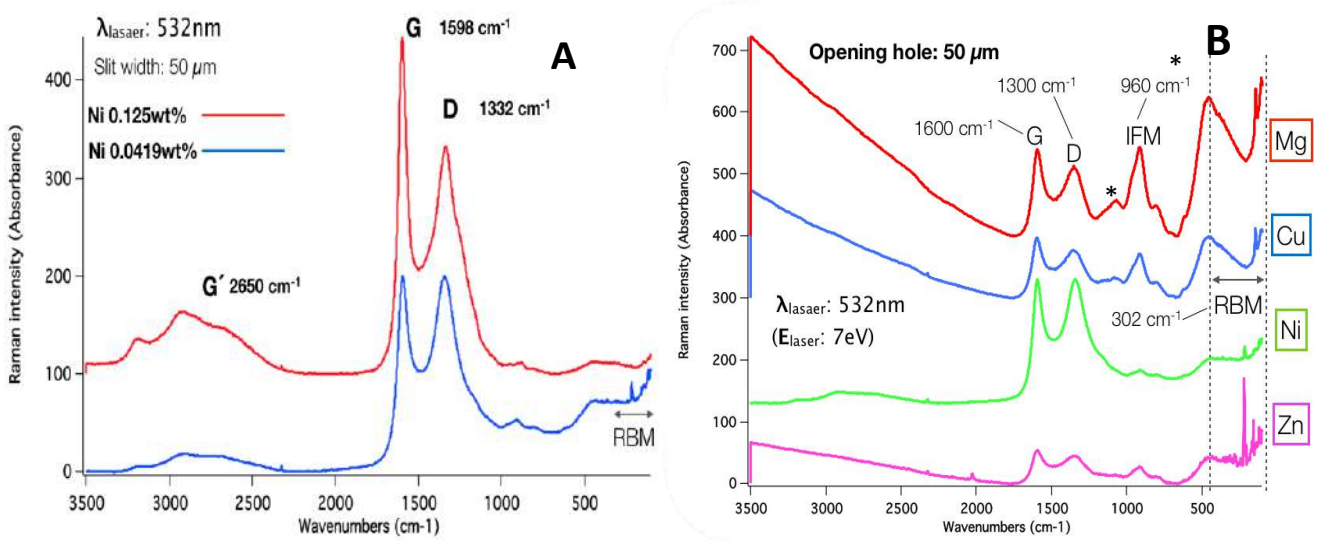

FIG. 5. Raman spectra of thin films: a) comparison of NiPc composites at different concentrations; b) comparison of samples obtained by pyrolysis using different MPc at 0.5 wt.%. (RBM is Radial Breathing Mode $140 \leq \nu \leq 350$ cm^{-1}) and IFM (intermediate frequency modes IFM^{-}= 750 cm^{-1}, IFM^{+}= 960 cm^{-1}).The features marked with '*' at 248, 521 and 962 cm^{-1} are from the Si/SiO$_2$ substrate and are used for calibration of the nanotube Raman spectrum [29]).

They can also correspond to other second-order vibrations as IFM (intermediate frequency modes) at 960 cm^{-1} (weaker bands). The first band D appears at ~1300 cm^{-1}, indicating the disorder of graphite. A strong increase of the band G is seen at 1600 cm^{-1} (vibration mode A1G). In case of NiPc use (Fig. 8a), a band at ~2700 cm^{-1} confirms the stacking of graphene layers. The G-band is highly sensitive to strain effects in sp^2 system, and thus can be used to probe modification on the flat surface of graphene.

Results of Kelvin (4 wire sensing) measurements. Voltage measurements against the current to a very small scale of the order of nano amperes in DC were made. The slope of the graph obtained in each of the samples being resistance is in the range of kilo ohms is achieved (Fig. 2). The summary of the readings taken with the technique Kelvin (4 wire sensing) is shown in Table 2. It was observed that there are three possible scenarios when depositing nanometer-thin layer of material on the substrate borosilicate glass as follows. 1) The nanometer-scale material is deposited on both sides of the substrate, 2) the material is deposited only on one side of the substrate, and 3) the nanometer material is deposited on any side of the substrate. This depends largely on the location of the substrate within the quartz tube, that is, if nothing is deposited in the terminals, if in the center, melts due to the high temperatures handled in the pyrolysis technique. It is recommended to place the substrates at a distance of 15 cm from the outside in the tube. Comparing the measurements of the samples from Table 2 we found that using only NiPc and MgPc in percentages 0.5 wt.% and 1.0 wt.%, the resistance is relatively very high (from 25 kΩ to 75 kΩ) having a very high current small but effective from 7.9 nA to 20.6 nA being sufficient to operate a MEMS.

TABLE 2
SUMMARY OF THE MEASUREMENTS OF FOUR POINTS SAMPLES PYROLYSIS

Toluene with	Concentration wt%	Initial voltage µvolts	Final voltage mvolts	Initial current nA	Final current nA	Resistance kΩ
MgPc	0.5	320	2.79	16.64	100	29.681
	1	226	2.25	20.60	100	25.477
NiPc	0.5	558	61.1	9.40	1000	61.156
	1	393	7.39	7.96	100	75.972
ZnPc	0.5	428	2.47	14.23	100	17.356
CuPc	0.5	341	7.01	21.45	1000	15.34

The metal-phthalocyanines (MPc) is very sensitive and selective to different gases and solvents as an account of the central metal atoms of the molecule, which can easily be varied. The surface morphologies and the grain boundaries of organic thin films can influence the sensing property of OTFT sensors.The sensitivities of the MPcs (ZnPcs, MgPc, CuPc, NiPc) to hydrogen peroxide may be determined as the slope (% ppm^{-1}) of the sensor. The linear fits of responses versus concentration show modest non-ideal behavior in that the intercepts are non-zero; this is likely due to the influence of the water present in each dose, which acts as an offset. Sensitivities are presented in Table 3**.**The reaction of NiPc, CuPc, ZnPc, and H_2Pc with hydrogen peroxide can be portrayed as a radical reaction (1) or as a charge transfer process (2) following coordination:

$$MPc + HOOH \rightarrow MPC^{\bullet+} + OH^- + {}^{\bullet}OH \quad (1)$$

$$MPc + HOOH \rightarrow [MPc \text{ --- } HOOH \longleftrightarrow MPc^{\delta+} \text{ --- } HOOH^{\delta-}] \quad (2)$$

TABLE 3
Sensitivities (% ppm^{-1}) for MPcs (M = Mg, Ni, Cu, Zn, H_2) to 25% H_2O_2(aq) and di-*t*-butyl peroxide vapors in the kinetic dosing regimen at 50°C and 8 V.

MPc	Hydrogen peroxide sensitivities (% ppm^{-1}) x 10^{-2}	Di-*t*-butyl peroxide sensitivities (% ppm^{-1}) x 10^{-2}
ZnPc	2.5±0.7	0.4±0.2
CuPc	29.2±5.3	3.5±1.3
NiPc	2.2±0.8	0.3±0.1
MgPc	2.1±0.6	0.4±0.2
H_2Pc	26.4±4.9	0

IV. CONCLUSIONS

SWCNT monolayers having diameters of 1.45 nm were obtained by spray pyrolysis of toluene-ethanol dispersion of metal phthalocyanines as precursors of catalysts for carbon nanotube formation. Thin layers of nanomaterials were deposited on borosilicate glass and were found to conduct in nanoamper scale. The deposited material may be present on both sides of the substrate or on one side only. The nanoparticles were homogeneously distributed and have diameters of 20 nm and 750 nm for magnesium and nickel phthalocyanines used as precursors, respectively.

The G, D and G' characteristic bands of SWCNTs were confirmed by Raman spectroscopy, as well as other intense bands in the range of 140 to 350 cm^{-1} corresponding to RBM (radial breathing mode) and a less intensive band intermediate frequency modes (IFM) 750 cm^{-1}, 960 cm^{-1} corresponding to the IFM^- and IFM^+.

ACKNOWLEDGEMENTS

The authors gratefully acknowledge the helpful to the CONACYT-Mexico for Ph.D. scholarship for Antonio Alanis.

REFERENCES

[1] Riu J., Maroto A., Rius F.X. Talanta, 2006, v. 69, p. 288—301.

[2] Shi J., Zhu Y., Zhang X., Baeyens W.R.G., Garcia-Campana A.M. Trends Anal. Chem., 2004, v. 23, 5, p. 351-360.

[3] Costa-Fernandez J.M., Pereiro R., Sanz-Medel A. Ibid., 2006, v. 25, 3, p. 207-218.

[4] Huang X.-J., Choi Y.-K. Sensors and Actuators B, 2007, v. 122, p. 659-671.

[5] He L., Toh C.-S. Anal. Chim. Acta, 2006, v. 556, p. 1-15.

[6] Jeronimo P.C.A., Araujo A.N., Montenegro M.C.B.S.M. Talanta, 2007, v. 72, p. 13-27.

[7] Tansil N.C., Gao Z. Nanotoday, 2006, v.1, № 1, p.28-37.

[8] Vaseashta A., Dimova-Malinovska D. Sci. Technol. Adv. Mater., 2006, v. 6, p. 312-318.

[9] James S.W., Tatam R.P. J. Opt. A: Pure Appl. Opt., 2006, v. 8, p. 430-444

[10] Merkoci A. Microchim. Acta, 2006, v. 152, p.157-164.

[11] Wildgoose G.G., Banks C.E., Levebtis H.C., Compton R.G. Ibid., 2006, v. 152, p. 187-214

[12] Sakamoto K., Okumura E., Materials 2009, 2, 1127-1179.

[13] Walter P.M.G., Rudine A.B., Wamser C.C. J. Porphyrins Phthalocyanines 2010, 14, p. 759-792.

[14] Burkitt R., Whiffen T.R., Hao Yu E., Applied Catalysis B: Environmental, 2016, v. 181, p. 279-288.

[15] Ma J., Liu Y., Zhang P., Wang J. Electrochemistry Communications 2008 v. 10(1) p. 100-102.

[16] Sorokin A.B. Chem. Rev., 2013, 113(10), p. 8152–8191

[17] Patois T., Sanchez J.B., Berger F., Fievet P., Segut O., Moutarlier V., Bouvet M., Lakard B., Talanta. 2013, 117, p.45-54

[18] Peng Zhao, Qiang Liang, Yan Li. Applied Surface Science, 2005, 252, p. 1596-1607.

[19] Raval H.N., Sutar D.S., Ramgopal Rao V. Organic Electronics, 2013, v. 14, 5, p 1281–1290

[20] Rodríguez Gómez A., Sánchez-Hernández C.M., Fleitman-Levin I., Arenas-Alatorre J., Alonso-Huitrón J.C., Sánchez Vergara M.E., Materials, 2014, 7, p.6585-6603.

[21] Iannuzzi M., Tran F., Widmer R., Diene T., Radican K., Ding Y., Hutter J., Gröning O. *Physical Chemistry Chemical Physics*. 2014, **16** (24), p.12374

[22] Nilson K., Ahlund J., Shariati M., Gothelid E., Palmgren P., Schiessling J., Berner S., Martensso N. and Puglia C. J. Phys. Chem. C, 2010, 114, p.12166.

[23] Das S., Magut P.K.S., Zhao L., Hasan F., Karki A.B., Jin R. and Warner I.M. RSC Adv., 2015, 5, p.30227-30233.

[24] Gottfried J.M. Surface Science Reports, 2015, v. 70, 3, p. 259-379.

[25] Wang Y., Chen H.-Z., Li H.-Y., Wang M. Materials Science and Engineering: B, Volume 117, Issue 3, 25 March 2005, Pages 296-301.

[26] Mani V., Devasenathipathy R., Chen S.-M., Gu J.-A., Huang S.-T., Renewable Energy, 2015, v.74, p. 867-874.

[27] Kharissova O.V., Dias H.V.R., Kharisov B.I., Jiang J. RSC Advances, 2015, 5, p. 57764-57770.

[28] Dresselhaus M.S., Dresselhaus G., Jorio A., Souza Filho A.G., Saito R. Carbon, 2002, 40, 2043-2061

[29] Temple P.A., Hathaway C.E. Phys Rev B, 1973, 7, p.3685–3697.

Influence of the Cooling Environment on Cutting Temperature and Specific Energy when Turning AISI 4340 Steel

Christianne L. Soares[1], Paulo E. de Faria[2], Augusto M. Martins[3], Antônio Carlos de Andrade[4], Alexandre M. Abrão[5*]

[1,2]Department of Production Engineering, Universidade Federal de Minas Gerais, AvenidaAntônio Carlos, 6627 Pampulha, Belo Horizonte MG, CEP: 3120-901, Brazil
[3,4,5]Department of Mechanical Engineering, Universidade Federal de Minas Gerais, AvenidaAntônio Carlos, 6627 Pampulha, Belo Horizonte MG, CEP: 3120-901, Brazil
*Email: abrao@ufmg.br

Abstract*—Temperature monitoring and controlling is a critical aspect influencing the technical and economic success of metal cutting operations owing to the fact that it affects both the quality of the machined component and the performance of the cutting tool. The aim of this work is to investigate the influence of the cutting parameters on tool temperature when turning AISI 4340 steel under three cooling environments: flooding, minimal quantity lubrication and dry cutting. In addition to that, the specific cutting energy required under each cooling environment was measured using a modified impact testing machine, thus allowing the estimate of the temperature associated with the chip formation mechanism. Furthermore, it is aimed at verifying whether this test can replace force measurement using a dynamometer. The findings indicate that the lowest tool temperature was achieved under flood cooling, followed by minimum quantity lubrication and dry cutting. Inversely, lowest specific cutting energy was obtained when dry cutting, followed by minimum quantity lubrication and flooding, thus suggesting that the higher temperatures achieved under dry cutting aid the softening of the work material and the reduction of its shear strength.*

Keywords*—*AISI 4340 steel, specific cutting energy, temperature, turning.

I. INTRODUCTION

The usage of cutting fluids aiming at reducing temperature in cutting zone was first reported by Taylor [1], who manage to increase cutting speed by 40% in turning with the provision of ordinary water as cutting fluid. Ever since, considerable progress has been achieved with regard to cutting fluids formulation and means of application, thus leading to increasing cutting tool life, superior surface finish [2], tighter dimensional accuracy, easiness of chip breakage and transportation [3], machined surface protection against corrosion and reduced cutting forces and energy consumption [4].

Despite the above mentioned benefits, approximately 85% of the cutting fluids used in industry is of mineral basis and therefore offers considerable risk to environment and occupational health and safety during their life cycle [5]. Prolonged contact of cutting fluids may cause dermatitis [6], skin and breathing problems [7], intoxication and cancer [8]. Furthermore, cutting fluid purchase, maintenance and disposal increase production costs. Boubekri, Shaikh & Foster [8] estimate that between 7.5% and 20% of the production costs is related to cutting fluids, while the costs associated with cutting tools are approximately 4%.

Hadad&Sadeghi [2] highlight minimal quantity lubrication (MQL) as an important alternative to flood cooling due to the fact that it combines cooling function with extremely low fluid consumption, which ranges from 10 to 500 ml/h. The influence of the cooling environment (flooding, MQL or dry cutting) on the machinability of TiAl4V when turning with polycrystalline diamond tools was investigated by Revankar et al. [9], who noticed that while MQL provided better surface finish (owing to the reduced friction between tool and workpiece), dry turning promoted higher surface hardness of the machined specimen due to the increase in workpiece temperature combined with higher plastic flow rate when cutting under this condition.

Cutting fluid application at the tool-chip or tool-workpiece interface directly affects cutting temperature. Varadarajan, Philip &Ramamoorthy [10]performed turning trials using AISI 4340 steel as work material and reported lowest temperature using MQL in comparison with dry turning and flooding, under both low and high cutting speeds. The results are explained by the fact that cutting fluid droplets are capable of reaching the interface, making heat transfer more effective.

Work by Li and Liang [11] investigated the influence of cutting fluids on temperature when turning AISI 1045 steel dry, under flooding and using MQL. The cutting tool temperature was measured using an embedded thermocouple while cutting speed, feed rate and depth of cut were varied and the results indicated that tool temperature decreased by 22,1% for MQL and

31,4% when flood turning in comparison with dry cutting. Temperature reduction for MQL was attributed to both cooling and lubrication effects, however, temperature reduction under flooding was more effective and produced less aerosol than MQL. Similar work was carried out by Dhar et al. [7], although using AISI 1040 steel as work material. The authors noticed that lower temperatures were obtained with MQL, which might have had greater access to the interface, effectively cooling it due to the reduced contact length between chip and part. Kumar &Ramamoorthy [12] assert that the superior ability of MQL in reducing temperature is due to the fact that heat is removed from the cutting zone by convection and evaporation, whereas in flood cutting convection is the only possible mean for heat transfer.

The aim of this work is to investigate the influence of the cutting parameters and cooling environment on the cutting tool temperature when turning AISI 4340 steel. Moreover, the effect of the cooling environment on the specific cutting energy is studied using an impact testing machine modified to a pendulum scratch testing machine. Using this device and having the heat capacity of the studied material in hand is possible to estimate the temperature associated with the chip formation mechanism and how this phenomenon is affected by cutting fluid application.the introduction of the paper should explain the nature of the problem, previous work, purpose, and the contribution of the paper. The contents of each section may be provided to understand easily about the paper.

II. MATERIALS AND METHODS

AISI 4340 steel was selected as work material. Initially, bars with diameter of 76.2 mm and length of 300 mm were subjected to full annealing (peak temperature of 930^{o} C during five hours) to reach an average hardness value of 193 HV. Continuous turning trials were carried out on a computer numerical control lathe (5.5 kW power and maximum rotational speed of 3500 rpm) employing TiCN/Al_2O_3/TiN coated tungsten carbide inserts (ISO grade P10-P30) as cutting tools. The inserts presented geometry coded CNMG 120408-GN and were mounted on a tool holder code PCLNR 2020K-12.

In order to measure the temperature of the cutting tools during the turning tests using the implanted thermocouple method (type K with wires possessing a diameter of 0.25 mm each), holes with nominal diameter of 1 mm and opposite to the rake face were produced in the inserts using electrical discharge machining (EDM), see Fig. 1. Figure 2 shows a photograph of a sample hole together with its most relevant dimensions.

The average depth of the EDMed holes is 3.7 mm, therefore, considering that the thickness of the inserts is 4.76 mm the thermocouple hot junction was located 1.01 mm beneath the rake face. The thermocouples were connected to a Tektronix TEK DTM510 portable unit (operation range from from -50°C to 1300°C and resolution of 1°C).

FIGURE 1: DRILLING OF INSERTS USING ELECTRICAL DISCHARGE MACHINING

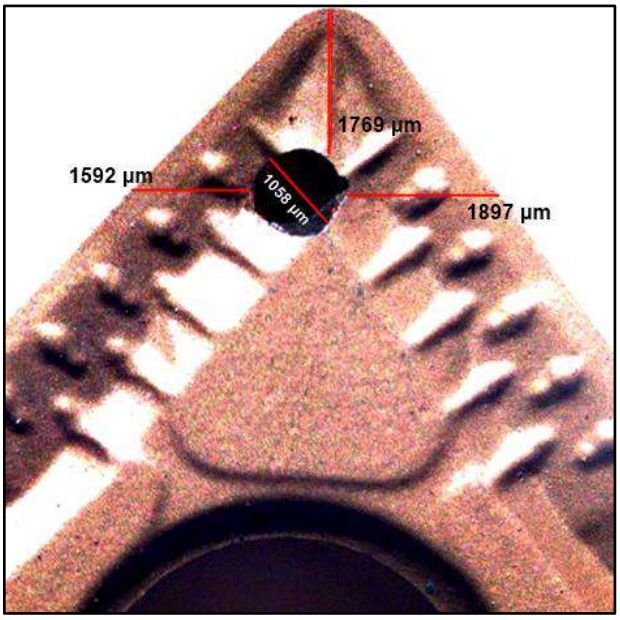

FIGURE 2: COATED TUNGSTEN CARBIDE INSERT WITH HOLE FOR THERMOCOUPLE EMBEDDING

Three cooling environments were employed during the turning tests: flooding (emulsion in a concentration of 5% in water at a pressure of 1 bar and flow rate of 4.3 ℓ/min), minimal quantity lubrication – MQL (vegetal based oil applied at a pressure of 5 bar and flow rate of 60 mℓ/h using Accu-Lube MQL Box Applicator) and dry cutting. For all cooling environments,

cutting fluid was applied at the tool-workpiece interface (clearance face). A fractional factorial experimental design was employed and the cutting conditions are depicted in Table 1. One test plus one replicate were performed for each condition.

TABLE 1
CUTTING CONDITIONS

Level	Cutting speed v_c(m/min)	Feed rate f (mm/rev)	Depth of cut a_p (mm)	Cooling method
-	150	0.15	0.5	Flooding
0	200	-	1.0	MQL
+	250	0.3	1.5	Dry

Additionally to the turning tests, single pass pendulum scratch tests were performed using a modified Gunt Hamburg WP410 impact machine. Instead of an indenter, however, the same tool holder and inserts used in the turning trials were attached to the pendulum. The aim of this test is to measure the specific cutting energy associated with chip formation and verify whether this test can replace force measurement using a dynamometer, which is a much more expensive equipment. Figure 3(a) shows the modified impact machine and Fig. 3(b) presents the tool holder attached to the pendulum. AISI 4340 steel specimen with 10 × 20 × 50 mm (Fig. 3c) were taken from the bars after the turning tests and their mass values were recorded before and after each scratch test using a Mettler Toledo AB204 precision balance (range from 10 g to 210 g and resolution of 0.0001 g).

The same cooling environments used in the turning tests (flooding, MQL and dry cutting) were employed in the pendulum scratch tests, nevertheless, the specimen holder was adjusted in order to allow the removal of a maximum cross section of 1 mm^2. Therefore, the potential energy associated with cutting (chip formation plus ploughing) and sliding can be used to estimate cutting fluid efficiency.

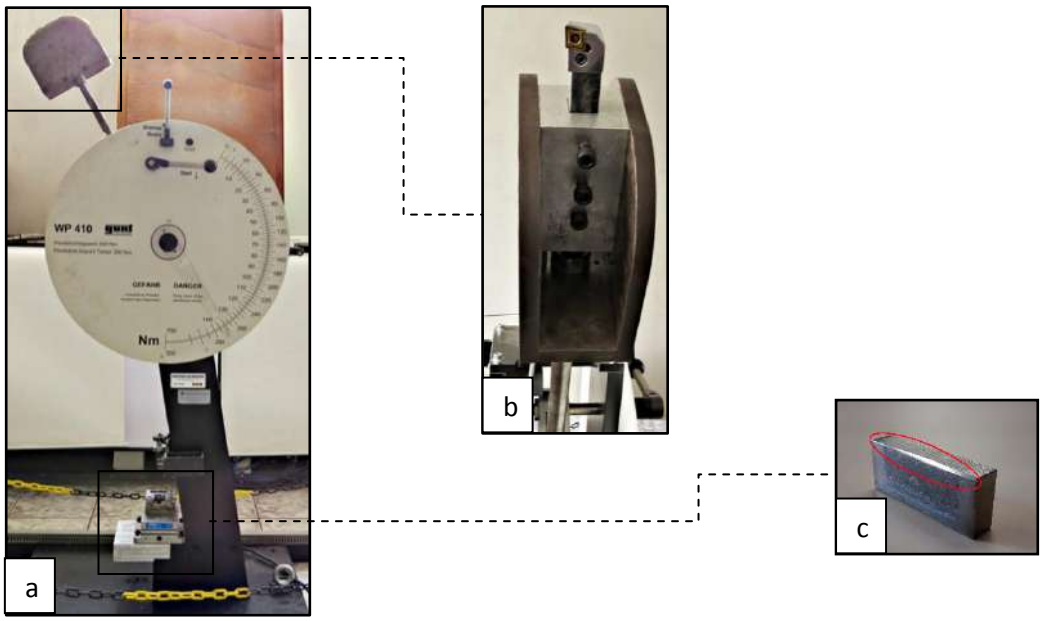

FIGURE 3: MODIFIED IMPACT TESTING MACHINE (A) WITH A DETAIL OF THE TOOL HOLDER ATTACHED TO THE PENDULUM (B) AND A SPECIMEN AFTER TESTED (C)

III. RESULTS AND DISCUSSION

A preliminary test under constant cutting condition (cutting speed of 200 m/min, feed rate of 0.3 mm/rev and depth of cut of 1 mm) was carried out for each cooling environments in order to assess the time required for temperature stabilization at the thermocouple location. For this purpose, the embedded thermocouple was connected to a signal amplifier integrated into a Tektronix TDS1001C-EDU oscilloscope. Figure 4 shows that when flood turning, temperature remains stable after a sudden increase, while when cutting with MQL temperature stabilizes after approximately 20 s and for dry cutting a steady

temperature value is not achieved after turning for 24 s. Based on these data and in order to avoid the influence of tool wear, tool temperature was collected after 15 s for all tested conditions.

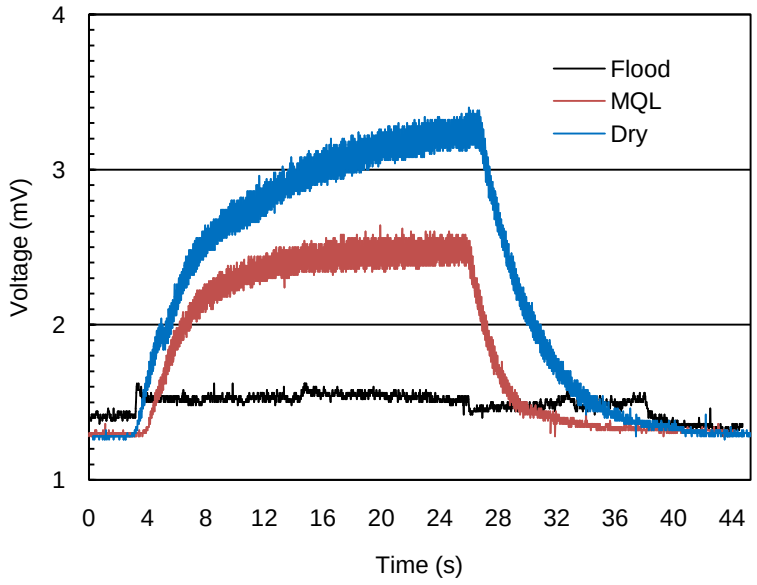

FIGURE 4: TEMPERATURE (VOLTAGE) EVOLUTION AGAINST CUTTING TIME

The influence of cutting speed and cooling environment on cutting tool temperature is represented in Fig. 5. Irrespectively of the cutting speed tested, lowest tool temperatures are obtained with flooding, followed by MQL and by dry cutting. The higher convective coefficient of the cutting fluid applied as a flood together with the reduction of friction by the mineral oil present in the emulsion promotes a steeper temperature reduction. An intermediate condition is observed when minimal quantity lubrication is applied, while the highest temperatures in dry turning indicate that convection to air is insufficient to promote a considerable temperature decrease (under forced convection, the heat transfer coefficient of water is approximately 10 – 20 times higher than that of hot air).

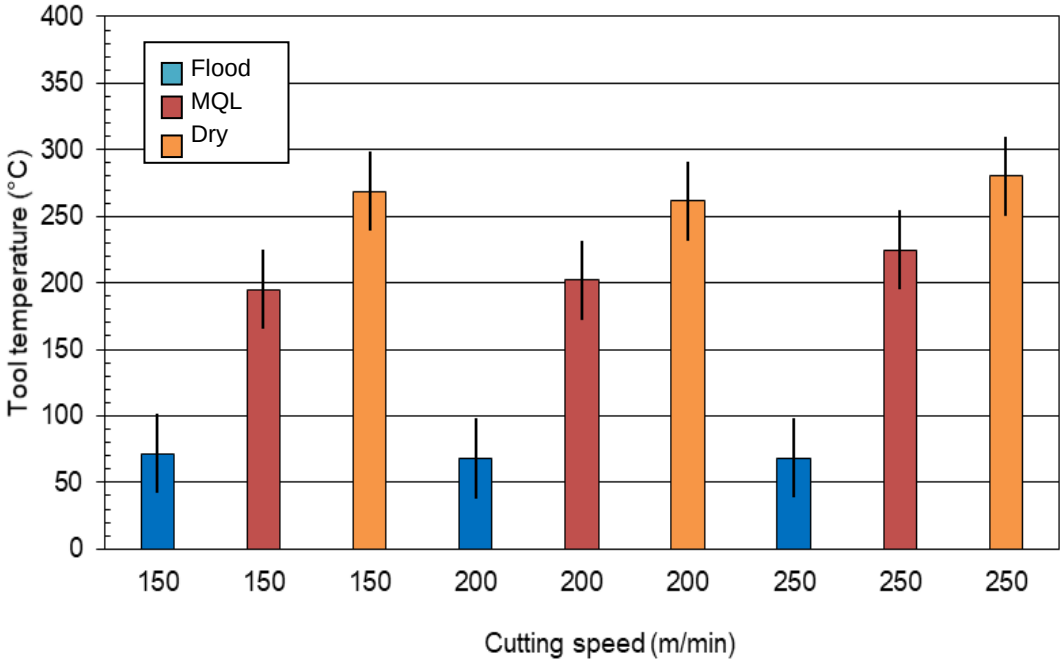

FIGURE 5: EFFECT OF CUTTING SPEED AND COOLING ENVIRONMENT ON TOOL TEMPERATURE (f=0.3 mm/rev and a_p=1 mm)

Table 2 summarises the analysis of variance (ANOVA) results for the influence of cutting speed and cooling environment on temperature (confidence level of 95%), where feed rate and depth of cut were kept constant (f=0.3 mm/rev and a_p=1.0 mm). It can be noted that only cooling environment possesses a significant effect. Within the cutting range tested, the influence of both cutting speed and the interaction between cutting speed and cooling environment are statistically negligible. This behaviour can be explained by the fact that the selected temperature measuring technique is less sensitive to cutting speed owing to the fact that when the latter is increased, chip thickness is reduced, therefore, the heat source moves away from the thermocouple location.

TABLE 2
ANOVA FOR TEMPERATURE CONSIDERING CUTTING SPEED AND COOLING ENVIRONMENT

Factor	p-value
Cutting speed (v_c)	0.073
Cooling environment	0.000
v_c *cooling environment	0.269

The influence of feed rate (f) and depth of cut (a_p) on cutting tool temperature for distinct cooling environments is shown in Fig. 6. Increasing feed rate and depth of cut leads to large shear plane areas and, consequently, higher shear stresses are required, thus resulting in higher temperatures in the cutting zone. Similarly to Fig. 5, cutting fluid applied as a flood was responsible for lower tool temperatures, followed by MQL and dry cutting. One spurious result was observed when turning under flooding using a depth of cut of 1.5 mm, where the temperature recorded for f=0.15 mm/rev was higher than that for f=0.3 mm/rev. One possible explanation for such behaviour may be the undesired change in the position of the thermocouple used in the test at f=0.3 mm/rev farther from cutting zone.

The analysis of variance considering the influence of depth of cutting and cooling environment is summarized in Table 3, however, due to the selected experimental design; it is presented separately for each feed rate. Depth of cut and cooling environment significantly affect cutting tool temperature, irrespectively of the feed rate employed. As far as the interaction between depth of cut and cooling environment is concerned, however, it is statistically significant for the highest feed rate only. A paired t-test was performed for tool temperature measured at different feed rates and the result indicated that they are statistically significant within a 95% confidence level.

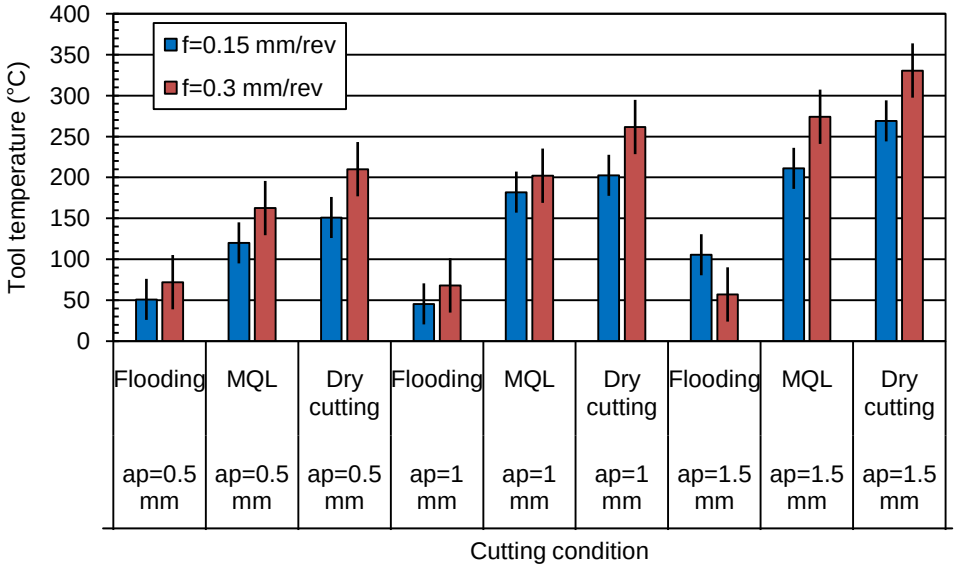

FIGURE 6: EFFECT OF FEED RATE AND DEPTH OF CUT ON TOOL TEMPERATURE (v_c=200 m/min)

TABLE 3
ANOVA FOR TEMPERATURE CONSIDERING DEPTH OF CUT AND COOLING METHOD

Factor	p-value (f=0.15 mm/rev)	p-value (f=0.30 mm/rev)
Depth of cut (a_p)	0.002	0.000
Cooling environment	0.000	0.000
a_p * cooling environment	0.365	0.003

Following the cutting temperature tests, specific cutting energy was measured employing the equipment depicted in Figure 3, however, it is important to point out the fact that the same tool holder and insert geometry as well as tool grade employed in the temperature measurements were used. AISI 4340 steel specimens were mounted in order to allow the removal of a maximum cross section with 1 mm^2 during the test, which represents a two-fold increase in the chip cross section area in comparison with the most severe cutting condition employed in the cutting temperature measurements ($f \times a_p = 0.3 \times 1.5 = 0.45$ mm^2). By converting the gravitational potential energy into kinetic energy the pendulum speed was calculated to be 276 m/min, i.e., slightly above the highest cutting speed used in the temperature measurement trials (v_c=250 m/min).

The average specific cutting energy (u) for each cooling environment is presented in Fig. 7, where it can be noted that the highest value (u=418.1 J/g) was recorded when testing under flooding, followed by cutting under MQL (u=366.9 J/g) and dry cutting (u=347.4 J/g). Two sample t-tests were performed and the results indicated that the specific cutting energy obtained under flooding is not equal to dry cutting within a significance level of 5%, however, the difference between flooding and MQL and between MQL and dry cutting is not statistically significant. The specific cutting energy can be considered as the sum of three components associated with chip formation, ploughing and sliding [13]. These findings indicate that the low oil concentration in the emulsion (5%) does not offer an appreciable contribution towards the reduction of the friction coefficient. Inversely, the high water concentration plays a key role in transferring heat away from the tool-workpiece interface, thus preventing temperature elevation (as can be seen in Figures 5 and 6) and the consequent reduction in the shear strength of the work material. When minimal quantity lubrication is applied, however, the intermediate specific cutting energy value suggests that the access of oil droplets in the tool-workpiece interface is improve and less energy is spent in sliding due to the reduction in the friction coefficient. Finally, lowest specific cutting energy is obtained when performing the pendulum scratch test without cutting fluid application, probably owing to the fact that the temperature increase promotes the softening of the work material (reduction in the specific cutting energy associated with chip formation).

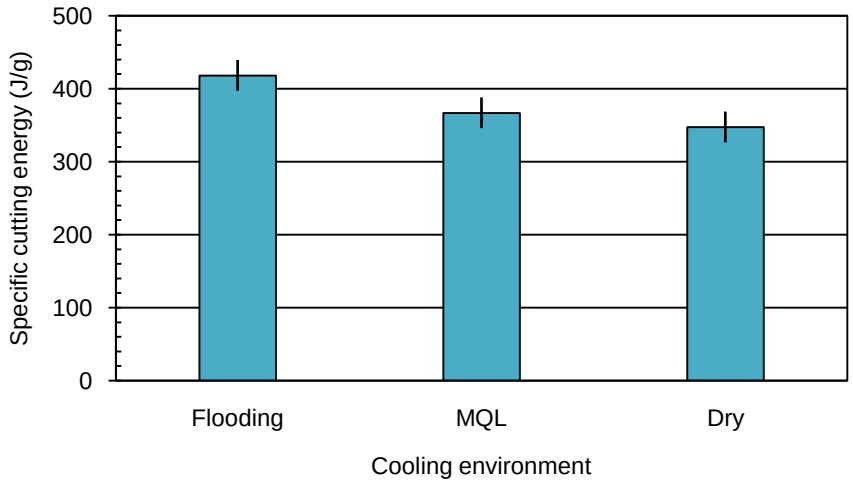

FIGURE 7: EFFECT OF COOLING ENVIRONMENT ON THE SPECIFIC CUTTING ENERGY

Considering that the specific cutting energy is equivalent to the specific heat capacity ($m \cdot c \cdot \Delta T$), the temperature change associated with chip formation can be estimated. In the case of the scratch tests performed without cutting fluid, the average specific cutting energy is u=347.4 J/g. Estimating the specific heat capacity of steel as c=0.466 J/gK results in a temperature change of 745 K (or 745° C) when removing a cross section of 1 mm^2 at a speed of 276 m/min, while the temperature recorded by the thermocouple embedded 1.01 mm beneath the rake face of the cutting tool recorded 330.5° C when turning at a cutting speed of v_c=200 m/min and removing chips with a cross section of 0.45 mm^2 (f =0.3 mm/rev and a_p=1.5 mm).

Considering the difference in the shear areas for both cases and distance between the tool-chip interface and thermocouple position, the difference between the calculated temperature change and value measured by the thermocouple is quite plausible.

IV. CONCLUSION

After conducting continuous turning tests on AISI 4340 steel using coated tungsten carbide tools under flooding, minimal quantity lubrication (MQL) and dry cutting in order to measure the cutting tool temperature (using the implanted thermocouple method) and performing pendulum scratch tests on a modified impact testing machine in order to assess the specific cutting energy associated with each cooling environment, the following conclusions can be drawn:

- As far as the influence of the cutting parameters is concerned, temperature in the cutting tool increased with the elevation of cutting speed, feed rate and depth of cut, however, the effect of cutting speed was considered not statistically significant with a confidence level of 95%. This behaviour can be explained by the fact that the tool-chip contact area is reduced as cutting speed is elevated, therefore the heat source is moved farther from the thermocouple location.
- Cooling environment statistically affected cutting tool temperature and lowest tool temperatures were recorded when flood turning, followed by minimal quantity lubrication and dry turning.
- Inversely, lowest specific cutting energy was obtained during the dry pendulum tests, thus suggesting that the higher temperature achieved under this condition aid the softening of the work material and the reduction of its shear strength. Highest specific cutting energy was recorded for the tests under flooding and intermediate results were achieve using minimal quantity lubrication, which indicates that the oil droplets produced by MQL are capable of reducing the friction coefficient and, consequently, the fraction of the specific energy associated with sliding.
- The modified pendulum scratch test allowed the calculation of the temperature associated with the chip formation mechanism.

ACKNOWLEDGEMENTS

The authors would like to thank the following research agencies in Brazil for supporting this research project: CNPq, CAPES and FAPEMIG.

REFERENCES

[1] F.W. Taylor,On the art of cutting metals, New York: The American Society of Mechanical Engineers, 1906. Available at: <http://ir.library.oregonstate.edu/xmlui/handle/1957/21006>. Access on the 7 October 2014.

[2] M. Hadad, and B.Sadeghi, "Minimum quantity lubrication-MQL turning of AISI 4140 steel alloy",J. Cleaner Prod., vol. 54, pp 332-343, 2013.

[3] V.S. Sharma, M. Dogra, and N.M.Suri,"Cooling techniques for improved productivity in turning",Int. J. Machine Tools Manuf., vol. 49(6), pp. 435 – 453, 2009.

[4] S. Kalpakjian, and S.R.Schmid, Manufacturing Engineering and Technology. New Jersey: Prentice Hall, 2010.

[5] S.A. Lawal, I.A. Choudhury, and Y.Nukman, "Developments in the formulation and application of vegetable oil-based metalworking fluids in turning process", Int. J. Adv. Manuf. Technol., vol. 67(5–8),pp. 1765–1776, 2013.

[6] I.B. Abhang, and M. Hameedullah, "Experimental investigation of minimum quantity lubricants in alloy steel turning", Int.J. Eng. Sci. Technol., vol. 2(7), pp. 3045–3053, 2010.

[7] N.R. Dhar, M.W. Islam, S. Islam, and M.H.A. Mithu, "The influence of minimum quantity of lubrication (MQL) on cutting temperature, chip and dimensional accuracy in turning AISI-1040 steel", J. Mater. Process. Technol., vol.171(1), pp 93–99, 2006.

[8] N. Boubekri, V. Shaikh, and P.R. Foster. "A technology enabler for green machining: minimum quantity lubrication (MQL)". Journal of Manufacturing Technology Management. 2010; 21(5): 556–566.

[9] G.D. Revankar, R. Shetty, S.S. Rao, and V.N.Gaitonde, "Analysis of surface roughness and hardness in titanium alloy machining with polycrystalline diamond tool under different lubricating modes", Mater. Res., vol. 17(4), pp. 1010-1022, 2014.

[10] A.S. Varadarajan, P.K. Philip, and B. Ramamoorthy, "Investigations on hard turning with minimal cutting fluid application (HTMF) and its comparison with dry and wet turning",Int. J. Machine Tools Manuf., vol. 42(2), pp. 193–200, 2002.

[11] K-M. Li, and S.Y. Liang,"Performance profiling of minimum quantity lubrication in machining", Int. J. Adv. Manuf. Technol., vol.35(3–4), pp. 226–233, 2007.

[12] C.R.V. Kumar, and B. Ramamoorthy, "Performance of coated tools during hard turning under minimum fluid application", Journal of Materials Processing Technology. 2007; 185(1–3): 210–216.

[13] S. Malkin. Grinding technology: Theory and applications of machining with abrasives, Nova York: John Wiley & Son Limited, 1989.

A Study into the Development of More Energy Efficient and Less Polluted Fishing Vessel

Pramudya Imawan Santosa[1], I.K.A.P Utama[2], Wasis D.A[3]

[1]Institut Teknologi Adhi Tama (ITATS) Surabaya, Indonesia
[2,3]Institut Teknologi Sepuluh Nopember (ITS) Surabaya, Indonesia

Abstract— *The successful application of catamaran hull form as passenger carriers has been well-known since the last 30 years. It is later extended to the development of fishing vessels and the reason behind this is attributed to safety criteria and wider deck-space which can be offered by the catamaran. It is also in connection with the handicaps of monohull fishing vessels, in terms of stability and seakeeping performance which can be improved by the introduction of catamaran forms. Recent situation on the rare and expensive fossil fuels have caused the fishermen into deep trouble hence most of them tend to be deprived if there is no anticipation taken to help them. The current paper describes a systematic investigation into the way to reduce (if not possible to replace completely) the use of fossil fuels on a catamaran fishing vessel. The study is focused on the use of diesel engine, sail and solar power on individual application as well as the combination of them. The implication to the final cost of the vessel, however, is negligible. It is discovered that the use of diesel engine could be replaced by the use of sail and solar power for individual basis. A combination of those power sources is found to be more appropriate in terms of stability and capacity of fishing holds. The investigation is extended to the evaluation of energy efficiency design index (EEDI), a compulsory criterion for measuring marine pollution made by the international maritime organization (IMO) and applied for ocean-going vessels. It is considered for fishing vessels because this type of vessel is thousands in number and most of them use engine together with fossil fuels hence there is strong potency to pollute air and the environment.*

Keywords— Catamaran, fishing vessel, stability and seakeeping, power estimation, energy efficiency.

I. INTRODUCTION

In the last thirty years, there has been a great increase on the use of catamaran for various applications such as ferries, fishing vessels, sporting craft, and oceanographic research vessel [1]. The main advantages of catamaran compared to single hull are a wider deck space area, better transverse stability, and in certain case lower total resistance [2, 3]. Considering the resistance performance and wider deck space area for catamaran hull, it is a potentially good to apply for fishing vessel. Wider space area provides freedom of ship crews for fishing activities and to install fishing equipments on deck [4].

Factors driving fishing vessel operational, in general, are economic and environmental issues. The main economic concern, in particular, is fuel costs and the main environmental issue amounts to emissions and pollution [5]. Conventional Fishing vessel uses diesel engine and is found to be not economical in term of fuel spending and environmental issues. Recent situation on the rare and expensive fossil fuels have caused the fishermen into deep trouble hence most of them tend to be depressed if there is no anticipation taken to help them [6].

Development of environmental friendly vessels has become a major issue since the last twenty years. This occurs due to the scarcity and high cost of fossil fuels especially for ocean-going vessels in the world. Other reason relates to efforts to reduce the spread of toxic gases to the atmosphere such as CO, CO_2, SO_2 and NO_2 which is mainly caused by the use of fossil fuels [5, 6].

The powering of vessel without using engine and fuel oil has later become more popular considering environmental issues. There are several choices of power systems such as the use of sail, solar powered, diesel engine or the combination of those two and three power systems [6]. A combination of those power sources is found to be more appropriate in terms of stability and capacity of fishing holds. Overall, ship stability and seakeeping evaluation are considered for fishing vessels because of the placement of sail and (later) solar panel can affect ship stability and seakeeping qualities [7].

II. LITERATURE REVIEWS

2.1 Catamaran resistance

The most widely used estimation of catamaran resistance is the method proposed by Insel and Molland [2]. Catamaran hull consists of 2 isolated demihulls and creates wave and viscous resistance interference and formulated as follows:

$$C_T = (1+\phi k)\sigma C_F + \tau C_W \quad (1)$$

Where:

C_T is total resistance coefficient, C_F is frictional resistance coefficient and obtained from ITTC-1957 correlation line, C_W is wave resistance coefficient of isolated demihull, (1+k) is form factor value of isolated demihull, ϕ is used to estimate the change of pressure around demihull, σ represents additional velocity between demihulls and calculated from the summation of local frictional resistance around wetted surface area. In fact, the factors of ϕ and σ are difficult to measure hence for the practical purposes, the two factors can be combined to form viscous resistance interference factor β where $(1+\phi k)\sigma = (1+\beta k)$ hence:

$$C_T = (1+\beta k)C_F + \tau C_W \quad (2)$$

Where for monohull or demihull at isolation the value of β=1 and τ =1.

2.2 Powering

2.2.1 Conventional Engine

The overall concept of the powering system may be seen as converting the energy of the fuel into seful thrust (*T*) to match the ship resistance (*R*) at the required speed (*V*) [8], (see figure 1).

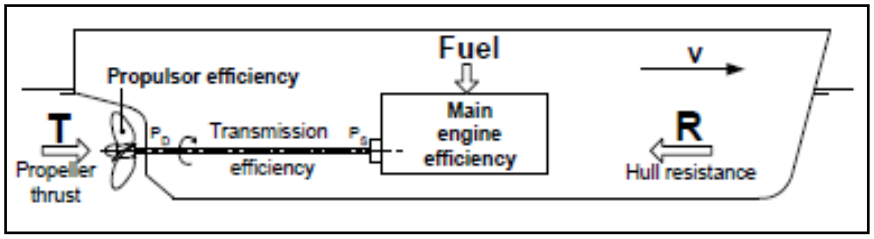

FIGURE 1: OVERALL CONCEPT OF ENERGY CONVERSION [8]

It is seen that the overall efficiency of the propulsion system depends on: fuel type, properties and quality; the efficiency of the engine in converting the fuel energy into useful transmittable power; and the efficiency of the propulsor in converting the power (usually rotational) into useful thrust (*T*). The present study concentrates on the performance of the hull and propulsor, primarily considering, for a given set of constraints, how resistance (*R*) may be reduced and thrust (*T*) may be increased.

2.2.2 The Use of Sail

A sail is defined as a surface, typically made of fabric and supported by a mast with purpose to propel a sailing vessel [9,10]. Recently, as fuel costs increase, particularly when fast journey time is not critical, there is a renewed interest in the commercial use of sail propulsion either as a primary source of propulsion with usually a back-up diesel-propeller for safety or as a means of providing additional power when wind is available [9]. The choice of sail arrangement and underwater hull and appendage design can make a large difference in available speed for given wind directions and magnitudes.

2.2.3 Solar panels

Solar panel as a powered boats get their energy from the sun. By using electric motors and storage batteries charged by solar panels and photovoltaic cells, solar powered boats can significantly reduce or eliminate their use of fossil fuels. Solar boats are uniquely suited to transform light energy into movement. Environmental friendly solar energy is an energy efficient way to power commercial oceangoing vessels as well as leisure boats [5].

2.2.4 Development Hybrid Vessel in the World

Several power systems have been developed such as combination of engine and sail which is later known as sail assisted engine. The powering vessel without using engine and fuel oil has later become more popular considering environmental issues. Successful application of catamaran type of vessel as passenger carrier with hybrid power has been well-known such as Foscat32, Greenpeace Rainbow Warriors and New York Hornblower [5].

2.3 Stability and Seakeeping Evaluation

Catamaran vessel has better transverse stability compared to monohull. Catamaran has been applied successfullly as passenger carriers, oceanographic research vessels, and leisure boats [1, 2]. Recent work shows that catamaran is feasible as fishing vessel, particularly for coastal waters operation [5]. Seakeeping ability is a measure of how well-suited a watercraft is to conditions when underway [7]. A ship or boat has good seakeeping ability is said to be very seaworthy and is able to operate effectively even in high sea states. Ship stability and seakeeping evaluation are considered for fishing vessels because of the placement of sail and solar panel can reduce the ship stability and seakeeping qualities. Also, fishing vessels are usually operated in more open sea hence this vessels are prone to capsize. Several surveys indicated that fishing vessel has reached the highest accident rates among othe types of vessel. Under United Kingdom Regulation every fishing vessel of 12 m registered length and over is required to satisfy as fairly specific minimum stability aggregate [12]. The specific requirement in relation to the static stability curve is given below (see figure 2):

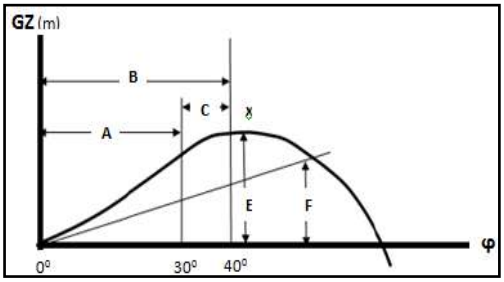

FIG.2 STATIC STABILITY CURVE [12]

A - area under curve up to 30 degrees to be not less than 0,055 meter-radians
B - area under curve up to x degrees to be not less than 0,09 meter- radians
C - area between 30 degrees and x degrees to be not less than 0,03 meter-radians
x - 40 degrees or any lesser angle at which the lower edges of any openings in the hull, superstructure or deckhouses which lead below deck and cannot be closed, will be immersed.
E - maximum GZ to occur at angle not less than 25 degrees and to be at least 0,20 meter at an angle equal to or greater than 30 degrees
F - Initial GM to be not less than 0,35 meter.

2.4 Criterion for measuring CO_2 environmental impact

The emissions from ships include NOx, SOx and CO_2. CO_2 emissions have a global climate impact and a concentrated effort is being made worldwide towards their reduction. In order to monitor and quantify CO_2 emissions, the International Maritime Organization (IMO) has developed an Energy Efficiency Design Index [13, 14].

The general form of the Energy Efficiency Design Index, as proposed by IMO, is as follows:

$$\text{EEDI} = \frac{P \times sfc \times C_F}{C \times V} \text{gm CO}_2\text{/tonne mile}$$

Where *P* is power (kW), *sfc* is specific fuel consumption (gm/kW.hr), C_F is a CO_2 conversion (tonne CO_2/tonne fuel), C is the capacity of the ship (DWT or GT) and *V* the speed (knots). As such, EEDI can be seen as a measure of a ship's CO_2 efficiency.

III. RESULT AND DISCUSSION

When considering the overall form of the Energy Efficiency Design Index it is clear that in order to reduce the index for a given ship at a given speed, a decrease in propulsive power must be achieved and/or improvements made in engine efficiency with a reduction in *sfc*. Improvements in efficiency of propulsion will lead directly to improvements in the economic return and a decrease in GHG emissions. This means that there is now a double incentive to pursue such efficiency improvements. There are, however, some possible technical changes that will decrease emissions, but which may not be economically viable [8]. Potential savings in resistance can be achieved throughout hull form selection and enhanced hull coatings, are likely to come into this category.

3.1 Improvement in Resistance

The experimental work was conducted using towing tank and a symmetrical catamaran model (S/L=0.4) were tested and the results are given in Table 1. The particular of vessel is 14.5 m LWL, 7.118 m B, 1.44 m H, 0.694 m d and 11.8 t Displacement. The models were tested at speed equal to speed of real vessel at open sea from about 5 to 10 knots and the Froude numbers were about 0.24 to 0.48 or from low speed to medium speed condition and the details can be found in [4].

TABLE 1
RESISTANCE RESULT OF TOWING TEST

Run Number	V (knots)	R_T (kN)	EHP	C_F	C_T
1	5.7	1.66	6.596	0.0023	0.0077
2	6.2	2.06	8.930	0.0023	0.0081
3	6.6	2.35	10.896	0.0023	0.0080
4	7.1	2.95	14.562	0.0022	0.0089
5	7.5	3.55	18.513	0.0022	0.0096
6	7.9	3.77	20.767	0.0022	0.0091
7	8.5	4.34	25.768	0.0022	0.0091
8	9.0	4.66	29.322	0.0022	0.0087
9	9.4	5.51	36.210	0.0022	0.0094
10	9.8	6.14	42.172	0.0021	0.0096

3.2 The use of Conventional Engine

If the catamaran is powered by engine at the speed of 9.8 knots, it requires effective power (PE) about 42 HP and breaking power (P_B) about 70 HP presumably the total eff. is 60%. The conventional engine thus contributes 0.2218 g CO_2 /ton mile of CO_2 index. Thrust (T) = $R_T/(1-t)$ [11], (given T: 4.12 kN). *Thrust deduction fraction* (t) = k_R . *wt*, for twin screw [11], where:

k_R is 0.5 for thin rudder, *wt* = -0.0458 +0.3745C_B^2+0.1590D_w-0.8635Fr+1.4773Fr^2, $D_w = \frac{B}{\nabla^{1/3}}\sqrt{\frac{\nabla^{1/3}}{D}}$, (given t : -0.49).

3.3 Improvement in Powering

To identify key areas where changes and improvements in powering might be made and decreases in power and hence CO_2 index, suggestions that emissions trading for ships may be introduced in the future are given below:

3.3.1 The use of Solar Panels and Sail (Solar Sail)

To achieved thrust power (T) of about 4,12 kN and speed (Vs) = 9,8 knots, the boat required 52 kW to move produce by 289 solar panels (180 WP) with 298 m^2 areas and 0.825 ton weight devices and Sail areas = 140 m^2 with 0.378 ton weight devices [9, 10].

3.3.2 The use of combination powering

All means of improvement in powering and reduction in greenhouse gas emissions should be explored and assessed, even if such improvements may not be directly economically viable. The following combinations are possible: (i) engine – solar panels, (ii) engine – sail, (iii) solar panels – sail, and (iv) engine – solar panels – sail (See figure 3 and 4).

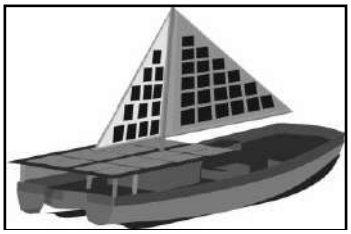

FIG.3 HYBRID CATAMARAN FISHING VESSEL [7]

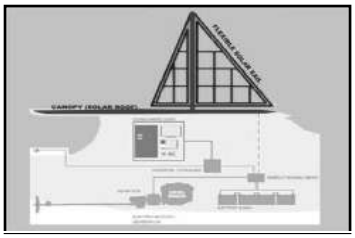

FIG.4 HYBRID POWER SYSTEM CONFIGURATION [7]

Many efforts to reduce the use of fuel and GHG effect have been made worldwide. The use of alternative energy to complement or replace the use of fuel is actively conducted around the world. The combination or hybrid of engine and sail has been done in many places in Indonesia especially by fishermen. The combination use of engine, solar powered and sail has become other promising answer.

IV. CONCLUSION

The present work apparently portraits a study into the development of more energy efficient and less polluted fishing vessel. Application of hybrid technology is very useful when applied to catamaran fishing vessels. The development of hybrid vessel gives a promising expectation in order to reduce the use of fossil fuels. It has been found that the use of sail or solar sail and solar panel in combination with the operation of electric engine is to be very useful.

REFERENCES

[1] Utama, IKAP., 2009, Development of Efficient and Environmentally Friendly Vessel Using Multihull Configuration, World Ocean Conference (WOC), Manado, Indonesia.

[2] Insel, M and Molland, A F, 1992, "An investigation into the resistance components of high speed displacement catamarans", Transactions of the Royal Institution of Naval Architects, RINA,Vol. 134.

[3] Turner, H and Taplin, A, 1968, "The resistance of large powered catamaran", Transactions of the Society of Naval Architects and Marine Engineers, SNAME, Vol. 76.

[4] Setyawan, D, Utama I K A P, Jamaluddin, A, Sugiarso, A., 2010, Development of Catamaran Fishing Vessel, IPTEK, The Journal for Technology and Science, Vol. 21, No. 4.

[5] Utama, IKAP and Santosa, PI., Nasirudin A., Chao RM., 2013, Study of Solar Catamaran Fishing Vessel, APAC, Unhas, Denpasar, Indonesia.

[6] Santosa, P.I. and Utama, I.K.A.P, 2012, Techno-Economic Review of Hybrid/Electric Catamaran Fishing Vessel, Procs. 13th QiR, Yogyakarta.

[7] Santosa, P.I. and Utama, I.K.A.P, 2014, Stability of Hybrid Catamaran Fishing Vessel, International Seminar Stability Workshop (ISSW), Kuala Lumpur, Malaysia.

[8] Utama, I K A P and Molland, A F, 2012, The powering of future ships taking into consideration economic viability and environmental issues, International Conference on Ship and Offshore Technology (ICSOT), Ambon, Indonesia.

[9] Kinney, F.S., 1977, Skene's Element of Yacth Design, ISBN: 071361823x, ACB Ltd, London.

[10] Larson L., 2007, Principles of Yacht design, 3rd editions., ISBN-13: 9780071487696, Mc Graw Hill.

[11] Molland AF, Turnock SR, Hudson DA, 2011, Ship Resistance and Propulsion – Practical Estimation of Ship Propulsive Power, ISBN:978-0-521-76052-2 Hardback, CUP, USA.

[12] Hind, J.A., 1982, Stability and Trim of Fishing vessel, ISBN: 0852381212, FNB Ltd, England

[13] IMO, 2012a, Guidelines on the Method of Calculation of the Attained Energy Efficiency Design Index (EEDI) for new ships, Resolution of the Marine Protection Environment Committee, MEPC.212(63).

[14] IMO, 2012b, Guidelines on Survey and Certification of the Energy Efficiency Design Index (EEDI), Resolution of the Marine Protection Environment Committee, MEPC.214(63).

AD Publications
Sector-3, MP Nagar, Bikaner,
Rajasthan, India
www.adpublications.org, info@adpublications.org